# IN SITU TEM AND CONTINUUM MODELING OF LASER-INDUCED RAPID SOLIDIFICATION OF ALUMINUM AND ALUMINUM COPPER ALLOYS

by

Can Liu

B.Eng., First Class Honors, University of Birmingham, 2010

Submitted to the Graduate Faculty of

Swanson School of Engineering in partial fulfillment

of the requirements for the degree of

**Doctor of Philosophy**

University of Pittsburgh

2017

UNIVERSITY OF PITTSBURGH

SWANSON SCHOOL OF ENGINEERING

This dissertation was presented

by

Can Liu

It was defended on

January 23, 2017

and approved by

Ian Nettleship, Ph.D., Associate Professor

Departmental of Mechanical Engineering and Materials Science

Markus Chmielus, Ph.D., Assistant Professor,

Departmental of Mechanical Engineering and Materials Science

Guangyong Li, Ph.D., Associate Professor

Departmental of Electrical and Computer Engineering

Dissertation Director: Jörg Wiezorek, Ph.D., Professor

Departmental of Mechanical Engineering and Materials Science

Copyright © by Can Liu

2017

# IN SITU TEM AND CONTINUUM MODELING OF LASER-INDUCED RAPID SOLIDIFICATION OF ALUMINUM AND ALUMINUM COPPER ALLOYS

Can Liu, PhD

University of Pittsburgh, 2017

In situ characterization of rapid solidification processes has proven too challenging for conventional characterization techniques as they fail to meet the spatio-temporal resolution requirements for observing the rapid transient processes. Recent advances in ultra-fast time-resolved in situ transmission electron microscopy enabled characterization of pulsed laser induced melting and rapid solidification processes in Al and Al – Cu alloys with unprecedented spatio-temporal resolution using the unique Dynamic Transmission Electron Microscope (DTEM). The DTEM achieves nano-scale spatio-temporal resolution by modifying a conventional TEM with two laser systems – the image formation laser system and process initiation laser system, for observing rapid solidification process in a thin film geometry.

In this study, in-situ DTEM experimentation has been utilized to document rapid solidification processes in Al and Al – Cu alloy thin films, enabling accurate determination of average solidification velocity evolution and associated crystal growth mode changes during rapid solidification process in pure aluminum and hypo-eutectic and hyper-eutectic Al – Cu alloys. Enthalpy transport based computer modeling has been performed and benchmarked by experimental metrics obtained from in situ DTEM experimentation to calculate the spatio-temporal thermal field evolution during the rapid solidification process in Al. This demonstrated the unique capability of in situ DTEM experimentation to deliver quantitative metrics from direct observation with nano-scale spatio-temporal resolution for the validation of computer modeling.

Post-mortem characterization provided detailed insights on microstructural evolution during rapid solidification process by establishing the correlation between solidification conditions and resultant microstructural constitution. The respective influence of heat transfer, crystallography and Cu concentration on the details of the dynamics of the rapid solidification process in hypo-eutectic and hyper-eutectic Al – Cu alloys were examined and quantified. The investigation showed that rapidly solidified microstructures in pulsed laser irradiated TEM transparent Al – Cu thin films exhibit equivalent microstructural features developed in bulk alloy samples after laser surface melting. DTEM experimentation uniquely allowed direct observation of rapid solidification processes in Al and Al-Cu alloys, and facilitated high precision determination of process metrics such as critical velocities for crystal growth mode changes, which are important to improved understanding of alloy microstructure evolution under the driven, far-from-equilibrium conditions pertaining to rapid solidification.

**Key words:** Transmission Electron Microscopy, In Situ TEM, Dynamic TEM, Rapid Solidification, Aluminum, Aluminum Copper Alloy, Laser, Continuum Modeling, Precession Electron Diffraction, OIM

## TABLE OF CONTENTS

# LIST OF TABLES

# LIST OF FIGURES

# PREFACE

First and foremost, I would like to express my deep gratitude to my Ph.D. adviser, Prof. Jörg Wiezorek. The PhD study has been a memorable but also challenging journey for me, especially due to a physical injury that had to be treated with two surgeries and prolonged physical therapy afterwards. I would not have been able to successfully complete my PhD study without Prof. Jörg Wiezorek's kindness, patience, encouragement, inspiration and knowledge. It is fortunate for me to have Prof. Jörg Wiezorek as my mentor, not only in terms of academic, but also in terms of life.

To the LLNL and IDES team, particularly Dr. Joseph McKeown, Dr. Thomas LaGrange and Dr. Bryan Reed, thank you for making the DTEM possible and the opportunity to utilize this state-of-the-art instrument for this research.

To Dr. Kai Zweiacker, who has laid the foundation of this research and has been my closest collaborator on this research, I enjoyed working together with you on this project and this dissertation would not have been possible without all your effort and help.

To my lab mates and student colleagues, Dr. Xiahan Sang, Dr. Yaakov Idell, Dr. Andreas Kulovits, Dr. Mauricio Gordillo, Dr. Giovanni Facco, Jaehyuk Jo, Shan Gong and all the friends I met and people who helped me during my study at Pitt. You all made the lab, the university and the city of Pittsburgh a special memory to me. I also want to thank Dr. Yinkai Lei and his wife, Dr. Rongjuan Wang, I am indebted to you for taking good care of me and helping me with many aspects of daily life while I was severely immobilized after the accident and two surgeries during the entire year of 2013.

To Wenqing Yang, my beloved fiancée, being together with you is one of the happiest things in my life and I truly hope that we will be happily together, just like myself and the Ph.D. degree. Thank you for all your support during this demanding endeavor.

Finally, I want to thank my parents, Guogen Liu and Hong Fu, for bringing me to this world, allowing me to adventure and supporting me with their endless love throughout my study and my life.

# 1.0 INTRODUCTION

Solidification is the phase transformation from liquid to solid as the temperature of the system decreases below its freezing point. Solidification processing has been one of the fundamental steps in the manufacturing of metallic materials and components, which are used in engineering systems for applications in the field of structure, transportation and energy, as well as electronic, electro-magnetic and biomedical technologies [1]. The conditions under which solidification takes place, namely the thermal gradients and resulting rates of the crystal growth, largely determine the microstructures and properties of the solidified materials. These solidification microstructures represent the initial state of the engineering material obtained from the solidification processing. Subsequent thermo-mechanical processing is typically required to modify the microstructures further and thereby render the materials fit for a given set of applications.

Among the many governing factors of solidification, solidification velocity is of particular interest because it can be controlled relatively easily by changing the thermal transport behavior during solidification process. The solidification velocity - the crystal growth rate during the liquid-to-solid transformation, affects the microstructure of the resulting solid in multiple ways. Unique microstructures in metals and alloys can be attained by solidification under conditions that facilitate very fast crystal growth from the liquid, associated with unusual properties. Under such conditions of the rapid solidification crystal growth rates in metals and alloys are typically in excess of 0.01 m/s and often involve rapid extraction of thermal energy to include both superheat and heat of crystallization during the solidification processes, which permits large deviations from equilibrium conditions during the transformation. For example, compared to conventional casting, where normally a few Kelvin of undercooling is achieved at the liquid-solid transformation interface, the undercooling achieved during rapid solidification processes can be as high as tens or even hundreds of Kelvin prior to the initiation of solidification. As a result, rapid solidification produces unique solidification microstructures in metals and alloys [2]. Depending on the solidification conditions and constitutional effects at the solidification interface, refinement of microstructure at various length scales, changes in the primary solid product phase and the formation of metastable phases or even non-crystalline phases can be introduced. These microstructural changes offer potentially advantageous mechanical, electronic, electromagnetic properties and usually are not attainable through conventional solidification and processing routes [3,4]. Therefore, rapid solidification of metals and alloys has been widely studied and has been attracting tremendous amount research interest as a viable method to modify microstructures of materials for improved properties [5–7].

Numerous models concerning rapid solidification processes have been proposed and significant amount of both theoretical and experimental research has been performed to examine these models [3,4,6]. However, many mechanistic details associated with the rapidly moving liquid-to-solid transformation interface, which are considered to dominate microstructure evolution occurring during rapid solidification transitions have not been fully elucidated yet [8–24]. One of the major challenges is the development of links of experimental observations of rapid solidification microstructures and their evolution with existing theories that predict or explain physical, chemical and thermal phenomena occurring during rapid solidification processes. For post-mortem characterization based analyses of rapid solidification microstructure evolution, any phenomena occurring during the phase transformation, such as the interface morphology and interface velocities, are not directly observed and the effort to correlate post-mortem characterization with theoretical predictions is inherently based on numerous assumptions and even requires speculations. This introduces considerable amount of uncertainty to the attempted linking of the microstructure resulting from rapid solidification and the theoretically predicted conditions prevalent at during its formation. Thus, it would be desirable to complement the post-mortem studies of rapid solidification microstructures with in situ experiments. The latter could deliver direct observations of the transformation interface and other features of the evolution of rapid solidification microstructures in metals and alloys. The rapid solidification processes in metals and alloys typically establish significantly scale refined polycrystalline microstructures, often with sub-micron or even nano-meter dimension grains. Thus, in situ observation of rapid solidification requires high spatial resolution as well as high temporal resolution to acquire accurate data by in-situ experimentation that can be used to reveal the dynamics of rapid solidification processes. This proves to be challenging for conventional characterization techniques such as optical sensing based high speed imaging, X-Ray diffraction, measurements based on optical and/or electrical property change of materials during solidification and conventional electron microscopy. Conventional experiments utilized in most prior studies on rapid solidification either provided adequate spatial resolution, while sacrificing the temporal resolution or offered sufficient temporal resolution but had limited spatial resolution [25–27]. Moreover, due to the limitation of computation resources, models for simulating rapid solidification processes, especially details at interfaces, are usually constructed to consider relatively small dimensions, which renders experimental data of limited resolution from larger scale might not be suitable for modeling input or verification. As a result, there is a gap between the capability of conventional post-mortem and in situ characterization techniques and experimental data needed for validating available models toward further understanding of rapid solidification processes. Without appropriate experimental data, it is very difficult to evaluate the validity of current models and theories, hindering development and improvement of theories relevant to rapid solidification processes.

To address this apparent problem, built upon recent prior work that established reliable methodology for in situ study of rapid solidification process in metallic thin films and usage of such on observing the rapid solidification process in pure Al and hypo-eutectic Al – 4 at.% Cu alloy thin films [28], this current study investigated pulsed laser induced rapid solidification of Al and Al-Cu alloys using the state – of – the – art dynamic transmission electron microscope (DTEM) located at Lawrence Livermore National Laboratory (LLNL) in combination with ex-situ pulsed laser processing and multiphysics based numerical modeling. The DTEM instrumentation enables imaging and diffraction using 200kV electrons with nanometer spatial resolution (< 10 nm) and nanosecond temporal resolution (< 15 ns), which perfectly satisfies the requirements for tracking dynamics of the rapid solidification process and offers opportunity to provide experimental data that cannot be obtained from more conventional techniques [29–33]. By conducting in – situ experiments in the DTEM, dynamics and physical parameters during rapid solidification of Al and Al-Cu alloys, such as evolution of solidification front morphology, average crystal growth rates from local and global measurements of the velocities of advancing solidification interfaces have been recorded. Linking these data sets with information provided by conventional transmission electron microscope (TEM), scanning electron microscope (SEM) before and after the in – situ experiments, e.g. regarding alloy composition, grain size and grain orientation, allows us to develop improved understanding of the rapid solidification processes that is uniquely based on direct observations of the transition events. Therefore, we are able to provide experimental observations and measurements that can lead to qualitative and quantitative improvements in understanding of rapid solidification process that is experimentally fully validated. Furthermore, the experimental methodologies established during this research can be adapted to investigate other alloy systems. The microscopic specimens and experimentation has potential to become a versatile platform for the facile and effective experimental evaluation and study of solidification microstructure evolution with respect to crystallization rates and local (spatially and temporally) events, i.e., inclusive of non-averaged behaviors, enabling the determination of solidification microstructure selection maps (SMSM).

Numerical modeling using COMSOL®, a continuum multiphysics based software environment, will complement the experimentation. Thus, based on calculations of heat conduction, the simulation of temperature evolution during the pulsed laser induced rapid solidification will be accomplished. Comparing the modeling results with experimentally measured parameters allows us to validate the computational model(s). For instance, the unique capability of DTEM to track the velocity of the migrating front with spatio – temporal resolution at the nano-scale (e.g. the interface migrates 10nm during 10ns means a migrating velocity of 1m/s) enables us to compare the measured velocity and velocity predicted by existing solidification models and simulations. Therefore, it will become possible to establish a robust theoretical model that can elucidate the liquid – solid transformation and associated physical effects during rapid solidification.

# 2.0 RESEARCH OBJECTIVES

Post-mortem characterization and conventional in situ characterization techniques fail or are incapable to provide experimental data with the appropriate spatio-temporal resolution for direct observation based validation of theoretical model predictions relevant to rapid solidification based microstructure evolution in metallic materials. The absence of in situ observation based data of the dynamic processes associated with the migrating liquid-solid interface during the transformation hinders further development of predictive theories that are capable of correlating solidification conditions and resultant microstructure evolution in multi-component metallic alloys.

In order to facilitate development of improved quantitative understanding of the rapid solidification associated microstructure evolution in metals and alloys, the *major aims of the research conducted here include the elucidation and quantification of details of the transient liquid – solid transformation in metals and alloys through in situ observation of pulsed laser induced melting and subsequent rapid solidification processes in metallic thin film geometry.* Specific goals include the direct observation of the transformation interface morphology, e.g. planar, smooth and stable versus non-planar, rough and unstable, as a function of a) interface velocity and b) for different composition in concentrated binary alloys. By utilizing the DTEM at LLNL, combined with complementary post-mortem characterization methods, this research will deliver novel experimental data based on direct observations with nano-scale spatio-temporal resolution that cannot be obtained in other more conventional in situ microstructure analysis techniques.

The materials chosen for this research are from the Al-rich side of the binary Al – Cu alloy system, with compositions ranging from pure Al with 0 atomic % (at.%) Cu to hyper-eutectic alloy with up to 22 at.% Cu. Investigating the Al rich Al – Cu system, which is a classic eutectic system with terminal phases of α-Al and θ-$Al_2Cu$ (see Figure 1), allows us to clarify the influence of constitutional effects on rapid solidification microstructure evolution.

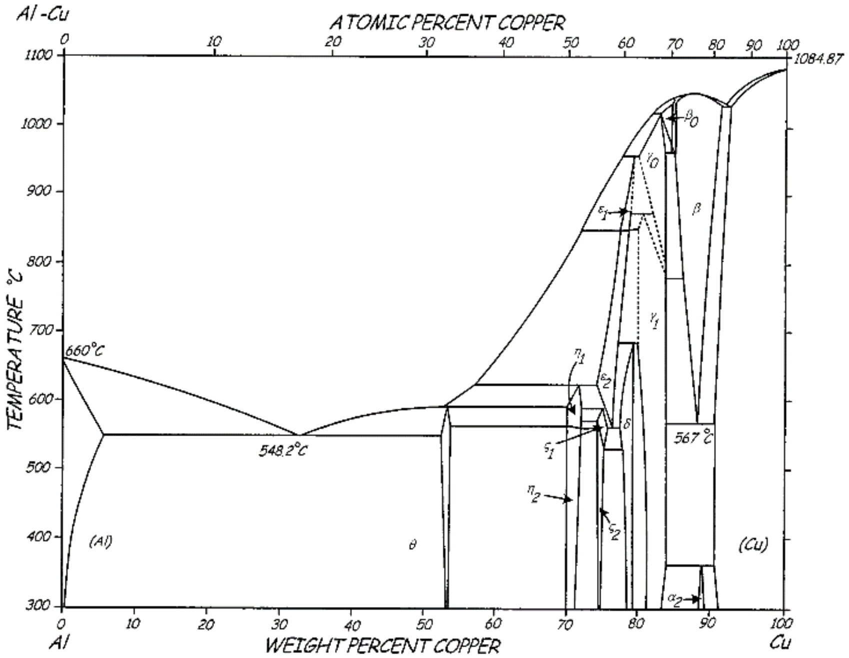

**Figure 1. Al-Cu Phase Diagram**

Also, rapid solidification behavior of bulk Al – Cu alloys was comprehensively studied previously, using it as a model system for which reliable sets of thermo-physical data are available [34–36]. Therefore, benchmarking data from prior studies exists. Furthermore, the constituents of the binary eutectic exhibit different types of growth interfaces from the liquid phase. The face centered cubic solid solution phase α-Al exhibits atomically rough interfaces typical of non-facetted growth of metals, while the chemically ordered tetragonal θ-$Al_2Cu$ phase, an intermetallic compound with a narrow composition range, has a compositionally layered structure and has been associated with a facetted growth morphology [34,37].

Previously, K. Zweiacker and co-workers have established methodology for MM-DTEM experimentation that would yield reproducible results using pure Al as the model system [28]. Study on rapid solidification process in Al – 4 at.% Cu has also been performed to evaluate the rapid solidification behavior of hypo-eutectic Al – Cu alloys for comparison purpose and effect of Cu on the rapid solidification process. However, the temperature evolution and associated heat transfer during rapid solidification of pure Al thin films remains insufficiently well known. Complementing multi-physics based numerical modeling based computer calculation, which can be verified by experimental results, of the transient processes will be conducted in this study to facilitate basic understanding the heat transfer and spatio-temporal temperature evolution during the processes subsequent to the laser pulse related melting in Al thin films. The pure element (single component) Al is used for this purpose in order to avoid constitutional effects and phenomena, which could potentially affect and render more complex modeling effort.

Combining the results from the multi-physics based computer model calculations of the dynamics of post-laser pulse delivery melting and subsequent solidification for the Al system with data sets acquired from ex – situ studies before and after the in – situ studies will enable us to discover possible mechanisms regarding responses of Al and Al-Cu alloy thin films to pulsed laser melting and accompanying microstructure evolutions. In addition to modeling, in situ DTEM experimentation combined with post-mortem analysis will be conducted on hypo-eutectic Al – Cu alloy thin films with higher Cu content than 4 at.% Cu and also for hyper-eutectic Al – Cu alloy thin films. This enables experiment-based elucidation the effect of Cu content on the rapid solidification behavior of Al – Cu alloys across the composition range for hypo- and hyper-eutectics. This facilitates a more comprehensive comparison between pre-existing data and results obtained through in situ DTEM observation.

Specifically, the following hypotheses are posed:

i. The rapid solidification process in pure Al thin films is dominated by the in-plane heat conduction through the metal layer.

ii. Overall the characteristic features of microstructure evolution of hypo-eutectic Al – Cu alloys with higher Cu content, 4 at.% ≤ Cu content ≤ 17 at.%, would remain similar to that in Al – 4 at.% Cu.

iii. Increasing the Cu content in hypo-eutectic Al-Cu alloys reduces the melting point will result in longer incubation time prior to on-set of directional rapid solidification crystal growth.

iv. Increasing the Cu content in hypo-eutectic Al-Cu alloys will introduce quantitative modification of the rapid solidification process, while maintaining overall characteristics (also see ii.).

v. Crystallographic effects might still affect the rapidly solidified microstructure after solidification completes, e.g., pre-existing texture in the as-deposited films may or maybe not be inherited in the rapidly solidified microstructure or preferred crystal growth orientations.

vi. Hyper-eutectic Al – Cu alloys could exhibit very different microstructure evolution during rapid solidification after pulsed laser melting compared to hypo-eutectic Al – Cu alloys. This could present in a) longer incubation times, b) fundamentally different stages of crystal growth modes and associated microstructure development and c) different characteristics in the crystal growth rate (solidification front velocity) evolution, since the primary phase becomes θ-$Al_2Cu$ phase upon solidification. The latter are expected to be attributable to limitations and constraints associated with faceted crystal growth (solidification) of the chemically ordered θ-$Al_2Cu$ phase relative to the situation of α-Al being the primary solidification product, which grows with an atomically rough interface.

The proposed research project will deliver an evaluation of these hypotheses by accomplishing the following objectives:

- Computational modeling of the rapid solidification process in metallic thin films upon laser melting that can be verified by quantitative metrics obtained from experimental results.
- Direct observation of the morphology and morphology evolution of the liquid – solid interface and measurements of the interface velocity in pure Al and Al-Cu alloys.
- Clarify the influence of constitutional effect and crystallography on laser induced transient transitions and resultant microstructures by combining in situ DTEM observation and post-mortem analysis.

Numerous factors can affect the melting and re-solidification of metallic thin films upon laser heating. By analyzing the experimental data and modeling results, the key factors (e.g. crystal structure, crystal orientation, composition, thermal properties of materials) that govern the transient transitions and resulting microstructures will be determined.

# 3.0 BACKGROUND AND LITERATURE REVIEW

## 3.1 RAPID SOLIDIFICATION IN METALS AND ALLOYS

Solidification is a fundamental process that dictates the initial microstructure and properties of naturally occurring and engineered materials, especially in fabrication and processing of metals and alloys. Thus, it has been extensively studied and several solidification models and mechanisms have been established for a variety of systems under different conditions [1,38].

Rapid solidification has become a topic of significant interest as it is capable of producing kinetically modified solidification microstructures that are attractive for many practical applications and several rapid solidification processing methods were developed [39]. Three widely used processing methods to achieve rapid solidification in metals and alloys are illustrated in Figure 2. The cold spinning wheel used in melt spinning is much larger than the incoming hot liquid metal, which enables production of rapidly solidified thin metallic ribbons. Gas-atomization processes are usually used to fabricate metal powders and rapid solidification conditions are achieved by the small size of the metallic powders and strong convection around the particles induced by the blowing gas. The solid base-material part of the bulk component in electron beam or laser beam induced surface melting can act as a large heat sink and a thin surface layer with rapid solidification microstructures can be created.

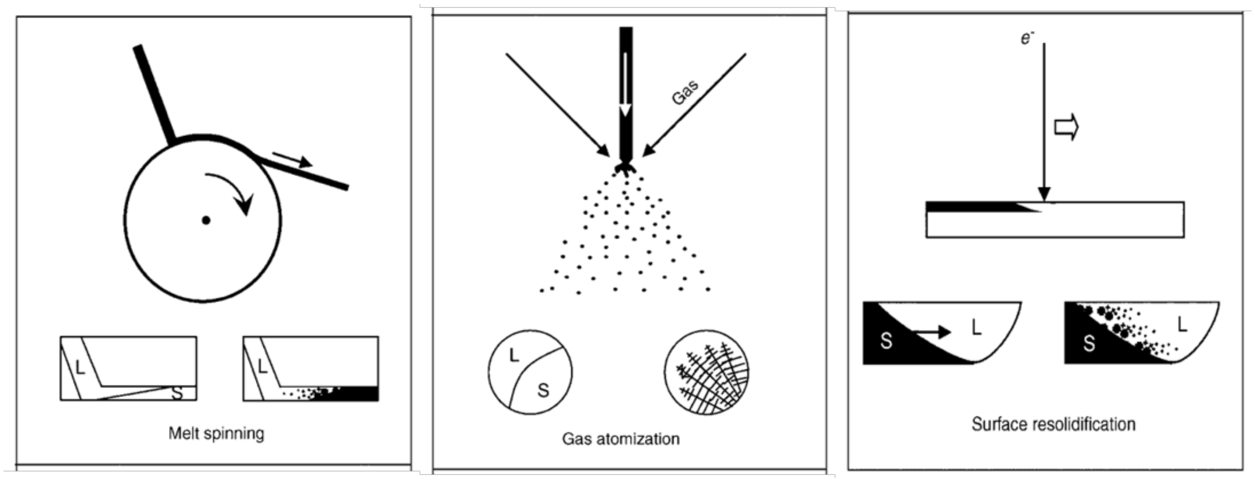

**Figure 2. Three types of processing methods used to produce rapidly solidified materials illustrated in** [39]

Typically, for metallic materials, rapid solidification is defined as the process of liquid-solid transformation for conditions that result in velocity of the advancing solidification front larger than 0.01 m/s. The high interface velocity is usually made possible by large undercooling of the melt or existence of an efficient heat sink in the vicinity of the migrating interface, both of which enabling rapid removal of heat at the solidification interface.

As solidification rate increases, the solidifying system increasingly deviates from full diffusional equilibrium and transitions to local interfacial equilibrium and then to metastable local interfacial equilibrium and eventually to interfacial non-equilibrium. For rapid solidification, previously proposed solidification mechanisms based on equilibrium and steady-state approximations no longer hold valid. Numerous researchers attempted to establish more advanced theory or models that take non-equilibrium and kinetic parameters into consideration. For instance, Aziz and Kaplan proposed the continuous growth mode (CGM) to describe the interface response during rapid solidification [40,41]. The CGM theory introduces the solidification velocity dependent non-equilibrium partition coefficient, K(v), defined as the ratio of solute composition in the solid, $C_S$, to that in the liquid, $C_L$, at the interface. For dilute alloy systems, it can be calculated as follows:

$$K(v) = \frac{K_e + (\frac{v}{v_D})}{1 + (\frac{v}{v_D})}$$

where $K_e$ is the equilibrium value of K(v) that can be obtained from the equilibrium phase diagram, $v$ is the interface velocity and $v_D$, the diffusive speed, is the ratio of $D_i$, inter-diffusion coefficient across the liquid-solid interface, to the interface thickness δ. So, $v_D$, is a metric of the diffusivity in the boundary layer in the liquid adjacent to the transformation interface. As the only free parameter in $K(v)$, the value of $v_D$ has usually been determined by applying best-fit methods to measured $K(v)$ relations. The validity of $v_D$ was then assessed by comparing experimentally measured parameters with theory predicted values of same parameters [42]. Although reasonable agreement between the experimentally determined $K(v)$ and that predicted by CGM has been reported by Kittl *et al.* [43] for interface velocity values lower than 1m/s, theoretically calculated $K(v)$ exhibited clear deviation from the experimental data when interface velocity exceeded 1 m/s (see Fig.9. in Ref. [43]). In addition, modification of $K(v)$ is necessary for more concentrated alloy systems and for non-planar solidification interface morphology conditions. The validity of such modified theories needs to be verified by further experimental observations.

## 3.2 CHARACTERIZING RAPID SOLIDIFICATION USING CONVENTIONAL IN SITU METHODS

In order to facilitate theoretical interpretation of rapid solidification processes and validate proposed models regarding rapid solidification, various in situ and post-mortem characterization efforts aiming at correlating solidification conditions and resultant microstructures have been performed in the past [43–46]. Several examples of them will be described in this section.

### 3.2.1 High-Speed Imaging

Monitoring rapid solidification utilizing light-sensing devices and high-speed cinematography is one of the earliest developed techniques to investigate rapid solidification processes in undercooled metal and alloy melts [47,48]. Later studies focused on the refinement of the experimental set-up to allow for more accurate observations and measurements. For example, Y. Wu *et al.* [49] used photodiodes combined with a digital oscilloscope to determine the solidification morphology and solidification velocities of undercooled quartz-encapsulated nickel ingots.

Another widely used method has employed the electromagnetic levitation technique to control the under-cooling and document the solidification morphology and solidification velocities during rapid solidification of metal and alloy melts [25,44,50–52]. The experimental set-up is similar to previous techniques (illustrated in Figure 3) but the levitation method allowed increased high undercooling of the melt with the absence of nucleants [53].

The melt of a pure metal or alloy is levitated in an electro-magnetic field and the temperature of the melt is measured by a pyrometer. In order to trigger nucleation in the melt, a needle made of the same material as the sample was employed. The needle is also part of a resistance-capacitance (RC) electrical circuit. The capacitance of the RC-circuit changes drastically when the needle touches the melt and initiates solidification and the time, $t_1$, is recorded as the initiation of the solidification.

With the set-up described above, it was possible to correlate the solidification velocity with the extent of undercooling and also the liquid-solid interface morphology. These prior efforts demonstrated that the solidification velocity increases with increasing super- or undercooling and the behavior agrees with what was predicted by previously proposed theories to a certain degree (as shown in Figure 4) [53–55].

However, there are inherent drawbacks of these methods: i) The material systems investigated were mostly limited to magnetic pure metal or very dilute solid solution binary alloys. ii) The temporal resolution of the data sets was at the µs-level due to the limitation of the sensing electronics and iii) the spatial resolution was limited at the mm-level at best because the images were recorded by optical cameras. In addition, these studies focused on the influence of very strong undercooling at interface, which might not be realistic for many rapid solidification processes.

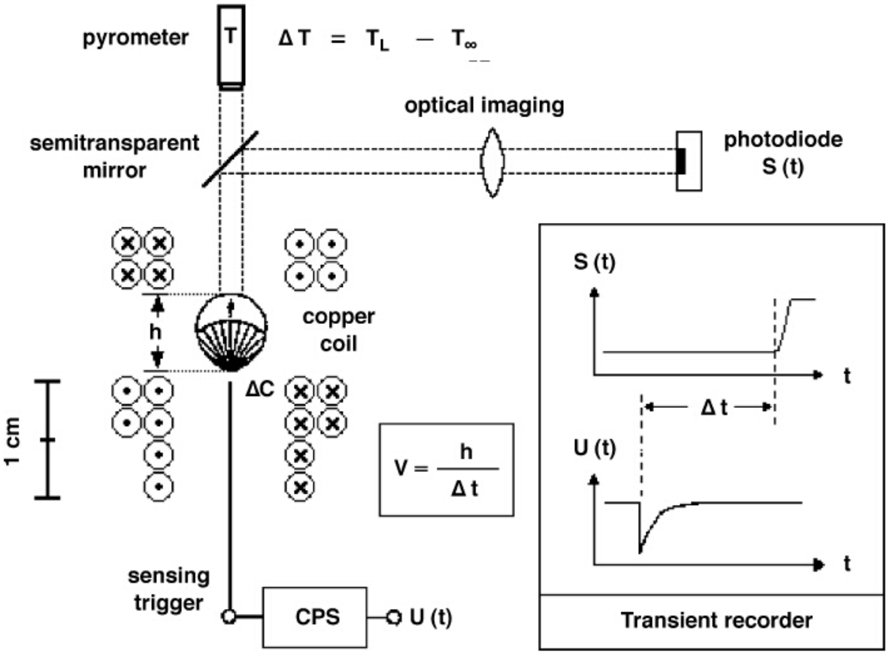

**Figure 3. Experimental set-up for monitoring the solid-liquid interface morphology and velocities during rapid solidification of the levitated undercooled melts. Adapted from** [53]**.**

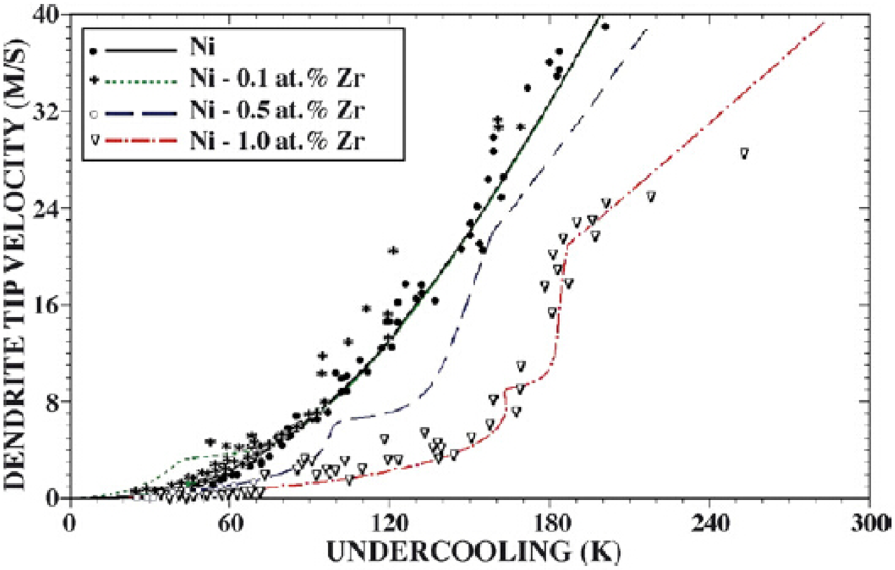

**Figure 4. Dendrite growth velocities as a function of undercooling measured for pure Ni (closed circles), Ni99.9Zr0.1 (stars), Ni99.5Zr0.5 (open circles) and Ni99Zr1 (triangles) compared with predictions calculated by sharp interface model (solid line). Adapted from** [53]**.**

### 3.2.2 Transient Conductance and Reflectivity Measurement

The development of various time-resolved measurement techniques enabled study of transient processes with micro-second to nano-second temporal resolution [56–59]. J. Kittl *et al.* reported research on pulsed laser induced melting and rapid solidification in thin film Si–4.5 at.% As and Si–9 at.% As samples [43,45]. Since the electrical conductivity and reflectivity increases as the Si-As samples melts and the electrical conductivity of the sample is dependent on its temperature, it was possible to utilize transient conductance measurement (TCM), time-resolved reflectivity measurements (TRR) and time-resolved temperature measurements to determine melt depth d(t), duration of melting and solidification, solid-liquid interface temperature and solid-liquid interface velocities v(t). The experimental configuration is schematically shown in Figure 5.

During solidification, the interface temperature, $T_i$, was determined from the recorded Pt resistor temperature, $T_{pt}$, and $\Delta T_{corr}$ can be estimated using an approximate solution to the heat flow equation:

$$T_i = T_{pt} + \Delta T_{corr}$$

and

$$\Delta T_{corr} \approx vH_f \left(d_{insul}/K_{insul} + d_{alloy}/K_{alloy}\right)$$

where v is the solidification velocity obtained from TCM, $H_f$ is the enthalpy of fusion, $d_{insul\ and}$ $d_{alloy}$ are the sickness of the nitride layer and the solid alloy layer, $K_{insul}$ and $K_{alloy}$ are the thermal conductivities of the nitride layer and alloy layer, respectively.

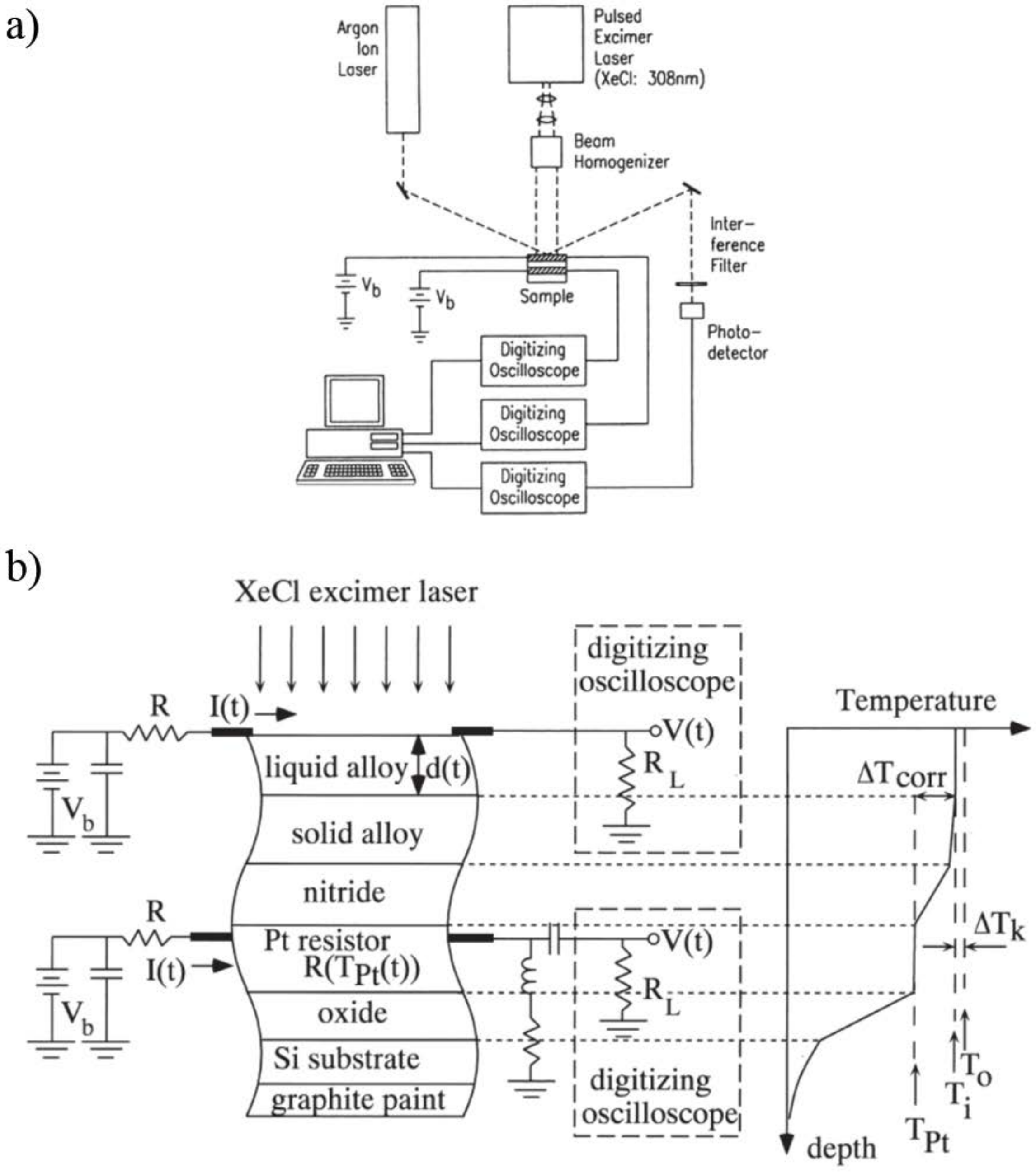

**Figure 5. Schematic of a) experimental setup of the transient measurements system and b) cross-section of sample structure. Adapted from** [43]**.**

Since the depth of the melted area can be easily measured and the time needed for solidification to complete can be measured by the change of reflectivity of Si-As (shown in Figure 6), the solidification interface velocity can be calculated simply by the melt depth divided by the total solidification time. By utilizing the experimental configuration described above, combined with numerical analysis that was necessary to determine the interface temperature, $T_i$, the congruent melting temperature of Si-As system was measured and the interface behavior was monitored at different velocities and used to provide experimental input to validate and compare the continuous growth mode (CGM) and various interface response models.

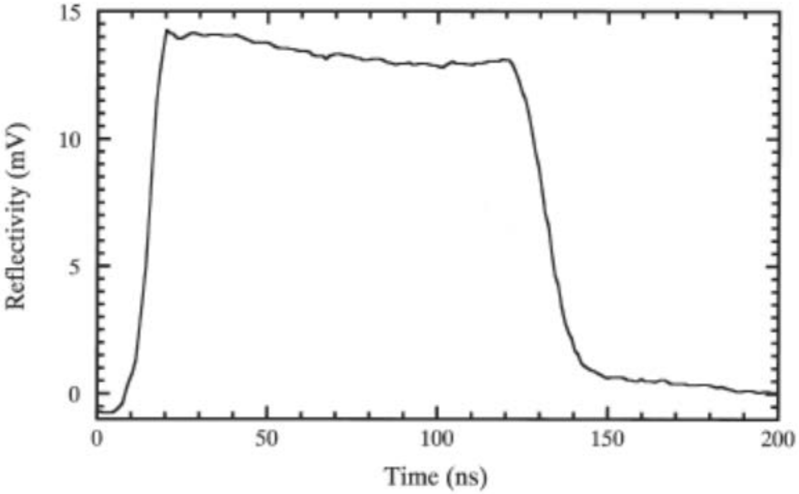

**Figure 6. Time-resolved reflectivity of Si-9 at.% As alloy showing changes when the surface melt and solidifies. Extracted from** [43]**.**

The CGM describes the interface velocity of alloys as following:

$$v = \frac{v_c(T_i)}{RT_i}\,(-\Delta G_{eff})$$

and

$$\Delta G_{eff} = \Delta G_{DF} = X_s \Delta\mu_B + (1 - X_s)\,\Delta\mu_A$$

where $V_C$(Ti) is a kinetic coefficient that is often expected to have Arrhenius form, R is the gas constant, and $\Delta G_{eff}$ is a molar Gibbs free energy change effectively driving solidification ($\Delta G_{eff}$ ,0 and n >0 for solidification). The “driving free energy” $\Delta G_{DF}$ is the change in Gibbs free energy per mole solidified, and $\Delta\mu_B$ and $\Delta\mu_A$ are the changes in chemical potential upon solidification for solute and solvent respectively.

After compiling all the measured interface velocity data at different interface temperatures for Si (for calibration purposes) and Si – 9 at.% As and comparing the data sets with what CGM and various other models predicts (shown in Figure 7), it was concluded that the CGM qualitatively explains the interface behavior during rapid solidification of Si – 9 at.% As alloy.

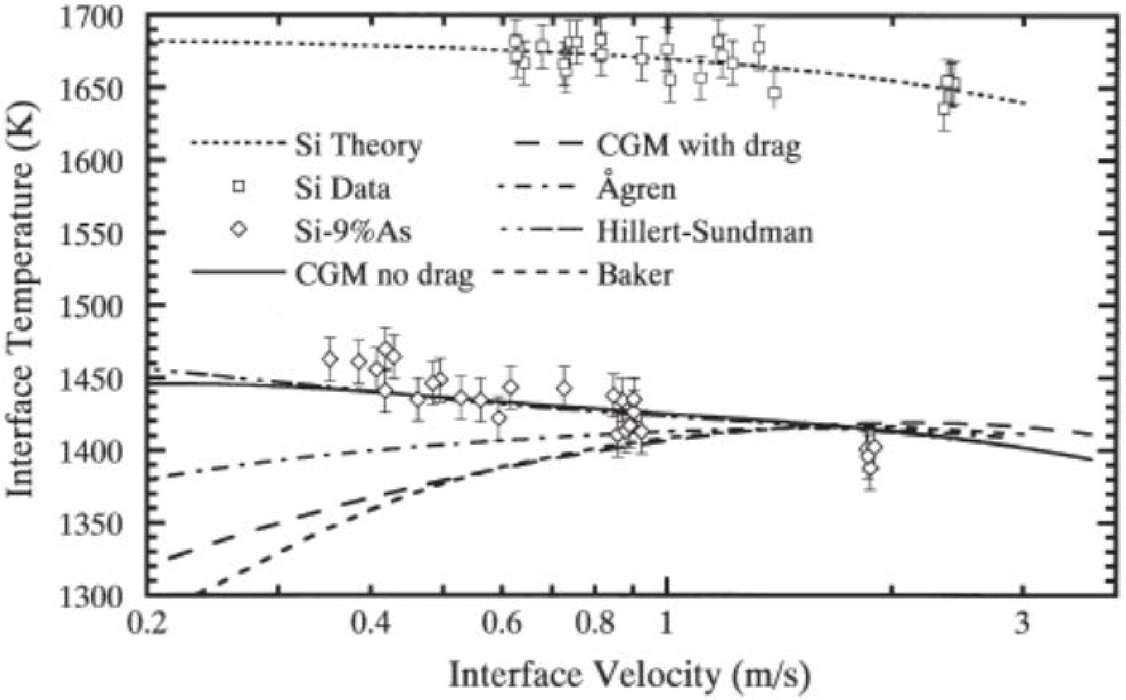

**Figure 7. Interface temperature vs. velocity response function. Theoretical pure Si curve taken from literature as discussed in text; calibration procedure forces pure Si data to fit curve. CGM without solute drag and Hillert–Sundman model fit alloy data; others do not. Reproduced from** [43]**.**

## 3.3 SURFACE REMELTING AND SOLIDIFICATION MICROSTRUCTURE SELECTION MAP

Besides investigations on rapid solidification processes using in-situ techniques (e.g. Section 3.2), a considerable amount of effort has been devoted to correlating microstructure and rapid solidification conditions based on post-mortem characterization and analysis. W. Kurz *et al.* have reported extensively on research on laser induced surface remelting and subsequent rapid solidification and accompanying microstructure evolution in various metal and alloy systems [35–37,60–65].

One system that was extensively examined was the Al-Cu alloy system [35–37]. In these studies, cylindrical Al-Cu alloy samples with various Cu concentrations were prepared by casting. A high-energy laser beam was then oriented at normal incidence to the surface of the Al-Cu alloy specimens. Surface remelting at controlled velocity of the laser beam was performed by rotating the cylindrical specimen about its axis at peripheral speeds, $V_b$. The local solidification rate, $V_s$, is related to $V_b$ by a simple plane geometry relationship

$$V_s = V_b \cos\theta$$

where $\theta$ is the angle between the vectors representing $V_s$ and $V_b$, as shown in Figure 8. This relationship implies that the local solidification rate, $V_s$, can be altered by changing the peripheral speed, $V_b$ (i.e., by varying the speed of the moving laser beam relative to the cylindrical specimen surface). Furthermore, the solidification rate also varies from zero to a maximum between the bottom and the top of the melt pool produced by a laser trace. Therefore, series of data on the relationship between the solidification condition and solidification microstructure could be obtained based on post-mortem microstructural investigations.

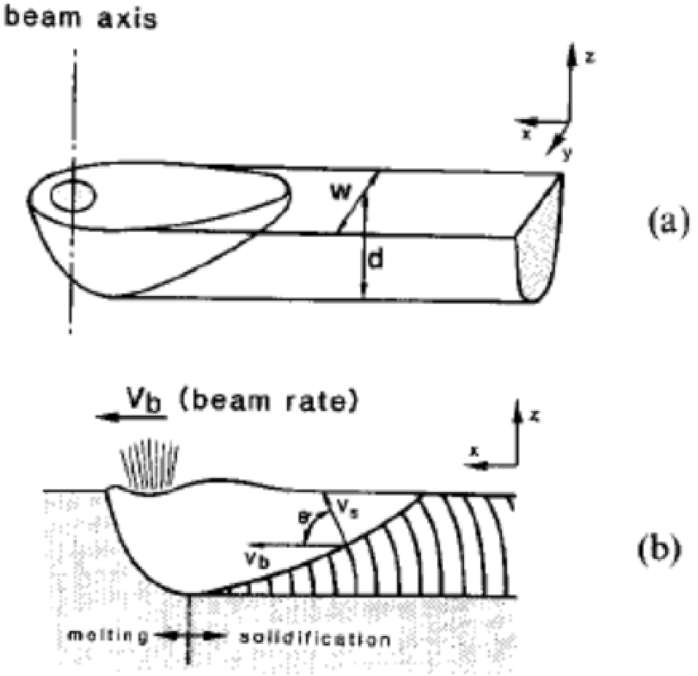

**Figure 8. (a) Illustration of the laser induced surface remelting. (b)Cross-section of the center plane of the laser remelted trace. $V_b$, the beam velocity can be related to local solidification rate $V_s$ by the angle between them based on the resultant microstructure. Extracted from** [37].

After laser surface remelting, subsequent post-mortem transmission electron microscopy (i.e. TEM imaging and diffraction analysis) was performed with the primary aim of correlating the local solidification rate and the corresponding microstructures. Distinct solidification microstructures in the surface melted and re-solidified samples were observed under different solidification conditions [35,36].

It has been shown by Gill *et al.* [34] that when $V_b$ is smaller than 0.5 m/s, the microstructure on the top surface of the laser trace is orientated perpendicular to the Z direction and therefore TEM micrographs of a cut in the X-Y surface plane can be used to calculate the local solidification velocities. However, when $V_b$ was equal or greater than

0.5 m/s, $V_s$ was observed to be no longer parallel to the specimen surface. As a result, the local solidification velocities cannot be calculated from the TEM micrographs of an X-Y cut. Therefore, it was necessary to adopt numerical simulations to estimate the solidification velocities in these situations.

By conducting a series of laser induced surface remelting experimentation, subsequent post-mortem TEM characterization and analysis and numerical simulations for Al-Cu alloys with a wide range of Cu concentrations, a Solidification Microstructure Selection Map (SMSM) for the Al-Cu alloy system that correlates velocities and resultant solidification microstructures as a function of composition was generated and shown as Figure 9. The different background patterns in the SMSM shown in represent the formation of morphologically distinct solidification microstructures over a range of compositions and velocities. The solid black lines dividing the regions indicate the existence of experimental observations, while the absence of such lines means that the position of the boundary between certain regions has yet to be identified.

The SMSM is a collective representation of the relationship between the solidification velocity and resultant microstructure for Al – Cu alloys that span a wide range of compositions (Cu concentrations). If correlation between solidification conditions and solidification velocity can be established, this map would be very useful for selecting the appropriate solidification conditions to generate desired final solidification microstructures. However, there are several shortcomings of the post-mortem analysis based SMSM due to the limited capability of the experimental methods used to generate the SMSM. First, the solidification velocity determination was based on reasonably justified assumptions regarding the geometric relationship to the laser beam scan speed when the solidification velocity values remained below 0.5 m/s. Secondly, these assumptions were found to become invalid for solidification velocities exceeding 0.5 m/s. Hence, for the solidification velocities larger than 0.5m/s, simulation was required to determine their magnitudes by calculation rather than from measurements. The solidification front velocities reported in the seminal works by of the Kurz group [34–36] on SMSM in Al-Cu are actually based on indirect observations and calculations rather than on direct measurements or observation of the interface during the re-solidification process. Hence, their validity needs to be examined, ideally by experimentation based on direct observations of the moving solidification interface. In addition, considering the velocity or y-axis of the SMSM is plotted on a log-scaled, the seemingly small error bars in the semi-log plot SMSM are in reality quite significant. Taking the third data point from the right to left of the SMSM for Al – 9 wt.% Cu, as an example, the lower bound of the estimated velocity for transition from cellular to banded morphology growth is about 1.2 m/s while the upper bound of the estimated velocity defined by the error can reach close to 3 m/s. This corresponds to an average velocity of 2.1m/s +/- 0.9m/s, i.e., an uncertainty range of ±43% in terms of relative error. Additionally, there is a notable lack of data points for the hyper-eutectic side of SMSM - the majority of data points concentrated on the hypo-eutectic side of the SMSM. The reason for the dearth of experiment based data for the respective critical velocities for the proposed crystal growth mode transitions were experimental difficulties with the solidification of the hyper-eutectic Al-Cu alloys. The primary phase formed during solidification of hyper-eutectic Al-Cu alloys is θ-$Al_2Cu$ phase, which frequently proved to be more brittle than the matrix during the thermo-mechanical stress cycles associated with the laser surface melting process resulting in crack formation in bulk hyper-eutectic Al-Cu alloys. Solidification cracking prevented direct correlations of the resulting microstructures with the laser beam scan speeds, as the cracks locally alter the thermal transport geometries.

With in situ experimentation that offers the required level of nano-scale spatio-temporal resolution, we will be able to obtain direct observation of the interface evolution during rapid solidification. This holds promise to deliver more precise solidification velocity determinations for a range of Al-Cu compositions. In addition, the thin film geometry we propose to use in this research would help to circumvent the solidification crack formation issues. As a result, the Movie - Mode DTEM use and thin film based pulsed laser melting induced rapid solidification experiments will facilitate validation of and improve upon the existing Al-Cu SMSM.

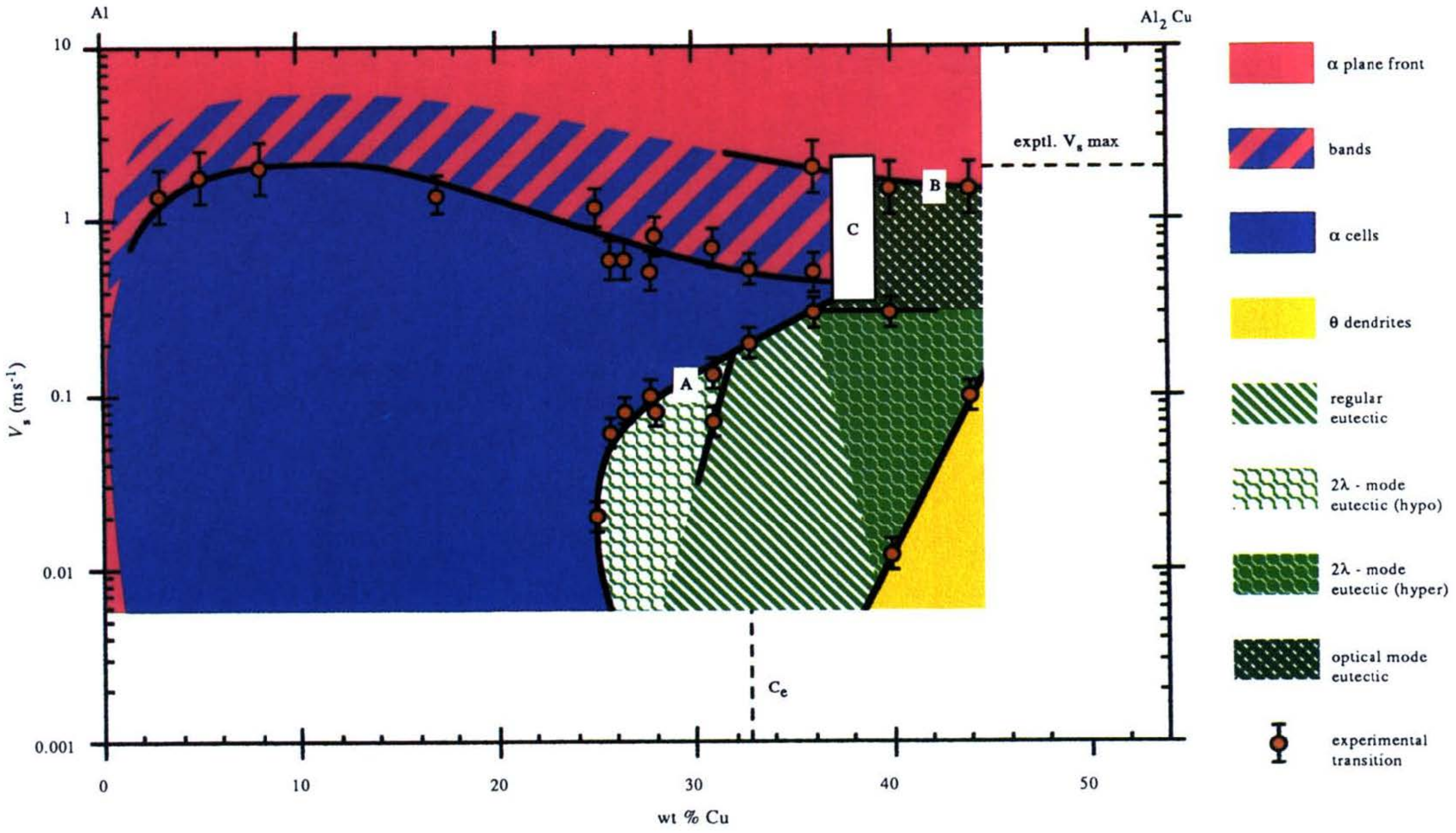

**Figure 9. Experimentally determined microstructure selection map for the Al-Al$_2$Cu under laser induced rapid solidification reported in** [37]**.**

## 3.4 LASER INDUCED RAPID SOLIDIFICATION IN METALLIC THIN FILMS

One common method used to study rapid solidification in metals and alloys has been the investigation of laser induced melting and re-solidification in samples with thin film geometry [45,66]. The combination of ultra-short laser pulses and minuscule material geometry lead to high cooling rates and hence steep temperature gradients at the liquid - solid interface. As a result, the migration of the transformation interface is extremely fast and the microstructural characteristics, such as interface morphology, grain size and crystal lattice orientation and composition profiles are strongly influenced by the solidification behavior.

Previous research [18,24,66–68] has shown that rapid solidification of metallic thin films introduced by pulsed laser heating yielded sheet-like polycrystalline microstructures in Cu, Au, Ag, Cr, Al and Al – Cu alloys. The microstructures were composed of high aspect ratio grains. A single laser pulse of defined geometry (a narrow line using wavelength in the deep UV range, 248 nm, in Ref. [18,24,66] or elliptical illumination using wavelength in the infrared range, 1064 nm, in Ref. [67,68]) of 15 – 30 ns duration was used to selectively melt part of the metal thin film using standard mask projection techniques.

The configuration of the experiment described above is schematically illustrated in Figure 10, for the situations of (a) metallic thin film supported by $Si_3N_4$ film and massive Si substrate and (b) nominally freestanding, electron-transparent $Si_3N_4$ membrane supported metallic thin film. In both situations, the metal melted completely in sections of the irradiated region and then solidification originated from the existing solid at the edge of the melt pool.

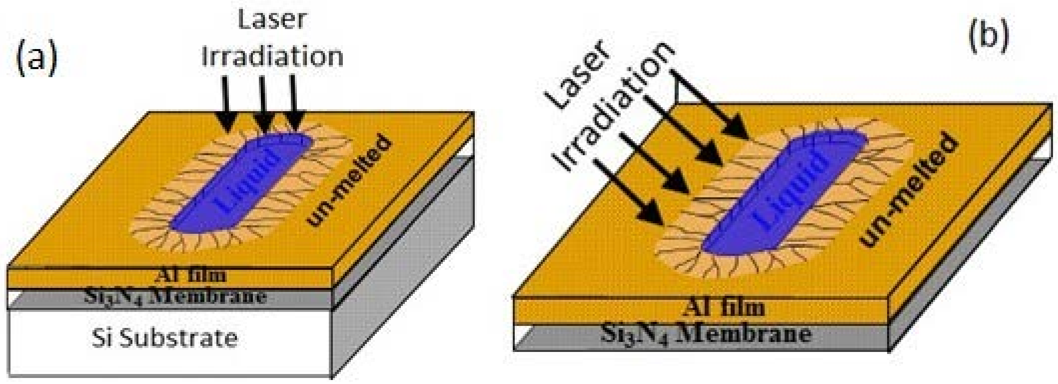

**Figure 10. Rapid lateral growth of existing solid into the melt pool from the edges of the melt pool. (a) Confined metal thin film (thickness ⩽ 200 nm) supported by thick substrate. (b) Metal thin film on free standing silicon nitride film. Reproduced from** [69]**.**

In contrast to a conventional solidification process, the well-known nucleation mechanism is not or not significantly involved in the rapid solidification process in metal thin films described above, because plenty of interface between the liquid metal and the un-melted solid of the same species exists, a situation akin to that encountered in the bulk experiments utilizing the laser beam melting described in Section 3.3. The rapid solidification in metallic thin films is analogous to post-nucleation or the crystal growth stage of the solidification process in bulk materials, where the solid material delineating the melt-pool provides seed crystals to initiate growth. The microstructure formed profoundly depends on the rate and direction of heat conduction, which is determined by the temperature gradient around the melt pool and thermo-physical properties of the surrounding materials. Thus, it is not unexpected that two distinct microstructures were observed in the experimental set-up described in Figure 10 [68,69].

In the first experimental configuration, up to four morphologically different regions were formed in the metal films on bulk Si wafer substrates (e.g. see Figure 11 a), whereas continuous lateral growth of elongated grains from the melt-pool wall to the center was observed in the absence of the bulk Si substrate support (e.g. see Figure 11 b). One rational hypothesis is to attribute the observed microstructural difference to the effects of the Si substrate on heat conduction. In the case illustrated in Figure 11 (a), the thickness of the Si wafer (~ 254 μm*)* is three orders of magnitude larger than the thickness of the Cu thin film (200 nm). As a result, the Si wafer acts as an infinite heat sink and the cooling rate is considerably increased in the vertical direction, which results in significant undercooling and nucleation from the substrate side in region III and IV (Figure 11 a). The lateral growth of elongated grains in regions I, II and parts of III is due to the dominance of heat conduction from the melt pool laterally through the adjacent, existing solid with a significant contribution from thermal transport through the metal horizontally and vertically into the solid bulk scale massive Si substrate [69]. Since nucleation requires additional activation energy, crystal growth from the pre-existing solid-liquid interface at the melt pool perimeter consumes fractions of the melt pool prior to successful nucleation in the eventually undercooled melt at the interface to the Si substrate in the central region of the melt pool occurs and results in competitive crystal growth of grains nucleated at the Si substrate interface to form region IV and those seeded at the solid metal delineating the melt pool to form regions I to III [70,71].

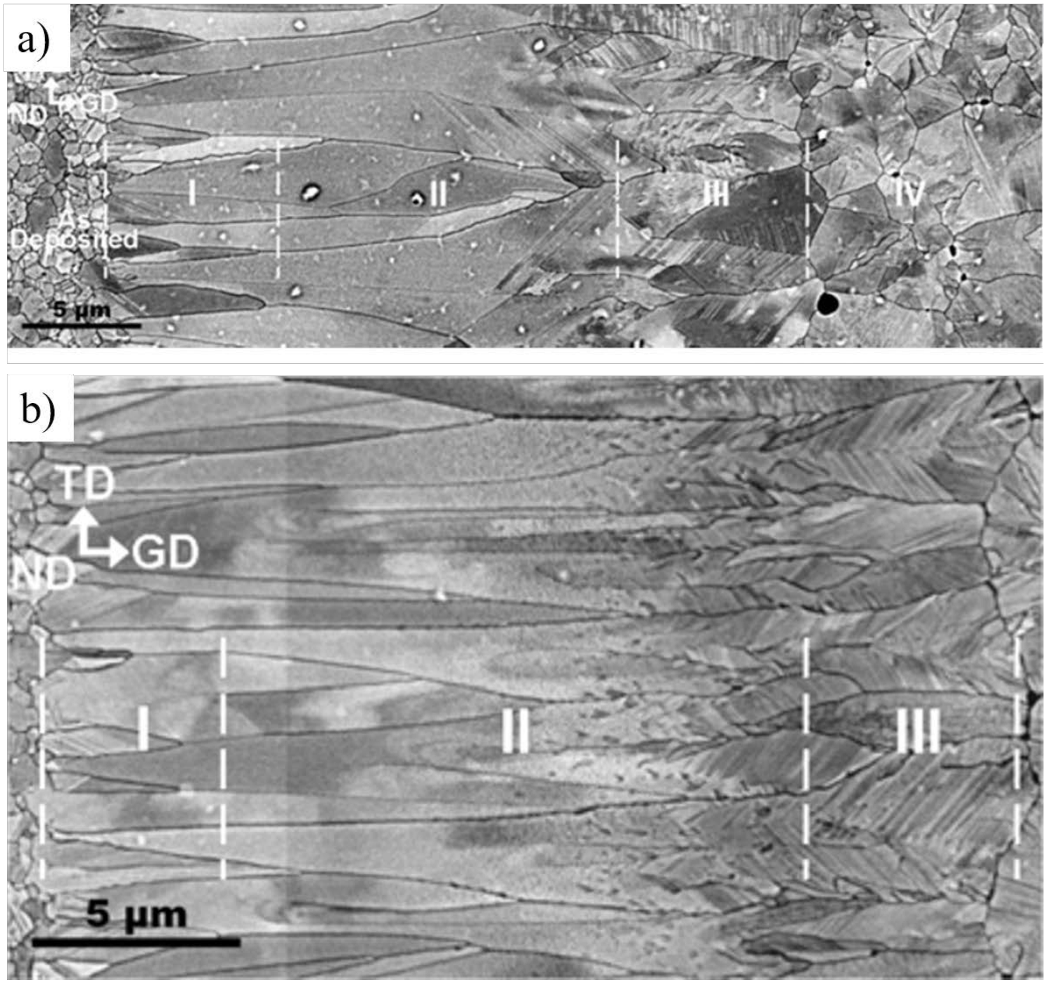

**Figure 11. (a) SEM micrograph of 200 nm thick Cu film on bulk Si wafer processed by pulsed laser, with four morphologically different regions. (b) SEM micrograph of 200 nm thick Cu film without bulk Si wafer processed by pulsed laser, with only three morphologically different regions, note the absence of the small grains (i.e. zone four in a)). After R. Zhong** [69]

## 3.5 IN SITU CHARACTERIZATION USING DYNAMIC TRANSMISSION ELECTRON MICROSCOPE

### 3.5.1 The dynamic transmission electron microscope

The discussion in the previous sections indicates that characterizing laser induced transient liquid – solid transformations remains challenging for conventional characterization techniques because it requires a combination of nanometer spatial resolution and nanosecond temporal resolution. As shown in Figure 12, most methods available for structural transitions studies fail to combine nano-scale spatial and temporal resolution. Among conventional characterization techniques, X-Ray based methods can provide a large field of view but only limited spatial resolution to ~ 1.5µm and their temporal resolution are no better than 150 ms. Conventional TEMs offer nanometer spatial resolution but relatively small field of view (depends on magnification and typically no more than 100 µm$^2$, the field of view at magnification of 25Kx, for instance, is ~ 20µm$^2$), and therefore they are limited in temporal resolution and can only be used to track slow transformations. Although recent years have seen significant improvements in the spatial resolution possible in the TEM, the temporal resolution of most microscopes is still limited to video rate, i.e. 30 frames per second, offering about 33 ms temporal resolution. Due to this rather limited temporal resolution, our understanding of transient processes in materials remains quite incomplete [29].

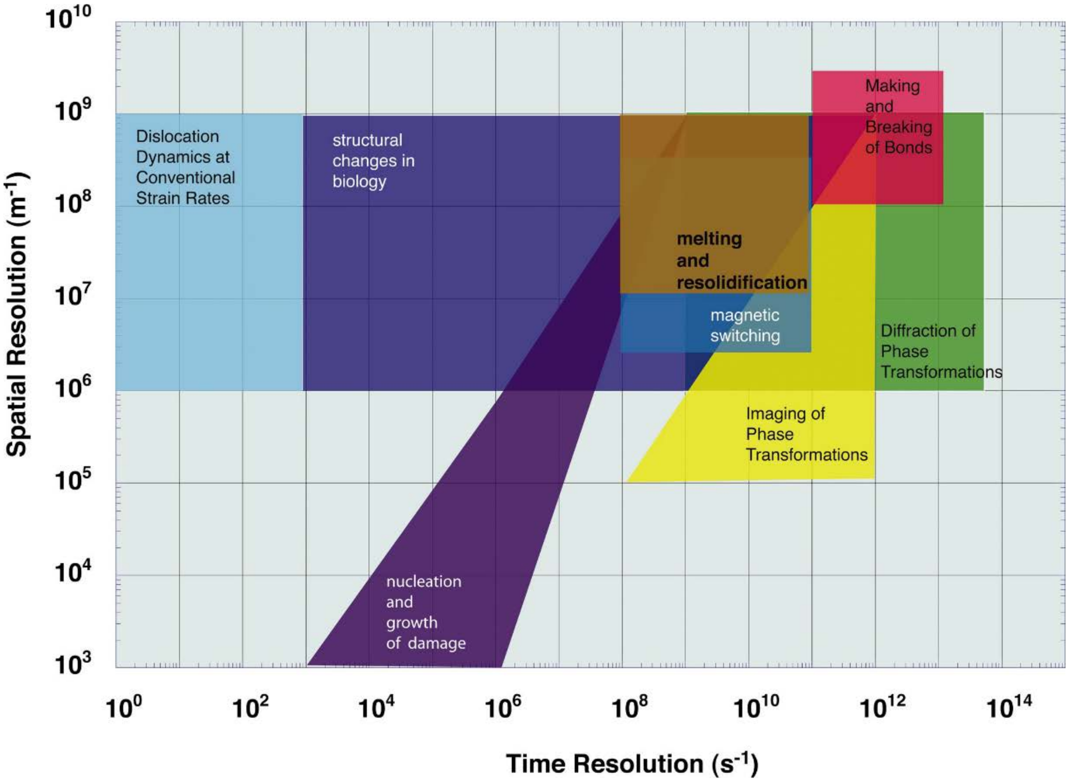

**Figure 12. Phenomena classified by spatial and temporal resolution. Adapted from** [29]**.**

Recently, a dynamic transmission electron microscope (DTEM) that can achieve nanosecond temporal resolution has been designed and implemented at the Lawrence Livermore National Laboratory (LLNL) [30–32]. The DTEM is modified from a standard JEOL 2000FX TEM and the high temporal resolution in the DTEM is achieved by replacing the common thermionic or field emission source with a photo-emission electron source. In this case, the temporal resolution is limited only by the ability to create a short pulse of photo-excited electrons in the source and this can be as short as a few femtoseconds.

The DTEM instrument together with the principle of the observation of transient processes in the pulsed laser illuminated sample is schematically shown in Figure 13 [32]. A Hydro-drive laser pulse triggers the transient process in the sample and then the sample is illuminated by a subsequent electron pulse. The electron pulse is emitted from the photo-emission cathode at a pre-set time delay, which can be as short as 15 ns. By in – situ imaging and diffraction study of the sample before and after the arrival of the process initiation pulse from the Hydro-drive laser system, information on many aspects of the transient process can be obtained. Similar to conventional TEM studies, the sensitivity of the measurement is determined by the signal-to-noise ratio in the image and/or diffraction pattern.

The DTEM has demonstrated its unique capability for characterizing transient processes with at least 10 nm spatial resolution and 15 ns temporal resolution (presented in Figure 14) via in – situ imaging and diffraction studies on α to β transformation in pure nanocrystalline Ti, crystallization of amorphous Si, ultra-short laser irradiation induced rapid solidification of Al thin film and other experiments [30–33,67,68,72,73]

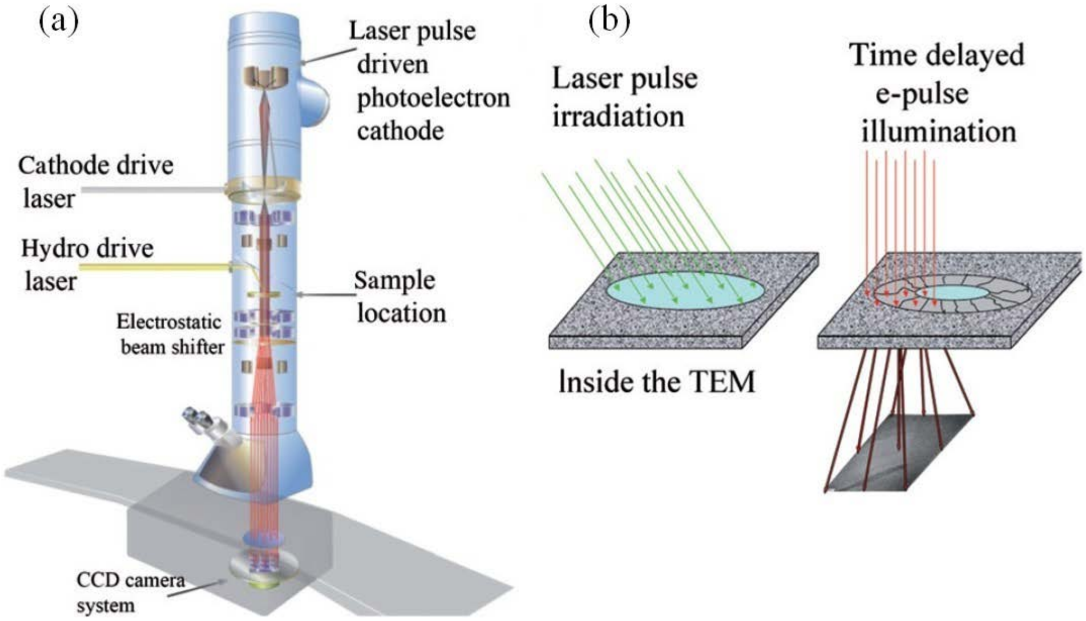

**Figure 13. (a) Schematic illustration of the DTEM. (b) Principe of rapid solidification initiated by pulsed laser irradiation and the time delayed electron beam capturing the migrating liquid - solid interface. Extracted from** [74]

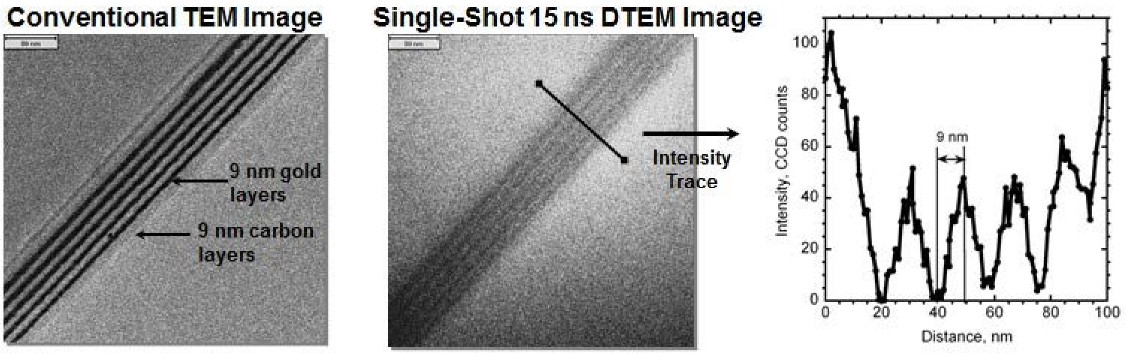

**Figure 14. Comparison between a conventional TEM image of equally spaced gold layers and carbon layers obtained from conventional TEM imaging and single shot DTEM imaging with 15 ns pulse duration. The full width at half max (FWHM) of the intensity line profile proves a spatial resolution of 9 nm. Extracted from** [33]**.**

For observation of rapid solidification, which is an irreversible transient process, it is necessary to generate enough electrons within a single pulse for imaging or diffraction pattern formation. This is called the “single shot approach” [30,75,76]. Thus, unlike conventional TEMs in which a continuous electron beam is used, the DTEM at LLNL is using a photo-emission cathode, which can generate electron pulses with duration of less than 15 ns and contains up to $2 \times 10^9$ electrons, as its illumination source. After the transient liquid –solid process initiated by the irradiation of the Hydro-drive laser on metallic thin films, electrons are emitted from the cathode upon the irradiation of the cathode drive laser at a pre-selected time delay and accelerated to 200 KeV. The electron pulses then arrive at the sample and enables acquiring a snapshot of the evolving rapid solidification process using a single electron sensitive detector, the charge coupled device (CCD) camera. By arranging a series of the snapshots in a time sequence with systematically varied delay times for acquisition after the Hydro-drive laser pulse, a “movie-like” sequence of images of the irreversible transition with nanosecond temporal resolution can be produced and unique information of the transition can be gained. For instance, the velocity of the migrating liquid – solid interface may be evaluated from measurements of the distance that the interface has migrated divided by the recorded time interval that passed between images recorded at different delay times. This information can be used for comparison with the interface velocity predicted through simulation and thereby validation by verifying the parameters and models used in modeling becomes possible.

### 3.5.2 Movie-mode DTEM

Recent upgrades to the DTEM permits a movie-mode image acquisition operation [77]. The multi-frame movie of a unique event provided by movie-mode DTEM allows the progress of rapid solidification processes to be explored in detail and offers the ability to record the motion of phase fronts, providing information of microstructural evolution at atomic-level that facilitates understanding of the dynamics and kinetics of rapid solidification. It brings unprecedented insight into the physics of rapid solidification processes from the initiation of solidification to completion. Due to several reasons, such as fluctuations of laser energy, change of starting microstructure after laser irradiation etc., possible uncertainties and errors are incorporated in the single-shot based DTEM experimentation and cannot be easily eliminated. The movie-mode DTEM experimentation greatly reduces the potential uncertainties associated with single-shot approach (see section 3.5.1) by obtaining a series of time-resolved TEM observations of the transient processes after a single Hydro-drive laser induced transition in the sample. Thus. Movie-mode DTEM experimentation represents a ‘step-function’ improvement for the nano-scale spatial resolution in-situ experimentation possible for irreversible transformations, such as the dynamics of rapid solidification.

The two core components enabling the movie-mode operation in DTEM are the arbitrary waveform generator (AWG) cathode laser system and a high-speed electrostatic deflector array (shown in Figure 15). The AWG cathode drive laser produces a laser pulse train with user-defined pulse durations and time delays between pulses that stimulates the photoelectron cathode to generate an electron pulse train, rather than a single electron pulse. Each pulse of a pulse train produced by the AWG modified cathode drive laser system captures an image of the sample at a specific time. A fast-switching electrostatic deflector located below the sample directs each pulse (image) to a separate patch on a large high-resolution CCD camera. At the end of the experiment, the entire CCD image is read out and segmented into a time-ordered series of images, i.e., a movie. The current technology produces 9-frame movies but future modification to the system should enable up to 25-frame movies with interframe delay times as low as 25 ns.

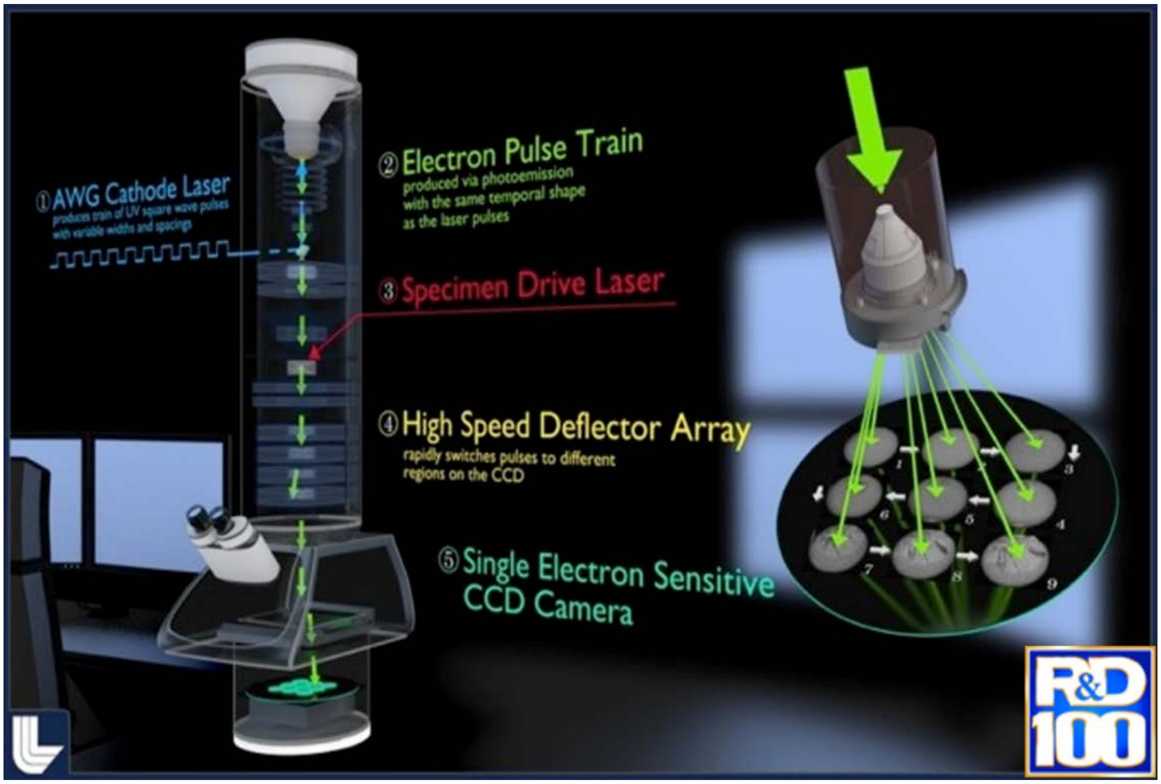

**Figure 15. The Movie-mode DTEM. Modified after**[77]**.**

## 3.6 MODELING OF RAPID SOLIDIFICATION IN METALS AND COMSOL MULTIPHYSICS

Abundant studies have been performed to simulate solidification phenomena across different scales: numerical modeling of industrial-scale casting [38,78], solidification in a confined lab-scale square cavity [79,80], surface melting and solidification [81–83] and dendritic growth at solidification interface during solidification [84–86] based on various assumptions and models have been performed. The modeling techniques and their applications to solidification processes have been reviewed by H. Hu *et al.* [87]. However, limited works has been done for rapid solidification in the presence of liquid superheat [88], which would be a physically suitable scenario for describing the laser induced rapid solidification in a thin film geometry. Therefore, we adapted a general heat conduction based enthalpy model proposed by N. Shamsundar *et al.* [89] to simulate the laser induced rapid solidification process in metallic thin films. The details of the model will be described in future sections.

In order to solve the coupled equations in the enthalpy model, the model was implemented in COMSOL Multiphysics, a finite element analysis (FEA) based simulation software. It has been proven to be capable of solving complicated coupled physics, for example, in laser induced melting and subsequent solidification processes [90–92]. Numerical solutions and profiles of certain physical parameters (e.g. heat transfer and temperature evolution of transient processes) that are not easily measured can be computed and displayed.

# 4.0 METHODS AND MATERIALS

## 4.1 THIN FILM FABRICATION

Electron-transparent Al-Cu thin films with various Cu concentrations (e.g. pure Al, hypo-eutectic Al – 11 at.% Cu, and hyper-eutectic Al – 18.5 at.% Cu) were be deposited on commercially available TEM grids with $Si_3N_4$ membrane support using a PASCAL Ultra-High Vacuum electron beam evaporation system and where appropriate additional magnetron sputtering for further in situ and ex situ characterization. The composition of the alloys films can be controlled by changing the evaporation rate of the two guns individually to achieve the desired composition ratio and film thickness. The chamber pressure was monitored during deposition and deposition was initiated only when the chamber pressure is below $7 * 10^{-8}$ Torr and the substrate temperature was at room temperature.

## 4.2 IN SITU DTEM EXPERIMENTATION

The sample setup for in situ DTEM experimentation is schematically shown in Figure 16. After putting the sample of interest into DTEM, a sample drive laser pulse was applied on the sample to initiate melting in the Al or Al-Cu film. Subsequent re-solidification will be rapid solidification due to the extremely fast heat extraction realized by the thin film geometry.

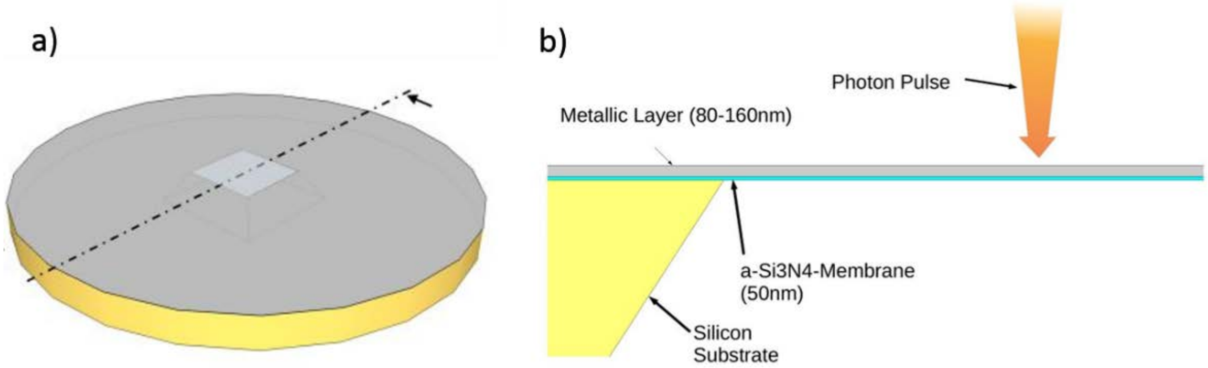

**Figure 16. a) Schematic illustration of a TEM grid with thin films deposited on top. b) Schematic of the cross section of TEM grid showing details of the layered structure.**

The laser pulse driven photo-electron cathode in the DTEM was then stimulated by a laser pulse train with pre-set time delay and time interval between each of the nine pulses of preselected pulse durations in the range of ~50ns to 250ns in order to generate the electron pulse train with its nine pulses to document the dynamics of the post-laser pulse solidification events. The pre-set time delay ranged from several tens of nano-seconds to more than one hundred microseconds and the time interval between individual pulses ranged from 500 ns to 10 μs, allowing observation of transient phenomena occurring during solidification as well as full documentation of a solidification process sequence. A high magnification mode of typically 1200X magnification was utilized to capture the morphological and structural details of the evolving transformation inter-face and a low magnification mode of typically 120X to 150X magnification were adopted to obtain the overview of the melt pool behavior and measure the instantaneous velocities as an average over the complete transformation front rather than at local points of observation. The former enables spatial resolution on the order of several tens of nanometers for the morphological changes associated with the crystal growth, e.g. for the liquid-solid interface, while the latter ensures that the overall behaviors of the transformation interface was captured accurately, enabling identification of local anomalies for instance, thereby avoiding non-systematic errors in velocity measurements.

## 4.3 EX SITU CHARACTERIZATION

The ex situ characterization encompasses two aspects: ex situ characterization before and after the pulsed laser induced rapid solidification.

Prior to the in situ DTEM experiments, conventional TEM (JEOL JEM 2100F and FEI Tecnai G2-F20) were used to characterize the thin film morphology, grain size, possible texture of Al and Al-Cu films, phase fractions and spatial distribution. The actual compositions of the Al-Cu films were also determined by using energy dispersive x-ray spectroscopy (EDS) and analytical TEM or scanning TEM instrumentation. The presence of secondary phases was examined using imaging and diffraction techniques of TEM.

In order to correlate the solidification conditions and resultant microstructures, post-mortem characterization was conducted on Al and Al-Cu films after in situ experimentation utilizing TEM and/or STEM. TEM based imaging, diffraction techniques such as precession electron diffraction (PED) and automated orientation image mapping (OIM) and composition analyses were performed to identify the solidification microstructures, presence of secondary phases and/or metastable phases, elemental composition, especially deviation from equilibrium states and potential orientation relationships.

Besides the TEM based techniques, scanning electron microscopes (SEM), such as Philips XL-30 and FEI Scios Dual-Beam FIB system, were also used to examine the thin film morphology and geometry of the melt pool when suitable. Since the evaporation processes and laser induced rapid solidification often introduce straining of the thin film, which leads to contrast change in the film or around the solidified microstructure, optical microscopy was found to be useful for quickly checking the film conditions and also the distribution and geometry of the melt pools in the film.

## 4.4 EX SITU LASER IRRADIATION

Some Al and Al-Cu alloy thin films were also irradiated with an ex situ laser system available at the University of Pittsburgh to examine the influence of laser geometry on the rapid solidification processes. The samples were irradiated with a single pulse from a 248 nm (KrF) excimer laser, projected through a single-slit Cu-mask with a five times demagnification. The mask is used to control the shape and dimensions of the laser beam at the sample and thus the size of the resulting melt pool. A small central part of the laser beam emitted by the KrF-excimer system was selected to obtain a uniform top-hat laser profile. The energy and geometry of the laser pulse was configured to initiate complete melting of metal thin films, resulting a melt pool of approximately 40 µm wide and 130 µm long. With termination of the pulse, the liquid starts to cool and rapid directional solidification commences. The experimental setup of the ex situ laser system and an example showing the geometry of a typical melt pool of an Al-Cu alloy thin film irradiated at room temperature are shown in Figure 17.

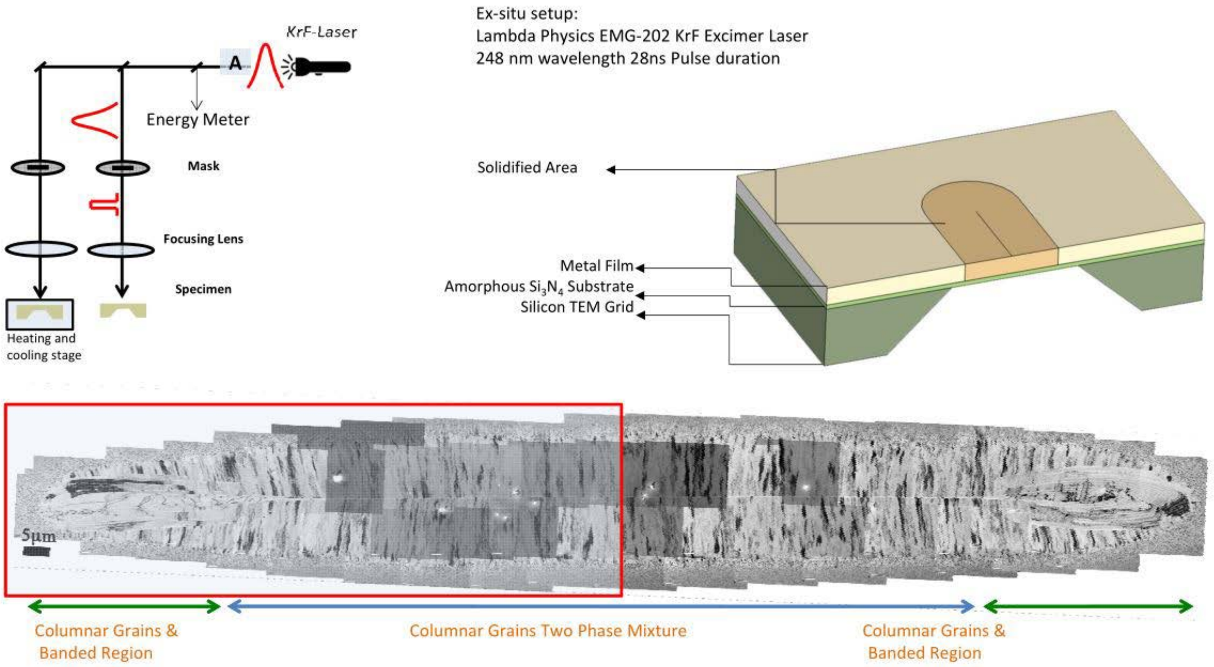

**Figure 17. Schematic of the ex-situ laser melting setup and an example of the observed re-solidified melt pool. Adapted from** [28]**.**

## 4.5 CONTINUUM MODELING IN COMSOL MULTIPHYSICS

Multi-physics finite element modeling has been performed in the COMSOL$^{TM}$ Multiphysics (version 5.1, COMSOL, Inc.) software environment using a modified enthalpy model, which solves the Stefan problem by adopting the enthalpy density as the dependent variable, for calculations of temperature evolution in the thin film sample after delivery of a laser pulse [87,89]. Details of the model and implementation of the model in COMSOL$^{TM}$ Multiphysics will be described and discussed in future sections.

The Gaussian laser pulse profile characteristics used in the model calculations were constrained to the experimentally utilized parameters regarding the elliptical shape and size on the sample, e.g. diameters of ~ 135μm and ~190μm along the minor and major axes. The model calculations used temperature independent thermo-physical properties for the solid phases and the liquid Al phase consistent with literature [93–95]. Thermal conductivity values used were in the range of 210 to 230 $Wm^{-1}K^{-1}$ for solid Al and equal to $90WK^{-1}m^{-1}$ for liquid Al, 150 $Wm^{-1}K^{-1}$ for Si, and 8 - 13 $Wm^{-1}K^{-1}$ for amorphous $Si_3N_4$. The model assumed no contribution from convection in the liquid to the heat transfer. The model accounted for the heat of crystallization of Al and considered the differences in densities and optical reflectivity for the incident laser radiation of the solid and liquid Al. A composite-model has been used for a phenomenological treatment of the relative contributions of the Al and amorphous $Si_3N_4$ layers to heat conduction for a simulated sample geometry comprising a 500 μm side length square area of initially solid Al equivalent to the 160 nm thick film with the 50 nm $Si_3N_4$ support layer and boundary conditions at the perimeter of an infinite heat sink representing the Si frame.

The effective contribution of the nitride layer to heat conduction after the laser irradiation pulse established an Al melt pool has been evaluated by varying the fraction of amorphous $Si_3N_4$ in the simulated composite sample. These calculations indicated that the small thermal conductivity of the amorphous $Si_3N_4$ resulted in thermal conduction being strongly dominated by the Al thin film during solidification. The experimentally determined metrics used to benchmark the model calculation results included the size of the melt pool of Al, the time delay between delivery of the laser pulse to the onset of directional rapid solidification, the total time to complete solidification and the temporal evolution of the solid-liquid interface velocity during solidification.

# 5.0 RAPID SOLIDICIATION OF ALUMINUM THIN FILMS

In order to successfully perform reproducible in situ DTEM experiments, pure aluminum was used as a model system to establish the procedures for in situ DTEM experimentation for observing rapid solidification in metallic thin films.

This chapter presents results obtained from systematically characterizing rapid solidification in Al and accompanying COMSOL® based multi-physics computational modeling by numerical calculations. Results based on in situ DTEM observations and post-mortem analysis will be correlated with the computer model calculation results to provide quantitative understanding of the rapid solidification process in Al thin film after delivery of the laser pulse. In addition, details of the enthalpy model used to model the rapid solidification process in Al and implementation in COMSOL™ will be described in this chapter. Comparison of the experimental data, quantitative metrics obtained from the in situ observations by DTEM and post-mortem analyses, and the modeling results will be performed, demonstrating the unique capability of in-situ DTEM experimentation to monitor rapid solidification processes and support validation of numerical models.

## 5.1 AS-DEPOSITED ALUMINUM THIN FILMS

In order to evaluate the microstructural changes resulting from pulsed laser irradiation induced rapid solidification, it is essential to document the microstructures of the specimens prior to laser irradiation. Here the microstructure characteristics such as thin film morphology, grain size and possible texture of as-deposited Al thin films are presented in Figure 18 and Figure 19**.**

Figure 18 a) shows a typical BF TEM image of Al thin film prior to pulsed laser irradiation experimentation. The film is continuous and with a thickness of ~ 160 nm. The selected area diffraction patterns (SADP) of corresponding areas are shown in Figure 18 b). The two SADP in Figure 18 b) were obtained with two different tilt orientations of the thin film relative to the incident electron beam: the untitled condition at 0˚ (Figure 18 b) top) and a significant axial tilt at -25˚ (Figure 18 b) bottom). Notably, the diffraction ring intensities changed upon tilting of the thin film. Clearly the intensity of the most intense, the strongest diffraction ring in top of Figure 18 b) is associated with the (220) ring, while the strongest diffraction ring in the bottom of Figure 18 b) is the (111) ring. The continuous diffraction rings in top of Figure 18 b) also become arcs with tilting as shown in bottom of Figure 18 b. Figure 18 c) displays the sum intensity from azimuthal integrated diffraction pattern profiles, corresponding to the diffraction rings in the SADP for the two different specimen tilts and the relative shift of diffraction intensity from the {220} ring to the {111} ring is clearly illustrated in Figure 18 c), which indicates the presence of {111} texture in the as-deposited Al thin films.

Figure 19 displays representative precession electron diffraction (PED) based TEM orientation image mapping (OIM) data sets obtained for the Al thin film in the as-deposited state. Consistent with the results offered by the conventional TEM technique, the inverse pole figure (IPF) maps generated from the OIM scans for the crystal directions parallel to the film normal Figure 19 a)) and the in-plane crystal directions parallel to the vertical y-direction Figure 19 b)) reveal a strong preference for alignment of the 111-poles parallel to the film normal direction, i.e., a fiber-type thin film {111}-growth texture.  No preferred orientations are observed for the crystal directions contained in the plane of the thin film Figure 19 b)). Using virtual BF and index quality map overlays (e.g. Figure 19 c)), the Al film grain size has been determined to be 160 nm ± 10 nm. Therefore, prior to the pulsed laser induced transformation during the DTEM experiments, the Al thin films show nanocystalline nature with an average grain size of ~ 160 nm with a {111}-type texture along the film normal. These structural characteristics are consistent with standard models for face-centered cubic (fcc) metal thin film growth-related structural evolution for substrate temperatures of room temperature [96].

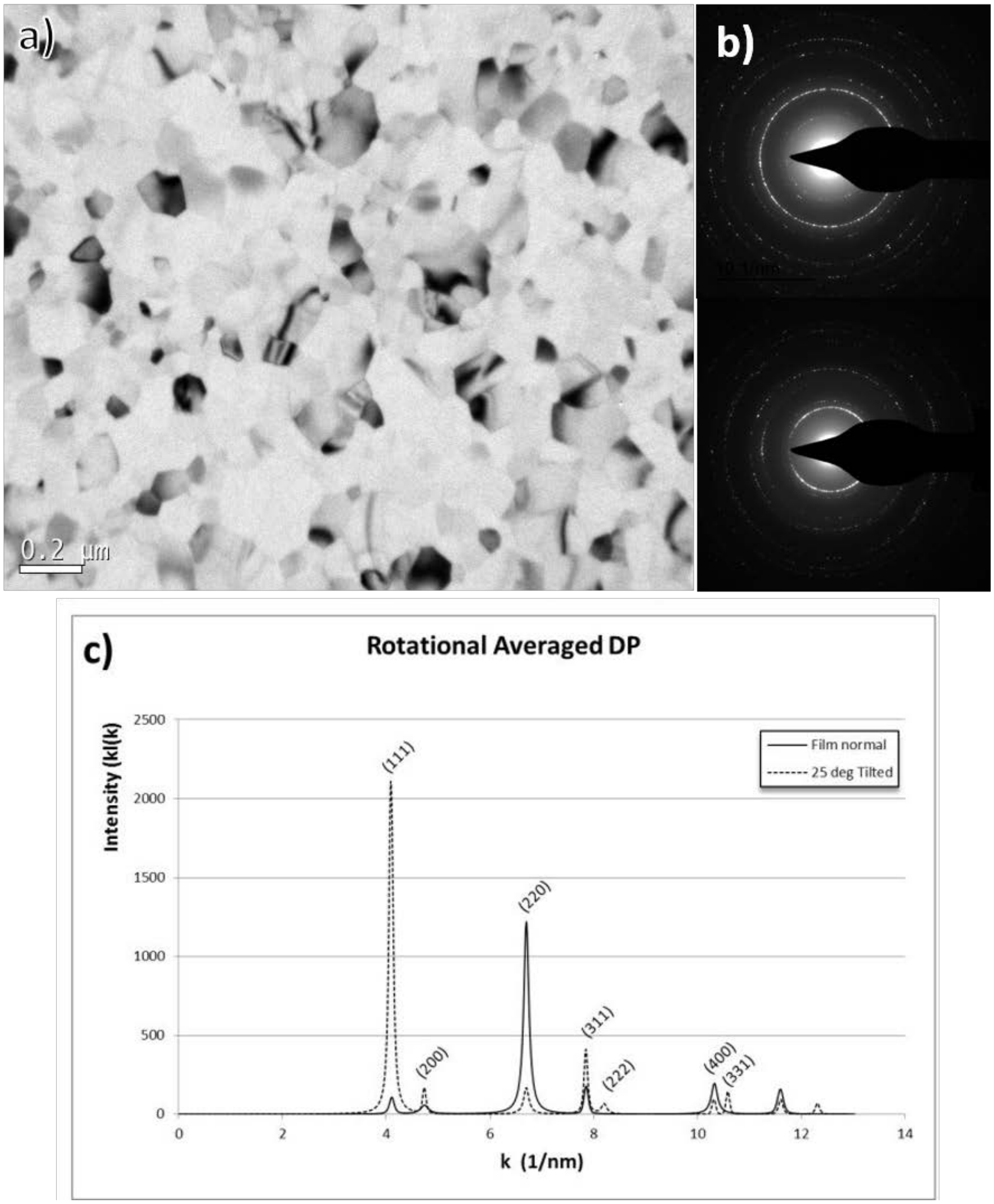

**Figure 18. a) Bright Field TEM image of as-deposited Al film. b) Top: Selected area diffraction pattern (SADP) of Al thin film without tilt. Bottom: SADP of Al thin film with -25$^{o}$ tilt. c) Rotational integrated intensity plot of the two SADP shown in b).**

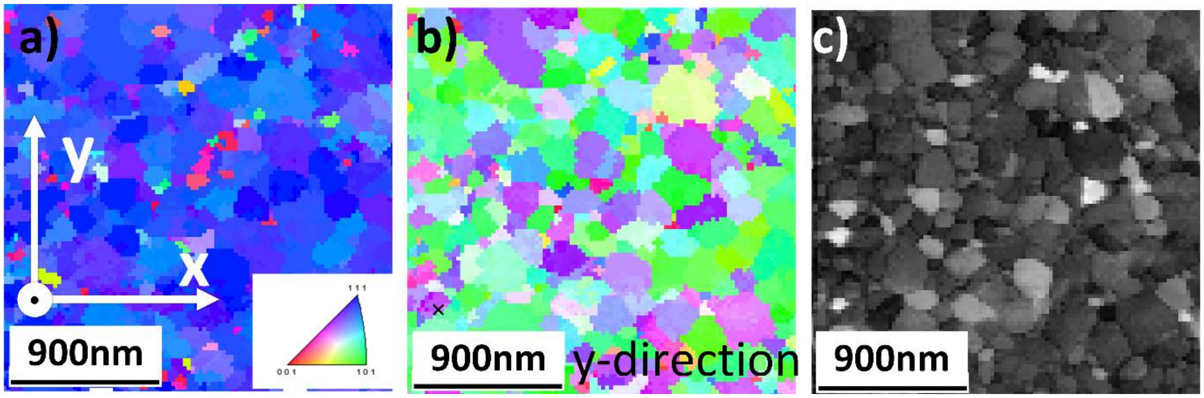

**Figure 19. PED TEM based OIM of as deposited Al film, (a) IPF based orientation map of film normal, (b) IPF based orientation map for in-plane vertical y- direction, (c) virtual BF image and index quality map overlay.**

## 5.2 CONTINUUM MODELING OF RAPID SOLIDIFICATION IN ALUMINUM THIN FILM

It is well known that temperature and its evolution during phase transformation processes is an important governing factor that usually has a significant effect on the behavior of the phase transformation processes. However, it is inherently challenging to measure the temperature evolution during rapid solidification, while performing in-situ DTEM observations. Therefore, enthalpy and heat transfer based modeling approach in COMSOL® Multiphysics environment was utilized to calculate the thermal field evolution during rapid solidification of Al under realistic conditions that are simulating the processes pertaining to rapid solidification experimentation in the DTEM. The successful model based calculations of the thermal field evolutions in the metal thin films after delivery of a laser pulse to induce melting will provide quantitative insights for more quantitative understanding of the rapid solidification process in the TEM specimen geometry. The details of the enthalpy model, implementation of the enthalpy model in COMSOL® Multiphysics and the modeling results in comparison with experimentally results will be presented and discussed in this section. Using the single component Al thin film samples avoids constitutional (compositional) effects from influencing the solid-liquid interface dynamics in response to the thermal cycles induces by the single laser pulse triggering the melting and subsequent re-solidification. The Al thin films exhibit liquid-solid and solid-liquid transformation sequences after deliver of the laser pulse that are entirely driven and controlled by the local temperature fields that develop. The in situ DTEM experiments uniquely provide experimental data for examining assumptions and for model benchmarking during the development of a suitable model for the calculation of the thermal field evolutions in the thin film specimens during RS.

### 5.2.1 The enthalpy model

The basic idea of the enthalpy method employed in COMSOL® Multiphysics is to solve the Stefan problem by tracking the enthalpy density as the dependent variable instead of the temperature. The Stefan problem considers the movement of a phase front under thermal conduction in the presence of a significant heat of transformation. Figure 20 illustrates the basic problem. While the enthalpy density $H$ is sufficient to determine the temperature *T* and the phase fraction *f*, these relationships are not in general invertible. *H*(*T*) and *f*(*T*) fail to be single-valued at $T_{melt}$. In order to track the boundary of the melt pool, the heat transport equation is reformulated in terms of *H* rather than *T*. The thermal diffusivity D is artificially smoothed and made to have a small finite non-trivial (not zero) value in the mixed-phase region, as shown in the Figure 20.

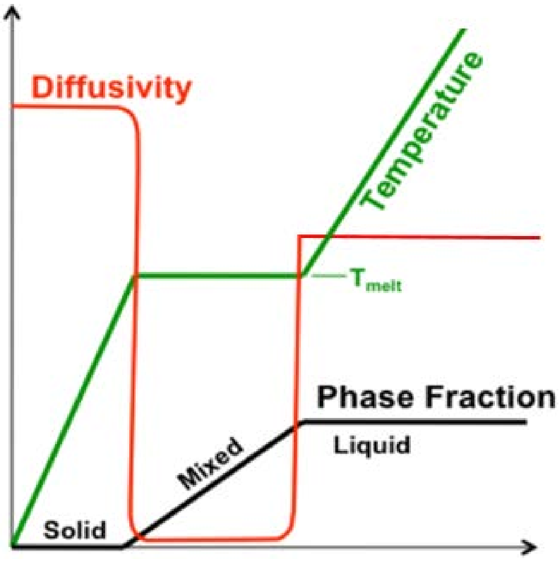

**Figure 20. Schematic relationship between the diffusivity and temperature of possible phases.**

For DTEM experiments, we typically have a supported thin film of total thickness *d* such that a characteristic time $\sim d^2/D$ for heat conduction in the normal direction is small compared to the time scale of the experiment. The thin films are also free to expand in the film-normal direction, while in-plane convection is assumed to be negligible, so that the mass-thickness is constant. Thus, a convenient formalism for these experiments is to define a purely two-dimensional problem, ignoring heat flux in the *z* direction, and calculating the enthalpy per area $H^{(A)}$ rather than per volume or per mass. Similarly, we define the heat capacity per area $c^{(A)}$. Then only an appropriate definition of diffusivity $D^{(A)}(H^{(A)})$ is necessary to solve the differential equation.

The usual heat equation is:

$$\frac{\partial H}{\partial t} = \nabla \cdot (k \nabla T)\,, \qquad (1)$$

where $H$ is enthalpy per unit volume, t is the time, k is the thermal diffusivity of a certain materials and T is the temperature.

For computational purposes, the sole independent variable needs to be $H^{(A)}$. First, we need to define $H^{(A)}$:

$$H^{(A)} = \sum_j \rho_j H_j d_j = \sum_j \rho_j H_j d_{j0} \frac{\rho_{j0}}{\rho_j} = \sum_j H_j d_{j0} \rho_{j0}\,. \qquad (2)$$

This is a sum over materials $j$ in the multilayered sample. Each material has an enthalpy per mass. $H_j$ and a thickness $d_j$ which is related to its initial (room-temperature) thickness $d_{j0}$ by the ratio of its initial density to its current density $r_j$. $H_j$ is a function of temperature, and therefore so is $H^{(A)}$. Since material properties are generally tabulated as functions of temperature and not enthalpy density, this function need to be constructed and then calculate its inverse $T(H^{(A)})$ in order to be able to calculate $k$, $r$, and $c$ as functions of $H^{(A)}$.

We also need the heat capacity per area,

$$\frac{dH^{(A)}}{dT} = c^{(A)} = \sum_j c_j d_{j0} \rho_{j0} , \qquad (3)$$

where $c_j$ is the usual heat capacity per mass, which of course is $dH_j/dT$. Lastly, we need an effective thermal conductivity, also scaled to the area, so that the differential equation becomes

$$\frac{\partial H^{(A)}}{\partial t} = \nabla \cdot (k^{(A)} \nabla T) = \nabla \cdot (\frac{k^{(A)}}{c^{(A)}} \nabla H^{(A)}) = \nabla \cdot (D^{(A)} \nabla H^{(A)}) . \qquad (4)$$

The appropriate definition of $k^{(A)}$ is

$$k^{(A)} = \sum_j k_j d_{j0} \frac{\rho_{j0}}{\rho_j} . \qquad (5)$$

This is because, to go from equation (1) to equation (4), we integrate in the foil-normal $z$ direction. Finally, we identify the effective diffusivity in this per-area formalism as

$$D^{(A)} = \frac{k^{(A)}}{c^{(A)}} . \qquad (6)$$

Ultimately, the function needs to be calculated is:

$$D^{(A)}\left(H^{(A)}\right) = \frac{\sum_j \rho_{j0} d_{j0} \frac{k_j\left(T(H^{(A)})\right)}{\rho_j\left(T(H^{(A)})\right)}}{\sum_j \rho_{j0} d_{j0} c_j \left(T(H^{(A)})\right)} , \qquad (7)$$

where all variable dependencies are made explicit. It is understood that, for the material layer undergoing the phase transformation, *k*, *r*, and *c* should be for the appropriate equilibrium phase.

In the mixed-phase region, $c^{(A)}$ diverges and the function is replaced with a small artificial diffusivity $D_{artificial}$, strictly for numerical purposes. Heat needs to be able to actually diffuse into the mixed-phase region so that the phase boundary can move naturally when heat diffuses into it. As a result, there will be an artificially diffuse edge between, say, the solid and the mixed-phase regions that spreads over a small number of grid spacing in the finite element model. If the solid part has a temperature gradient that, for example, creates a heat flux away from the boundary, the conservation law implied by equation (4) means that that heat has to come from the mixed-phase region right next to the interface. The enthalpy density of this region drops, and the phase fraction moves towards being purely solid, so that the diffuse-defined boundary moves a little bit in the correct direction and at the correct rate.

By assigning experimentally measured values or reasonable estimations to these parameters, results (e.g. the velocity of the advancing solid – liquid interface) will be calculated and used to evaluate the fidelity of simulation models.

### 5.2.2 Continuum modeling in COMSOL® Multiphysics

The enthalpy model for modeling the rapid solidification process in Al involve simultaneous couplings in the evolving material system of partial differential equations

(PDEs). Mathematically, it is often very difficult or even impossible to solve all the relevant PDEs for analytical solutions simultaneously. To describe and predict behavior of the evolving system, computational modeling based on numerical approaches is widely used to solve PDEs and many software codes have been developed. Among them, COMSOL® Multiphysics, a finite element analysis (FEA) based simulation software, has proven to be capable of solving complicated coupled physics, for example, in laser induced melting and subsequent solidification processes [90–92]. The software environment allows users to select pre-defined PDEs from modules for certain applications and/or enter user-defined PDEs that can describe a coupled system, which is convenient for users to customize and adapt certain physical models for specific situations. Therefore, COMSOL® Multiphysics was chosen for implementing and numerically solving the enthalpy mode described in the previous section.

With the formalism of the enthalpy model being established, the simulation space and a set of parameters need to be defined to implement the enthalpy model in COMSOL™ Multiphysics for describing the laser induced melting and subsequence solidification process we observe in situ by MM-DTEM experiments [28]. Based on the analysis in previous work by K. Zweiacker and co-workers [97], a safe distance of $\Delta X >$ 100 µm needs to be maintained for reproducible experimental results (the safe distance requirement will be elaborated in later section 5.3). Therefore, the simulation space is set to be 500 µm * 500 µm to reproduce and thus mimic the area of the electron transparent window.  The laser irradiation is projected at the center of the simulation space to ensure the modeling results will meet the safe zone requirement found experimentally and reliable as well. In this model, the energy of the laser is treated as the heat source (enthalpy source) that induced the melting. Therefore, the laser parameters need to be properly defined. For this purpose, a function, Hlaser, the energy per area deposited by the laser is defined. In addition, the driving force for the interface to migrate is assumed to be the in-plane heat transfer in the Al layer. Hence, the thermo-physical parameters of the materials involved (Al and $Si_3N_4$) at different states during the RS transformation need to be defined, including the density, thermal conductivity, and heat capacity of solid Al, liquid Al, and the $Si_3N_4$ support layer, and also specifying their initial thicknesses. Upon liquid to solid transformation occurring, or vice versa, the model should automatically change the parameters for Al when it melts.

The parameters associated with the phase transformation process, such as the heat of fusion and melting point of Al should also be included. The composite quantities appropriate for an enthalpy-per-area model, defined as $k^{(A)}$, $c^{(A)}$, and $D^{(A)}$ in section 5.2.1 can then be calculated.

Next, several parameters that need to be computed based on the evolving enthalpy that define the T(H) curve, including Deffective, the diffusivity used in the actual calculation of heat equation (1) in section 5.2.1, temperature and mass fraction of the liquid.

Finally, Tartificialspread and Dartificial are the two nonphysical parameters that need to be defined to make the diffusivity $D^{(A)}(H^{(A)})$ smooth enough that they are numerically compatible with the FEA algorithms.

These global parameters and variables along with their physical meanings are tabulated in the following Table 1 and Table 2.

**Table 1. Global parameters used in COMSOL Multiphysics**

| Parameters | Physical Meaning |
|---|---|
| **simboxsize** | Region for simulation. T = $T_0$ boundary condition on edges. |
| **lasersigmax** | RMS width in x direction of elliptical laser spot |
| **lasersigmay** | RMS width in y direction of elliptical laser spot |
| **laserenergy** | Total energy per pulse |
| **rsolid** | Assumed reflectivity of the sample |
| **rliquid** | Reflectivity of liquid |
| **asolid** | Absorption coefficient of solid |
| **aliquid** | Absorption coefficient of liquid |
| **rho0Al** | Standard density of solid aluminum |
| **d0Al** | Thickness of aluminum assuming standard density |
| **rho0Si3N4** | Standard density of support layer |
| **d0Si3N4** | Thickness of support layer at standard density |
| **rhoAlsolid** | Density of solid Al |
| **rhoAlliquid** | Density of liquid Al |
| **rhoSi3N4** | Density of substrate |
| **cAlsolid** | Heat capacity of solid Al |
| **cAlliquid** | Heat capacity of liquid Al |
| **cSi3N4** | Heat capacity of substrate |
| **kAlsolid** | Thermal conductivity of solid Al |
| **kAlliquid** | Thermal conductivity of liquid Al |

Table 2. Global parameters used in COMSOL Multiphysics-continued

| Parameters | Physical Meaning |
|---|---|
| **kSi3N4** | Thermal conductivity of substrate |
| **HfusionAl** | Heat of fusion of Al |
| **TmeltAl** | Melting point of Al |
| **ccompositesolid** | Heat capacity per area of the film stack when Al is solid |
| **ccompositeliquid** | Heat capacity per area of the film stack when Al is liquid |
| **kcompositesolid** | z integral of thermal conductivity when Al is solid |
| **kcompositeliquid** | z integral of thermal conductivity when Al is liquid |
| **Dcompositesolid** | Effective thermal diffusivity when Al is solid |
| **Dcompositeliquid** | Effective thermal diffusivity when Al is liquid |
| **Hfusionperarea** | Heat of fusion per unit area |
| **$T_0$** | Reference temperature for zero enthalpy |
| **Hsolidus** | Enthalpy per area just as the solid starts to melt |
| **Hliquidus** | Enthalpy per area just as the liquid starts to solidify |
| **Tartificialspread** | Approximate value of artificial spread of melting point |
| **Hartificialspread** | Degree of rounding of corners on smoothed D function |
| **Dartificial** | Artificial diffusivity in mixed-phase region |
| **$t_{offset}$** | Starts simulation and then ramps up diffusion over this time scale |

With the global parameters defined, the thermo-physical properties of the materials involved in the RS process that govern the phase transformation and heat transfer processes are set up. Next, the fundamental variable, enthalpy (as this is an enthalpy model), as well as the relationship between the temperature field, thermal diffusivity and the enthalpy evolution, need to be defined for calculating the enthalpy and temperature field evolution during the RS processes. The computed variables are expressed as following:

i. Hlaser: enthalpy per area deposited by laser

As previously mentioned, the enthalpy is introduced by the sample drive laser irradiation. However, the actual interaction between laser and polycrystalline metallic thin film is a very complex process [98–100]. Exploring the physics of this photon pulse interaction with the liquid and crystalline solid incorporating an electro-magnetism based description of the interaction between the sample laser and the Al thin film in the continuum modeling framework is beyond the scope of the current study. Hence, simplifying assumptions are made here to develop and implement effective solutions to address the modeling task for realistic calculations of the temperature field in the Al thin film after delivery of the laser pulse. Thus, here the enthalpy is treated as a laser energy delivered to the materials system at time 0 and defined as Hlaser, enthalpy per area deposited by laser, by the following expression:

Hlaser $= e^{(\frac{-x^2}{2} * lasersigmax^2 - \frac{y^2}{2} * lasersigmay^2)} * \frac{laserne nergy}{(2 * \pi * lasersigmax * lasersigmay)} * (1 - reflectivity)$

where *lasersigmax* and l*asersigmay* are the dimensions of the laser spot along the x and y direction, respectively. Laser energy is the total energy per pulse deposited all at once at time 0 and *reflectivity* is the variable that describes the optical reflectivity of the sample materials in different states (e.g. solid or liquid), as previously tabulated in Table 1.

The first term in the above formula is a two-dimensional Gaussian function, which describes the distribution of laser energy in the tow-dimensional sample plane to reproduce the Gaussian distribution of the sample drive laser used. The second term in this formula, $(\frac{laserne nergy}{(2 * \pi * lasersigmax * lasersigmay)})$, converted the total energy into a per area quantity to be utilized for this now two-dimensional model of the thin film sample.

ii. *Deffective*: the effective thermal diffusivity of material in the different states during the RS process

The thermal diffusivity is clearly dependent on the actual phase present, i.e., different thermal diffusivity needs to be correctly applied to Al in the solid and liquid states. Also, continuity needs to be ensured at the transformation interface to avoid singularities at the respective transformation boundaries during computations.

In order to achieve this, the effective thermal diffusivity, *Deffective*, with logic expression involved, is expressed as the following:

Deffective = (Dcompositesolid-Dartificial) * flc2hs((Hsolidus-H)/Hartificialspread,1) + (Dcompositeliquid-Dartificial) * flc2hs((H-Hliquidus)/Hartificialspread,1) + Dartificial

where the terms are tabulated as following:

**Table 3. Terms for Deffective**

| | |
|---|---|
| **Dcompositesolid** | kcompositesolid/ccompositesolid |
| **Dcompositeliquid** | kcompositeliquid/ccompositeliquid |
| **Hsolidus** | (TmeltAl-$T_0$)*ccompositesolid |
| **Hliquidus** | Hsolidus+Hfusionperarea |
| **Hartificialspread** | Tartificialspread*(ccompositesolid+ccompositeliquid)/2 |
| **Dartificial** | (Dcompositesolid+Dcompositeliquid)/1000 |

The function y = flc2hs(x,scale) computes the values of a smoothed version of the *Heaviside* function y = (x>0). The function is 0 for x<-scale, and 1 for x>scale. In the interval -scale<x<scale, flc2hs is a smoothed Heaviside function with a continuous second derivative without overshoot. It is defined by a sixth-degree polynomial.

For example, with the expression of Deffective defined above, when H > Hliquidus, the term ((Hsolidus-H)/Hartificialspread) < -1 and therefore flc2hs((Hsolidus-H)/Hartificialspread,1) = 0. Similary, the term ((H-Hliquidus)/Hartificialspread) >1 and hence flc2hs((H-Hliquidus)/Hartificialspread,1) =1. As a result, when H > Hliquidus, Deffective = (Dcompositesolid-Dartificial) * 0 + (Dcompositeliquid-Dartificial) * 1 + Dartificial = Dcompositeliquid, which means the liquid thermal diffusivity of the composite material is assigned to the material system when the enthalpy density is larger than the liquidus enthalpy.

Ultimately, the above expression would yield:

**Table 4. Deffective based on different enthalpy density**

| Enthalpy Values | Material State | Deffective Values |
|---|---|---|
| H < Hsolidus | Solid | Dcompositesolid |
| Hsolidus < H < Hliquidus | Transition-region | Dartificial |
| H > Hliquidus | Liquid | Dcompositeliquid |

And within the narrow region with width of Hartificialspread, diffusivity smoothly changed from Dcompositesolid to Dartificial (also Dartificial to Dcompositeliquid) through Heaviside function.

For example, the overview plot of Deffective over the x distance across the major axis of a melt pool at 4 μs after delivery of the laser pulse, the initial enthalpy, attained in a typical COMSOL$^{TM}$ simulation is shown in Figure 21. The enlarged view of Deffective around the “transition region” over the x distance across the major axis of a melt pool at the same time point is displayed in Figure 22. The different Deffective values of liquid and solid Al are correctly assigned to corresponding regions of the evolving material system.

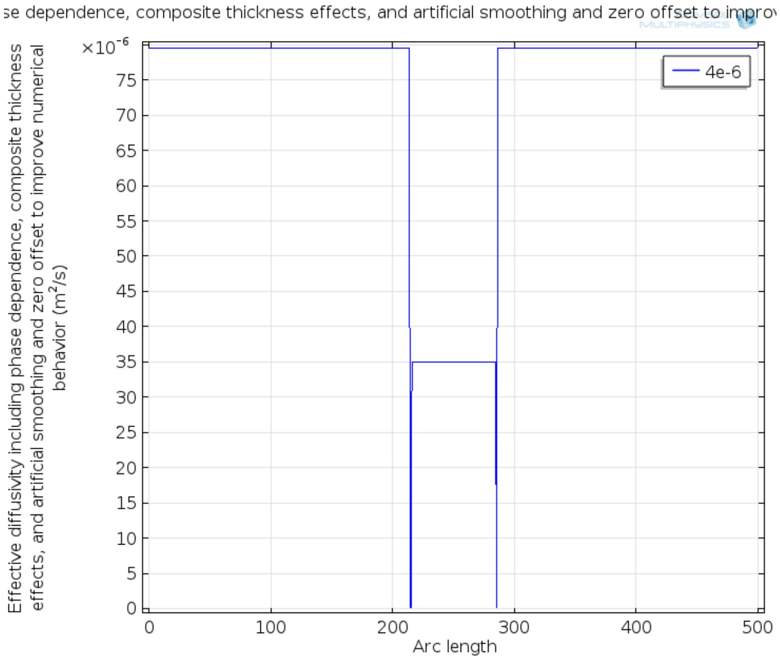

**Figure 21. Overview of Deffective across the major axis of a simulated melt pool at t = 4 μs**

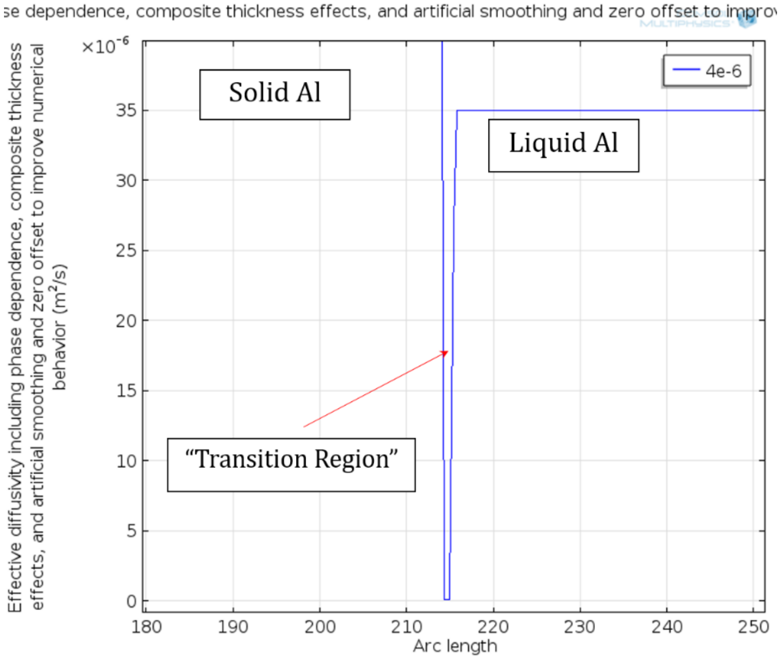

**Figure 22. enlarged view of Deffective around the "transition region" over the x distance across the major axis of a melt pool at t = 4 μs**

- iii. T(H): temperature calculated based on the enthalpy density at given point

T(H) = ($T_0$+H/ccompositesolid) * (H≤Hsolidus) + (TmeltAl) * (H≤Hliquidus) * (H>Hsolidus) + (TmeltAl+(H-Hliquidus)/ccompositeliquid)*(H>Hliquidus)

where $T_0$ is environmental temperature (300K), TmeltAl is melting point of Al (933K) and other parameters were previously defined. The (H ≤ Hsolidus) is a conditional expression: if H ≤ Hsolidus is satisfied then value of (H ≤ Hsolidus) will be 1 otherwise the value of the expression will be 0.

These would give:

**Table 5. Calculated temperature based on different enthalpy density**

| **Enthalpy Values** | **Material State** | **Temperature Values** |
|---|---|---|
| H < Hsolidus | Solid | T = $T_0$ + H/ccompositesolid |
| Hsolidus < H < Hliquidus | Transition-region | T = TmeltAl |
| H > Hliquidus | Liquid | T = TmeltAl + $\frac{H-Hliquids}{ccompositeliquid}$ |

iv. Meltfrac: mass fraction of liquid

meltfrac = ((H-Hsolidus)/Hfusionperarea) * (H>Hsolidus) * (H<Hliquidus) + (H ⩾Hliquidus)

The conditional expression is the same as described above and the value of meltfrac under different conditions will be:

**Table 6. Calculated mass fraction of liquid based on enthalpy density**

| **Enthalpy Values** | **Material State** | **Meltfrac Values** |
|---|---|---|
| H < Hsolidus | Solid | 0 |
| Hsolidus < H < Hliquidus | Transition-region | (H-Hsolidus)/Hfusionperarea |
| H > Hliquidus | Liquid | 1 |

With this implementation of the enthalpy model in COMSOL$^{TM}$ Multiphysics, it is evident that this model is indeed an enthalpy based model because all the computed variables are based on calculated enthalpy evolution for a given position in the two-dimensional simulation space. When H < Hsolidus, the "composite material" is solid and when H > Hliquidus, the "composite material" is liquid. When Hsolidus <H < Hliquidus, a mass fraction of liquid that is larger than 0 but smaller than 1 exists, which represents the "transition front" in the simulation.

This model also entails the following assumptions that we consider as reasonable, allowing significant reduction of model complexity and computation time while still capturing the physical essence of RS process:

i. Heat transfer in Z-direction is not taken into account:

   This assumption has been verified by the experimental observations for melt pools formed with properly placed laser irradiation. The thermo-physical parameters, such as heat capacity and computed variables are instead converted to area quantities.

ii. The convection of liquid during RS is not considered:

   Unlike in conventional casting where the amount of materials involved and the spatial dimension of the ongoing phase transformation are large, the material that undergoes rapid solidification in this study is thin film with 80 nm to 160 nm thickness and the solidification process completes within twenty microseconds for the Al. Therefore, the major driving force for rapid solidification and interface migration was expected to be the fast and highly directional in-plane heat transfer, not convention.

iii. The thermo-physical properties of Al at a given state remains constant: Physically, the thermo-physical properties, such as reflectivity, thermal conductivity and heat capacity are temperature dependent for liquid or solid Al, respectively [101]. However, it is very challenging to measure any of these changes during in situ experimentation and, again, the solidification completes within twenty microseconds. Therefore, it is not expected that the change of thermo-physical properties of liquid or solid Al during RS process would be significant enough to affect the RS process

## 5.3 IN SITU MM-DTEM EXPERIMENTATION AND MODELING OF RAPID SOLIDIFICATION IN ALUMINUM THIN FILMS

### 5.3.1 In situ DTEM experimentation and determination of solidification velocity

In parallel to the modeling efforts, systematic in situ MM-DTEM experimentation have been performed using pure Al thin films as the model system for establishment of reliable experimental methodology [28] to ensure reproducible experimental outcome and to provide experimental data for benchmarking the enthalpy model based continuum modeling in COMSOL$^{TM}$ Multiphysics.

Due to the geometry of the TEM grids used for in situ DTEM experimentation (see section 4.2), it was expected that the presence of thick silicon substrate in the TEM grids will change the heat extraction path. Therefore, a series of laser irradiation experiments were conducted to determine the “safe zone” for DTEM based in-situ pulsed laser irradiation experiments suitable for the study of the rapid solidification transformation dynamics. Five different locations at different distances from the border of the electron-transparent window of the TEM grids were selected to test the influence of the silicon substrate.

Figure 23 presents five low-magnification MM-DTEM image sequences that monitored the evolution of the entire melt pool for five different locations from #1 to #5 with different distance, $\Delta x$, to the silicon substrate. The entire transformation process was captured in each of the 20.4 µs duration in situ MM-DTEM image sequence. For melt pools produced by nominally identical laser irradiation pulses at the different locations from #1 to #5, by systematically varying the distances, $\Delta X$, from the edge of the thick Silicon support frame, it was expected the heat extraction should change gradually by the change of $\Delta X$ and hence affect the dynamics of the rapid solidification process during the transformation sequences observed in the experiments.

It can be clearly seen from Figure 23 that asymmetries in the melt pool geometry developing in sequence a) and b) and completion of solidification process before 17.85 µs due to the close proximity of the Si substrate affecting the heat extraction geometry. On the other hand, the melt pool geometry remains symmetrical throughout the solidification process in sequence c) to e) and the solidification process consistently finished between 17.85 µs and 20.04 µs as the last remaining liquid is visible in images corresponding to t = 17.85 µs. The actual time was not captured due to the interframe time delay used for this low magnification movie-mode. Hence, based on experimental observations, within the spatio-temporal resolution margins of the low-magnification in situ MM-DTEM experiments, it can be concluded that a safe distance of $\Delta x$ ($\Delta y$) > 100 µm from the edge of the electron transparent window is necessary for reliable and consistent observation of the pulsed laser irradiation induced melting and solidification dynamics for the Al thin films. More detailed analysis on the safe zone determination for in situ MM-DTEM experimentation can be found in reference [28,97].

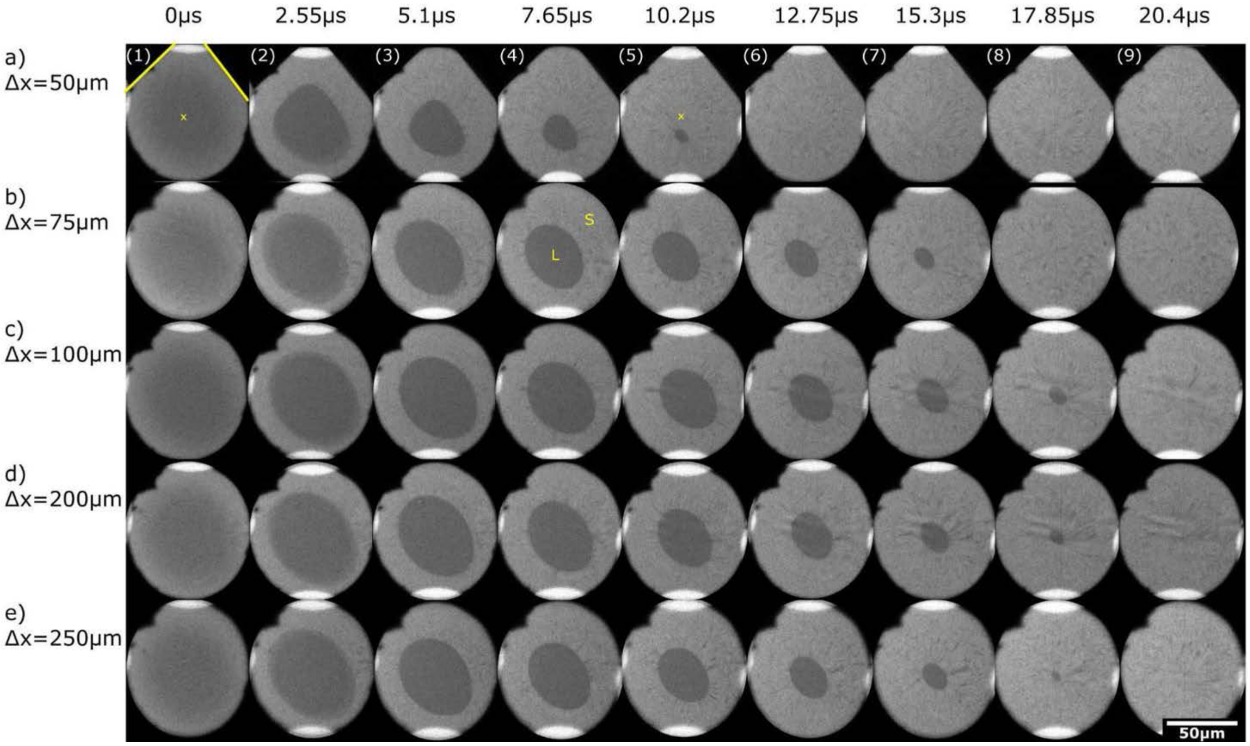

**Figure 23. In-situ DTEM Movie Mode bright field image series from locations (1) to (5) (Figure 20). (a) ΔX = 50 µm, (b) ΔX = 75 µm, (c) ΔX = 100 µm, (d) ΔX = 200 µm, and (e) ΔX = 250 µm. Each series contains nine individual frames marked (1) to (9). The labels L and S refer to all-liquid and all-solid regions. Adapted from** [97]**.**

Certain metric is needed in order to effectively evaluate the velocity evolution during rapid solidification and the melt pool size evolution with regard to time is an excellent metric for evaluating the velocity evolution during RS of pure Al. Since the distribution of laser pulse energy is elliptical and the melt pool consistently shows close to elliptical shape with planar interface at this given scale upon laser irradiation and also during the evolution, it is reasonable to approximate the melt pool as an ellipse. Based on the in situ observations, between $2.6\mu s < t_{image} < 5.15\ \mu s$, a discernible liquid-solid interface of the melt pool developed, which marks the initiation of solidification process after laser irradiation induced melting. The semi-major and semi-minor axes of the elliptical melt pool were measured by fitting an ellipse to the melt pool in the ImageJ software [102] for calculating velocity evolution. The average solidification velocity along the entire interface of the elliptical shape melt pools can be attained from the rate of change of the geometric-mean radius, R, which represents the radius of a circle of area equivalent to that measured for the corresponding elliptical melt pools observed experimentally. The area changes of the elliptical melt pools after in situ laser irradiation can then be represented by the changes of the respective geometric-mean radius, R, with time, and the instantaneous velocity evolution V(t) can then be expressed as following:

$$V\,(t) = -\frac{dR(t)}{dt}$$

### 5.3.2 Continuum modeling of rapid solidification in Aluminum thin films

As mentioned in section 4.5, the laser profile needs to be constrained to what was used experimentally to produce meaningful results and to allow direct comparison between the modeling results and the experimental results. The actual pico- to nanosecond timescale interactions between the sample drive laser photon pulse and the polycrystalline Al thin film is unclear. Also, the enthalpy deposited on the sample is significantly affected by the reflectivity of the sample materials, a parameter that cannot be accessed during in situ DTEM experimentation. As Hlaser is linearly proportional to (1 - reflectivity), i.e. changing reflectivity from 0.95 to 0.9 would increase the enthalpy deposited by 50% (see section 5.2.2), the energy of the laser is considered to be a highly unreliable metric or criterion for use in benchmarking the model against experimental data for setting up the laser parameters. Instead, the spatial laser profile geometry at the sample surface incidence, the initial dimensions of the resulting simulated melt pools when solidification initiates and the total time needed to complete solidification are well-defined experimentally accessible metrics and are used as the criterions for benchmarking of the laser parameters.

The actual laser profile reported by J. T. MeKeown *et al* is a laser with Gausssian beam profile ($1/e^2$ diameter of 135 ± 5 µm) incident at 45° [7]. For a Gaussian laser beam, the peak fluence can be related to total pulse energy by [99,103]:

$$E(r) = E_0 \exp(-\frac{2r^2}{w^2})$$

$$E_{pulse} = \int_{-\infty}^{+\infty} E(r) 2\pi r\, dr = \int_0^{\infty} E_0 \exp\left(-\frac{2r^2}{w^2}\right) 2\pi r dr = \frac{\pi w^2 E_0}{2}$$

where E(r) is the radial distribution of laser fluence, $E_0$ is the peak fluence and w is the $1/e^2$ intensity radius. The $1/e^2$ diameter is defined as the diameter of the Gaussian laser profile when $E(r) = E_0/e^2$.

In the enthalpy model implemented in COMSOL™ Multiphysics, a Gaussian function of two-dimensional form is used to represent the projected laser spot with incident angle of 45˚:

$$E(x, y) = E_0 \exp(-\frac{x^2}{2{\sigma_x}^2} - \frac{y^2}{2{\sigma_y}^2})$$

where $\sigma_x$ *and* $\sigma_y$ represent minor and major axis of the elliptical laser spot and correspond to the global parameters termed as *lasersigmax* and *lasersigmay* (see

Table 1 in section 5.2.2), respectively.

Along the minor axis: y = 0; E(x,0) = $\frac{1}{e^2}$ $E_0$ when x = $2\sigma_x$

Along the major axis: x = 0; E(0,y) = $\frac{1}{e^2}$ $E_0$ when y = $2\sigma_y$

By setting $\sigma_x$ = 34 µm, $\sigma_y$ = 34 µm / (cos 45˚) ≈ 47 µm, E(x, 0) = $\frac{1}{e^2}$ $E_0$ when x = $2\sigma_x$ = 68 µm and E(0, y) = $\frac{1}{e^2}$ $E_0$ when y = $2\sigma_y$ =94 µm. With these parameters, the Gaussian laser profile used in modeling would have $1/e^2$ diameter of ~136 µm and this agrees with the previously reported Gaussian laser profile used experimentally quite well (shown in Figure 24 and Figure 25).

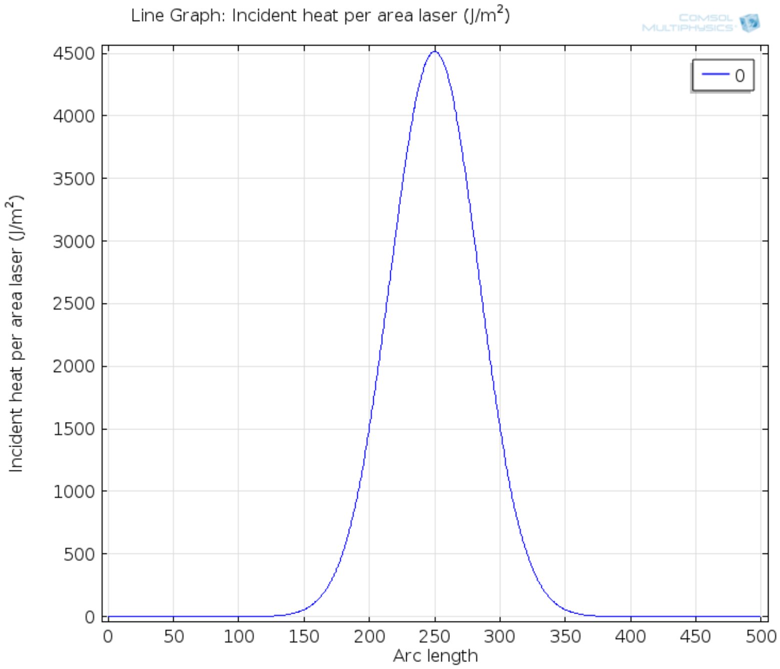

Figure 24. Laser Profile at time = 0 along the minor axis of the simulated melt pool

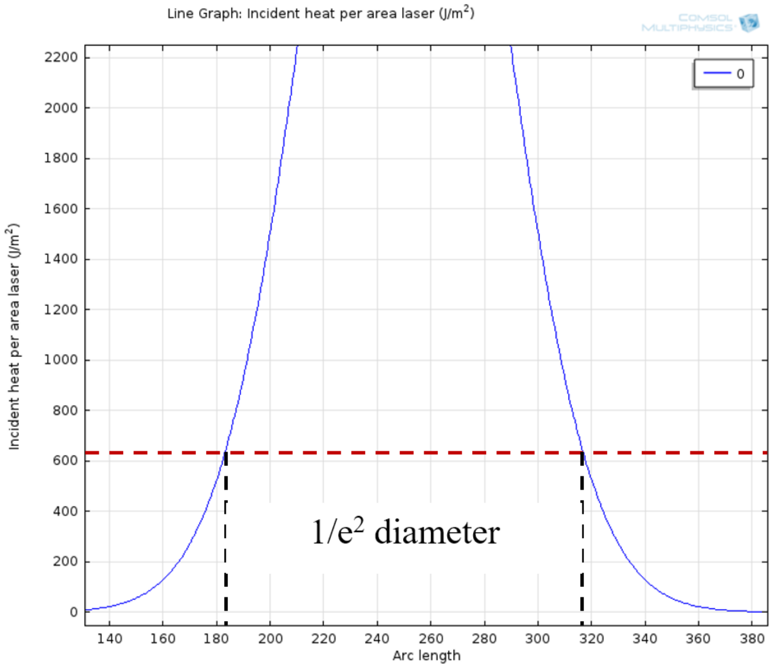

Figure 25. Zoomed-in view of laser profile along the minor axis of the simulated melt pool at time = 0, showing the $1/e^2$ diameter to be 136 µm

With the laser parameters defined, a series of simulation is performed to examine systematically the influence of numerical parameters and simulation parameters including but not limited to Hartificial, Dartificial, size and order of the mesh element. It has been observed that Hartificial and Dartificial need to be sufficiently small to avoid artifacts. If Hartificial or Dartificial are set to relatively large values, the “transition region”, effectively acting as the liquid-solid interface in the modeling, would not collapse to a very thin region and migrate together even at later time points during the simulation, as shown in Figure 26. In Figure 26, the color bar represents the temperature scale (red color indicates higher temperature) and the color in the simulation space indicates the calculated temperature field distribution corresponding to the color bar. The two black contour lines are the 933K, the melting point of Al, temperature lines (see section 5.2.2). The existence of transition region is for numerical continuity purposes and should have been a very thin region so that the solidification interface is properly represented. Clearly, a wide transition region is still present at 8 µs after laser irradiation in the simulation space as displayed in Figure 26. This is not physically accurate for representing the liquid-solid interface in the pure Al system.

In addition, finer mesh element size and higher element order were found to provide better numerical behavior and a smoother solidification interface. However, significantly more computation time (5 - 10 times more in some cases) was needed for modeling with finer mesh element size and higher element order. After a series of tests, it was determined the improvements were not sufficient to justify mesh element size of smaller than 0.15 µm and element order of higher than cubic. In order to balance the quality of the simulation results and the computation time, a mesh element size of 2 µm maximum and 0.15 µm minimum were used and a cubic element order was adopted for modeling the RS process.

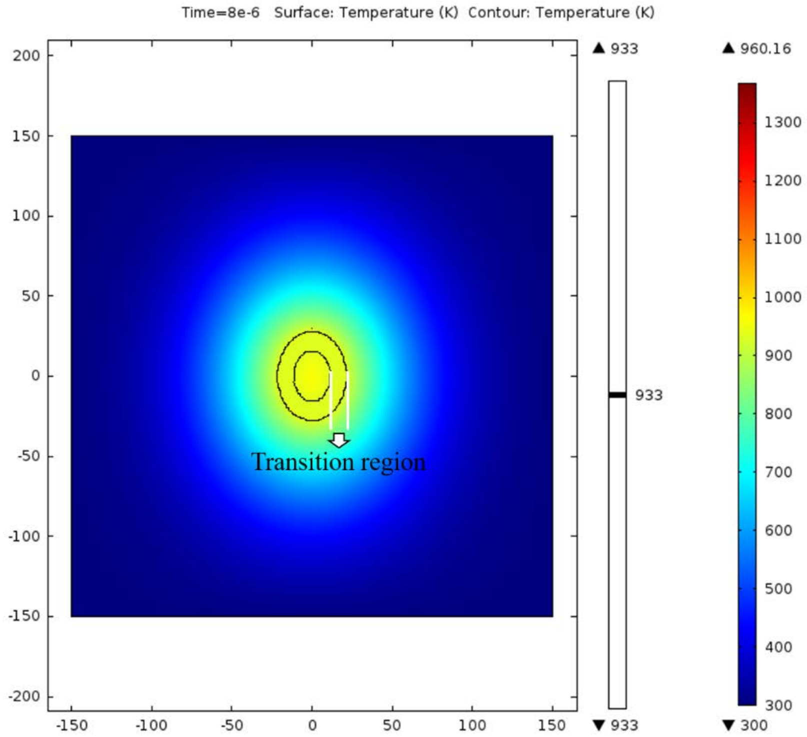

**Figure 26. Simulated melt pool at t = 8 µs after enthalpy deposition, showing wide "transition region" that is not collapsing as the "thin interface". Color bar represents temperature scale.**

After the laser parameters, numerical parameters and modeling parameters are set, the thermo-physical properties of Al and $Si_3N_4$ were systematically adjusted and optimized within the previously reported ranges of these values for the two substances [93–95,101]. Since the thermal conductivity of $Si_3N_4$ is at least an order of magnitude lower than that of Al, integrating the entirety of 50 nm thick of $Si_3N_4$ support layer into the composite material would require unrealistic thermal conductivity values set for Al to properly approximate the two-dimensional in-plane heat conduction assumption. Up to 15 nm of $Si_3N_4$ support layer could be incorporated without requiring unrealistic thermal conductivity values for Al, which implies at most a thin top layer of the entire $Si_3N_4$ support contributed to heat conduction. In addition, in reality there would be expected to be additional features associated with the interface between the dissimilar materials of the nitride membrane support and the metallic Al film, and the $Si_3N_4$ never actually undergoes melting and solidification like Al. Therefore, it is reasonable to exclude $Si_3N_4$ and the associated enthalpy required for $Si_3N_4$ melting in the melting of the composite material. The thickness of the $Si_3N_4$ support layer was set to 0 nm to exclude $Si_3N_4$ from the composite material. Iterations of benchmarking have been performed for the continuum modeling results by comparison with experimental data, which involved slightly varied material thermo-physical properties within the experimentally reported and therefore reasonable ranges. One set of parameters (tabulated in Table 7) was found to provide excellent matching between the model calculation results and experimental results in terms of the total time required for initiation and completion of the RS process, the initial maximum dimensions of the simulated melt pool and the simulated melt pool evolution over time. The size of the simulated melt pool starts to decrease monotonically after 3 - 3.5 µs, which marks the onset of solidification. This is in agreement with the in situ MM-DTEM observation that indicates the onset of solidification is between 2.6 µs and 5.15 µs. The simulated RS process completes around 18.3 µs after laser irradiation. Figure 27 a) and Figure 27 b) shows simulated melt pool at t = 3 µs and t = 18.2 µs and associated thermal field evolution. Note that only the central parts of the simulation space are shown in order to highlight the simulated melt pool.

**Table 7. Parameters used for modeling RS in pure Al**

| Properties | Value | Units |
|---|---|---|
| RMS width in x direction of elliptical laser spot | 34 | µm |
| RMS width in y direction of elliptical | 47 | µm |
| Assumed reflectivity of the solid Al | 0.95 | N/A |
| Assumed reflectivity of liquid Al | 0.9 | N/A |
| Thickness of $Si_3N_4$ layer | 0 | nm |
| Density of solid Al | 2640 | $Kg/m^3$ |
| Density of liquid Al | 2350 | $Kg/m^3$ |
| Density of $Si_3N_4$ | 3100 | $Kg/m^3$ |
| Heat capacity of solid Al | 1000 | J/kg/K |
| Heat capacity of liquid Al | 1095 | J/kg/K |
| Heat capacity of $Si_3N_4$ layer | 700 | J/kg/K |
| Thermal conductivity of solid Al | 210 | W/m/K |
| Thermal conductivity of liquid Al | 90 | W/m/K |
| Heat of fusion of Al | 398 | kJ/kg |
| Melting point of Al | 933 | K |

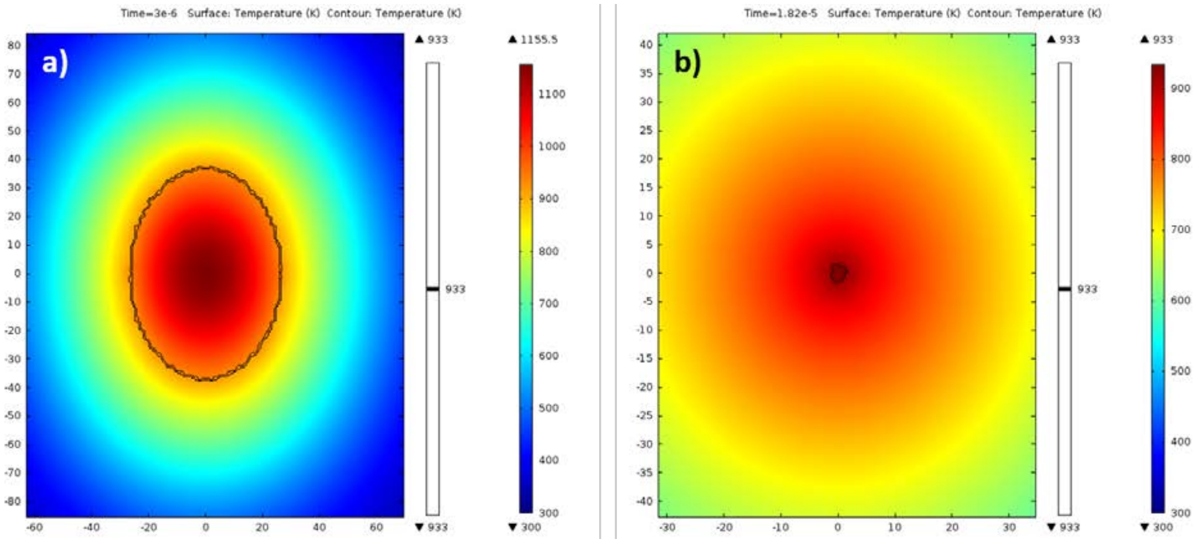

**Figure 27. Simulated melt pool by continuum modeling performed in COMSOL Multiphysics. Color bar represents temperature scale and contour lines represents interface of the melt pool. a) Melt pool at t = 3 μs and associated temeprature field around melt pool. b) Very small melt pool at t = 18.2 μs and associated temeprature field around melt pool, showing solidifiation is close to completion.**

With a satisfactory model benchmarked by the highly reproducible and thus high fidelity experimental results, it is then possible to extract the simulated melt pool at certain time points during the transformation sequence. This facilitates direct comparison the corresponding experimentally observed melt pool at the time points documented in the in situ DTEM image sequence (i.e., t = 2.55 μs, 5.1 μs, 7.65 μs, 10.2 μs, 12.75 μs, 15.3 μs and 17.85 μs) for comparison and validation purposes. Figure 28 shows the comparison between the MM-DTEM observation and the modeling results. The extracted model calculated images displayed at the same length scale as the experimental image sequence, i.e., the length per pixel is the same in both sequences. It can be seen that the simulated melt pool evolution agrees very well with experimental data obtained with the DTEM. Note that the “transition region” remains narrow during the simulated RS process.

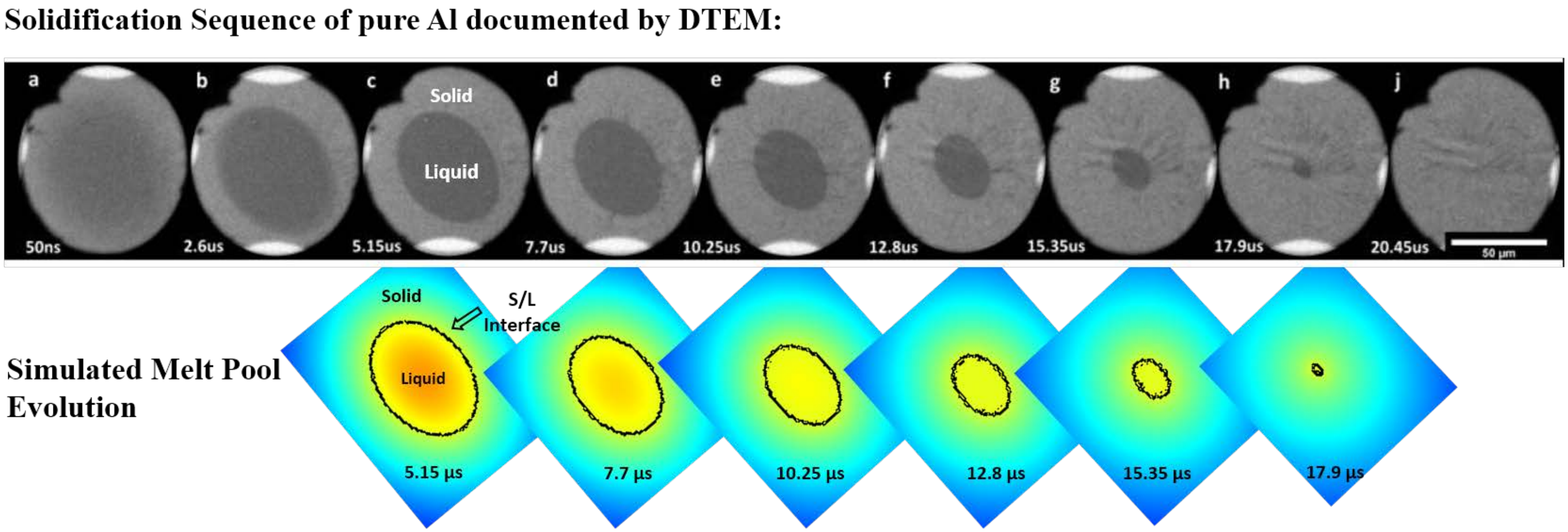

**Figure 28. Comparison between the MM-DTEM observations and simulated results. Top row: MM-DTEM sequence documenting RS process in Al thin film. Bottom row: Simulated melt pool evolution at corresponding time points. The black contour lines represent the melt pool interface.**

The calculations that matched the experimental benchmark metrics within the constraints imposed on the laser pulse and realistic material properties showed maximum temperatures at the center of the superheated liquid Al of 1365K and the Al melt cooled at rates on the order of $10^7$ K/s. Same as the MM-DTEM image sequence, the average solidification velocity averaged along the entire interface of the elliptical shape melt pools can be deduced from the rate of change of the geometric-mean radius, r. This represents the radius of a circle of equivalent area to that measured for the elliptical melt pools. The exact (x,y) positions of the melt pool interface in the simulation space can be exported, allowing facile and accurate determination of the length of the semi-major and semi-minor axes. Similar to the experimental measurements, the continuum results of the melt pool size evolution exhibited consistent deviations from linear behavior, e.g., overestimating the total time to complete solidification, which could be mediated by applying second-order polynomial best-fit procedures. Hence, the assumption of interface migration with a constant acceleration also provides better quantitative agreement with the continuum modeling–based calculations. The modeling results for the evolution of the melt pool size and velocity during RS of the 160nm thick Al thin film along with the evolution of the melt pool size and velocity determined from experimental data for comparison purposes are presented in Figure 29.

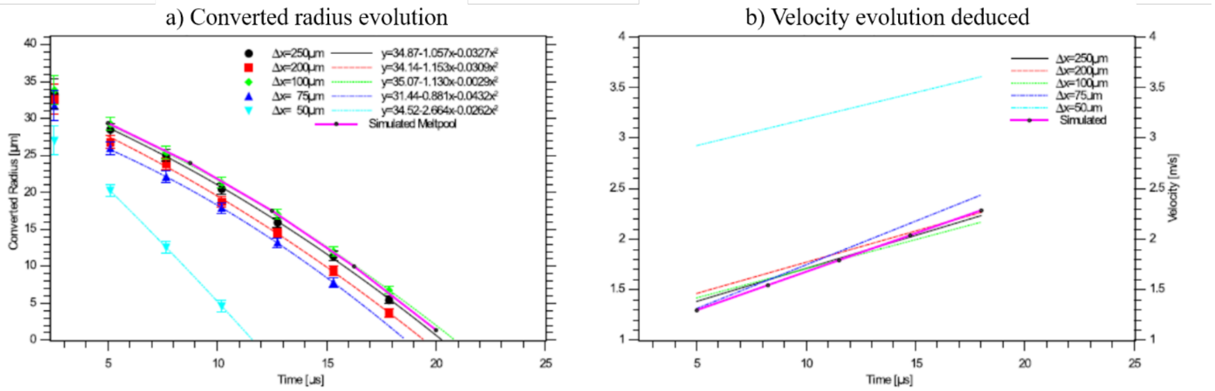

**Figure 29. a) Temporal evolution of the respective geometric radius for the experimental data sets for different ΔX and geometric radius obtained by continuum modeling calculation (labeled as "Simulated"); (b) associated solidification velocities deduced from the converted radius evolution. Adapted from** [97]**.**

The excellent agreements of the continuum modeling results with the experimental measurements demonstrate the unique capability of DTEM to provide experimental metrics suitable to benchmark and validate computational modeling results and thereby support the development of computational models for thin film specimen rapid solidification dynamics. Additionally, the comparison of experimentally measured and model calculated melt pool evolution supports the conclusion that to good approximation the solid-liquid interface velocity accelerates linearly during RS and the associated melt pool evolution is dominated by two – dimensional in-plane heat conduction from the superheated liquid Al radially outward into the surrounding solid Al. Since the thermal transport rate of the solid Al exceeds that of liquid Al significantly and the liquid Al is superheated, the heat of fusion generated at the evolving interface does not enter significantly into the liquid but rather ends up being transported away through the solid Al around the melt pool. Hence, the migration rate of the solid-liquid interface is limited by the two-dimensional heat conduction of the excess heat of fusion evolved at the interface and the thermal conductivity of the solid surrounding the melt. This is in analogous to pure metal growing into superheated liquid, during which the solidification remains planar and the heat flow away from the liquid-solid interface through the solid is balanced by heat flow from the liquid and the latent heat generated at the migrating interface[104], i.e.

$$K_S T_S = K_L T_L + vL_a$$

where K is the thermal conductivity, T is the temperature gradient, the subscripts S and L indicates corresponding properties for solid and liquid, respectively, v is the interface velocity, and $L_a$ is the latent heat of fusion per area. The interface velocity, v, can then be deduced as:

$$v = \frac{K_s T_s - K_L T_L}{L_a}$$

In this model, $K_S$, $K_L$ and La are constant. Based on the modeling results, it appears that the latent heat of fusion can always be conducted away sufficiently fast without heating up the surrounding liquid significantly while the temperature of the superheated liquid decreases rapidly, which means change of $T_S$ is small but $T_L$ decreases rapidly during solidification process (illustrated in Figure 30). As a result, $K_S T_S$ remains more or less the same while $K_L T_L$ decreases throughout the RS process, and hence the interface velocity, v, increases. Physically, as solidification progresses, the melt pool shrinks and less and less heat of fusion is generated at the interface. Therefore, less and less time is required to establish thermal equilibrium through heat conduction, resulting in the acceleration of the interface migration. The value of acceleration is material property dependent and hence remains constant during the RS process of Al since the thermo-physical properties of Al do not change significantly during the RS process.

Upon examining the calculated temperature field evolution at several time points during the RS process, it can be noticed that the temperature at locations that are 100 µm away in the Al thin film from the center of melt pool increased only ~ 100 K and the temperature increase at locations that are 150 µm away in the Al thin film from the center of melt pool is negligible (shown in Figure 30). This is consistent with the “safe zone” determined by systematical in situ DTEM investigation. This demonstrates that, using pure Al as the model system, the modeling results could guide DTEM experimentation for material systems with different thermo-physical properties. It is possible that the “safe zone” tests are not necessary for other material system by inputting corresponding thermo-physical properties into the enthalpy model to examine the calculated temperature field evolution and hence deduce the safe distance.

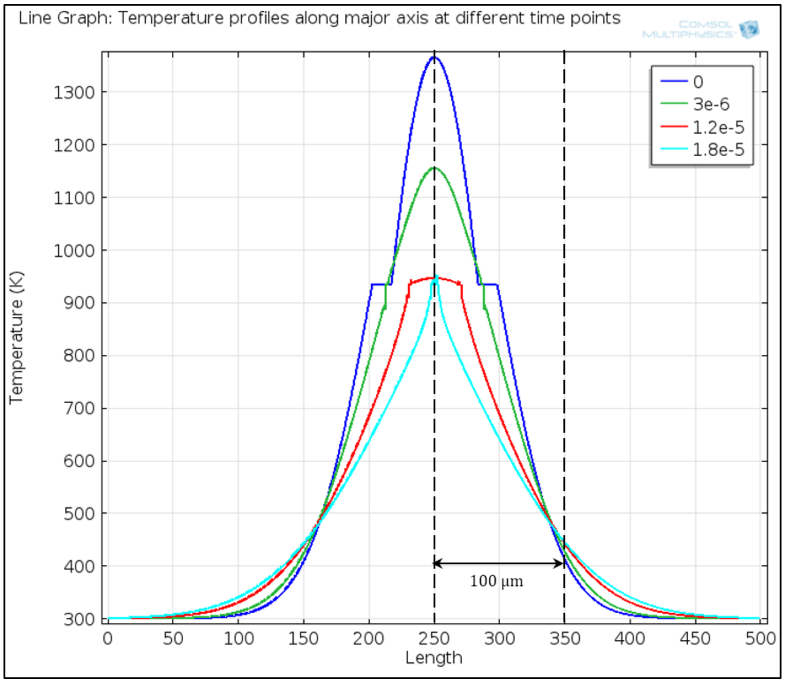

**Figure 30. Simulated temperature profile along major axis of melt pool at t = 0 μs, 3 μs, 12 μs and 18 μs. The center of the melt pool is at X = 250 μm.**

In addition, combining with post-mortem characterization, the modeling results can potentially shed light on the interpretation of the rapidly solidified microstructure. For example, the rapidly solidified microstructure in Al thin film has been extensively investigated by K. Zweiacker [28] and it was found that there is significant grain growth in a region that is within ~ 40 μm from the perimeter of the melt pool that cannot be explained by conventional heat affected zone and thin film grain growth theories. The BF TEM micrograph and grain size statistics on the right side of  Figure 31 shows the average grain size of grains that are adjacent to the melt pool is ~ 600 nm and remains roughly the same for about 20 μm distance. Then the average grain size gradually decreases from ~ 600 nm to ~ 475 nm in the region that is between 20 μm and 40 μm away from the melt pool. However, instead of continuing the gradual decreasing trend, the average grain size drastically drops to an average grain size of ~ 350 nm and start to gradually decrease again to an average grain size of ~ 160 nm, the original average grain size of the as-deposited Al film. In short, the average grain size remains the same for certain distance and then gradually decreases and then drastically decreases, deviating from the normal gradual change behavior.

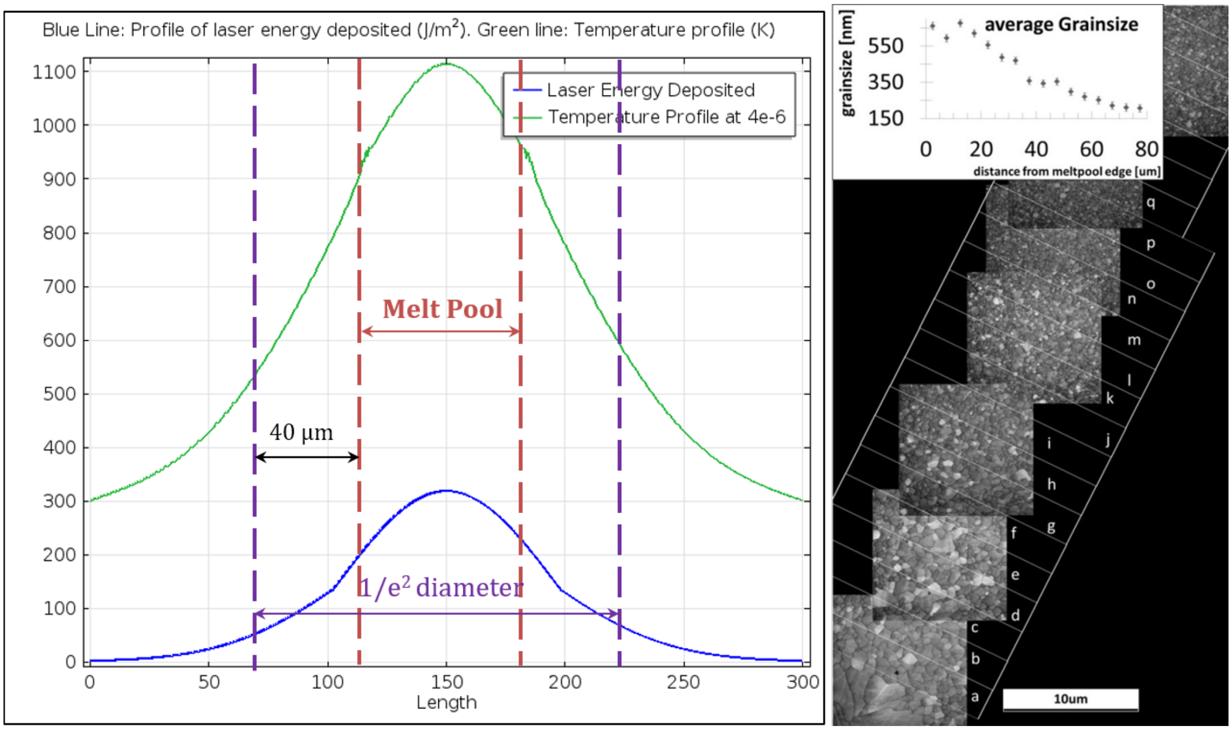

**Figure 31. Left: Overlay of laser energy deposited initially and temperature profile across melt pool at t = 4 μs, showing the geometric relationship between the laser induced melt pool and the laser profile. Right: TEM micrograph and accompanying average grain size statistics showing the gradual change of average grain sizes in regions adjacent to melt pool until 40 μm away from the melt pool and the drastic drop at x = 40 μm.**

It is hypothesized here that these microstructural characteristics are related to preferential melting of the polycrystalline thin film Al along the grain boundaries. Since the laser profile is a two-dimensional Gaussian distribution, it is possible that the energy of part of the laser pulse was not sufficient to introduce complete melting of the Al thin film but was high enough to induce grain boundary melting because grain boundaries often exhibit lower melting point than the matrix [105–107]. As the grain boundary melts, the grains are free to grow laterally into the liquid area that was previously grain boundaries. Since the laser energy gradually decreases with increasing distance from the melt pool, gradually decreasing level of grain boundary melting could be achieved. Depending on the extent of grain boundary melting, different extent of lateral grain growth could occur based on the distance from the melt pool, which explains the change of average grain sizes adjacent to the melt pool until 40µm away from the melt pool. However, once the laser energy is lower than a certain threshold to initiate grain boundary melting, the average grain size in those regions would show a discontinuous drop, like what we have observed in the pure Al thin film, because the grain boundary melting is no longer present and hence lateral growth is not possible, allowing conventional grain growth mechanism in heat affected zones would take over. By comparing the laser energy profile and the temperature profile shown in the right side of Figure 31 it can be seen that the thin film locations that are close to the melt pool experienced substantial heating due to the Gaussian laser profile but the temperature rapidly decrease with increasing x distance because the surrounding solid can rapidly transport heat away. Based on the overlay of the laser profile and the temperature profile at 4 µs after laser irradiation, the locations that are 40 µm away from the melt pool corresponds to the $1/e^2$ diameter of the laser profile. Thus, the modeling results partially supports the hypothesis for explaining the change of average grain sizes in the regions around the laser induced melt pool. It is still an ongoing effort to correlate the modeling results with the rapidly solidified microstructures.

## 5.4 SUMMARY

In summary, using pure Al as a model system, the framework and methodology of in situ MM-DTEM experimentation have been established and rapid solidification in pure Al have been successfully investigated by in situ MM-DTEM experiments. Continuum modeling benchmarked by in situ MM – DTEM based observations and analysis supplemented the experimental results and provided potential insight for quantitative understanding of the rapid solidification process in Al.

In situ dynamic transmission electron microscopy studies of rapid solidification in Al thin film evaporated on windowed membrane TEM grids revealed changes in crystal growth rates due to effects from differences in the heat extraction geometry. Based on the quantification of the reproducible dynamic behavior of rapid solidification at certain locations within the window area, it can be concluded it is necessary to control the position of the laser pulse on the TEM grid, thus ensuring that the heat extraction remains the same for the subsequent solidification event during multiple experiments, for obtaining reproducible experimental results.

The in situ TEM observations supports the solidification interface was migrating at a constant acceleration and confirmed a range of solidification front velocities for different interface segments along the perimeter of the elliptical melt pool, with a maximum and minimum velocity along, respectively, the major and minor axes of the melt pool. This is a consequence of heat extraction due to variations in the local curvature of the solid-liquid interface.

Continuum modeling based on an enthalpy model was performed in the COMSOL® Multiphysics environment and validated by experimental metrics to determine the thermal evolution during the rapid solidification of pure Al thin film. The modeling results showed that, in excellent agreement with the experimental measurements, the solid-liquid interface accelerated during the rapid solidification process. Melt pool evolution was dominated by two-dimensional heat conduction from the superheated liquid Al and the solid-liquid interface radially outward into the surrounding solid Al, indicating that the migration rate of the solid-liquid interface was limited by the thermal-physical properties of the surrounding solid.

Combined with computational results and post-mortem analysis, time-resolved in situ DTEM characterization facilitates quantitative understanding of pulsed laser induced melting and subsequent rapid liquid-solid transformation in pure Al, demonstrating the unique capability of DTEM to provide direct observation with nano-scale spatio-temporal resolution and validation of computation modeling.

# 6.0 RAPID SOLIDIFICATION OF HYPO-EUTECTIC ALUMINUM - COPPER ALLOY THIN FILMS

With the methodology for consistent MM-DTEM experimentation established using pure Al, rapid solidification processes in hypo-eutectic Al – Cu alloy thin films with Cu concentrations higher than four atomic percent are investigated.

This chapter presents and discusses results based on low-magnification MM-DTEM image sequences as well as MM-DTEM image sequences with high spatial-temporal resolution for accurate determination of velocity evolution during rapid solidification process in hypo-eutectic Al – 11 at.% Cu alloy thin films (for brevity Al-11Cu from hereon). In addition, ex situ pulsed laser irradiation experiments have been performed on the Al-11Cu. Post mortem characterization of the solidification microstructure obtained for the in situ and ex situ pulsed laser irradiation using conventional transmission electron microscopy (TEM), scanning TEM (STEM) and TEM PED based OIM and compositional mapping by energy dispersive X-ray spectroscopy (EDS) have been performed to correlate the solidification conditions and resultant rapidly solidified microstructure.

Results of the current study of the microstructure evolution during rapid solidification of Al-11Cu are compared with prediction from previously published solidification microstructure selection maps (SMSM) for the Al-Cu system [35]. By comparison with prior experiments on the hypo-eutectic Al-4Cu the effects of increased Cu content and crystallography on the rapid solidification behavior of hypo-eutectic Al – Cu alloy thin films are examined and quantified.

## 6.1 AS-DEPOSITED HYPO-EUTECTIC ALUMINUM-COPPER THIN FILMS

Establishing the link between the rapid solidification conditions and resultant microstructures requires documentation of the initial microstructures before rapid solidification in order to establish the change in microstructural characteristics accompanying the rapid liquid-solidi phase transformation. Important aspects of the as-deposited Al-11Cu thin film microstructure, such as film morphology, grain size, phases present and potential texture need to be characterized as the starting condition for subsequence RS processes.

Figure 32 (a) displays an example BF TEM image of the as-deposited hypo-eutectic Al-11Cu alloy thin film before laser irradiation, showing that the initial state of the film is continuous with grains of nanocrystalline features. Figure 32 (b) is a representative, typical selected-area electron diffraction pattern (SADP) obtained for the initial film. The discontinuous ring-type diffraction pattern is consistent with the nanocrystalline nature of the thin film. According to the Al-Cu phase diagram, the equilibrium phases that should be present are α-Al and θ-$Al_2Cu$. In the example SADP in

Figure 32 (b), although not all the diffraction rings are labeled, all diffraction peaks can be indexed as either α-Al or θ-$Al_2Cu$ phases. Since the lattice parameter of θ-$Al_2Cu$ (I4/mcm, a = 0.6066 nm, c = 0.4874 nm) is larger than that of α-Al (Fm$\bar{3}$m, a = 0.4046 nm) [108], the diffraction rings corresponding to the θ-$Al_2Cu$ phases appear closer to the center beam in the SADP. The diffraction data reveals that the film consisted of the equilibrium α-Al and θ-$Al_2Cu$ phases. Figure 32 (c) presents a typical and representative Dark Field (DF) TEM image of the hypo-eutectic Al-Cu thin film confirming that the film is comprised of nanocrsystalline grains. Upon counting ~ 100 the strongly diffracting grains in a series of DF TEM images, the average grain size was determined to be ~ 30 nm.

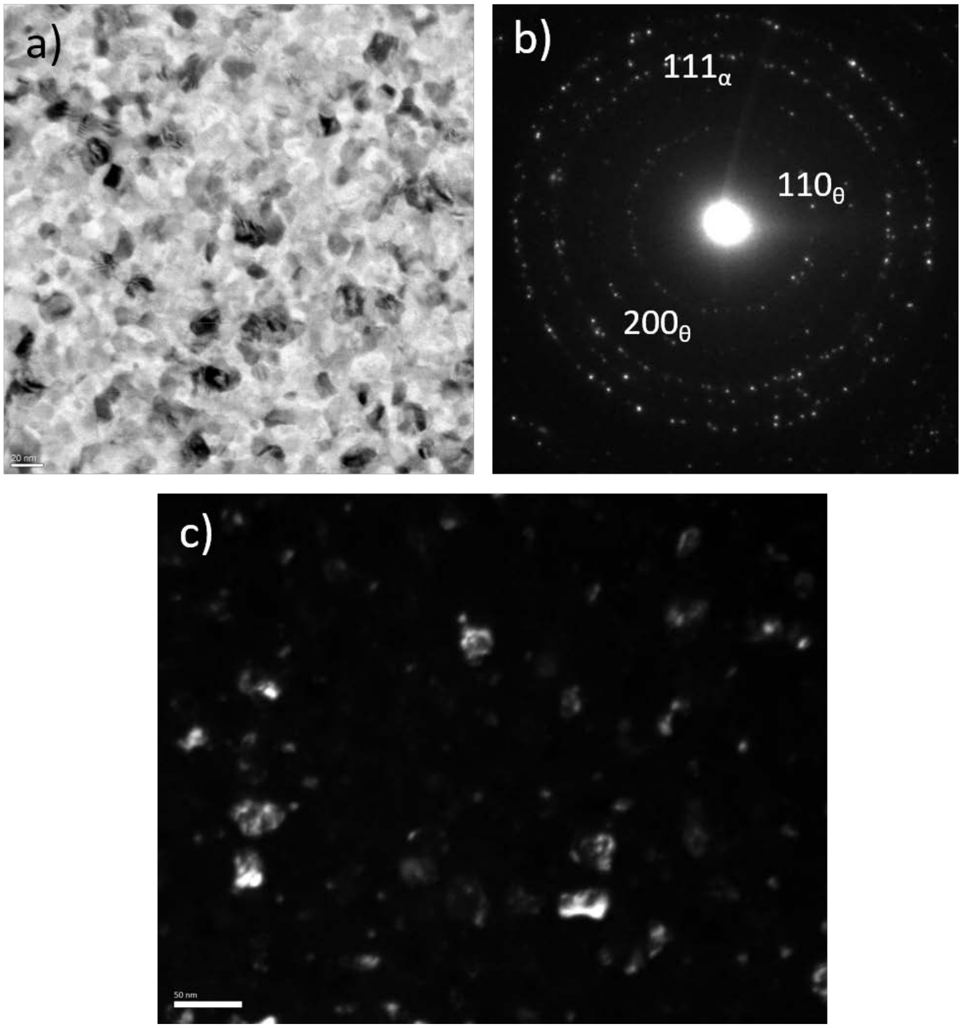

**Figure 32. a) BF TEM image of the as-deposited hypo-eutectic Al-Cu thin film. b) Example SADP of the as-deposited hypo-eutectic Al-Cu thin film and c) Typical DF TEM image of the hypo-eutectic Al-Cu thin film showing the nanocrystalline grain size.**

High-angle annular dark field (HAADF) based scanning transmission electron microscopy (STEM) imaging combined with EDS measurements and mapping have also been performed for compositional analysis of the as-deposited hypo-eutectic Al-Cu alloy thin film and an example of the results is shown in Figure 33. In HAADF STEM based imaging, the contrast is strongly dependent on the atomic number of elements present and heavier element with higher atomic numbers exhibit strong intensity in the HAADF images, known as the Z-contrast [109]. Therefore, the features with brighter contrast in Figure 33 a) should correspond to regions Cu-enriched relative to the alloy composition and the areas that appear to be darker in contrast, which should correspond to regions Cu-depleted relative to the average alloy composition. Figure 33 b) presents a color coded Cu concentration map based on STEM EDS mapping of area shown in Figure 33 a), with redder color representing higher concentration level of Cu and the contrast correlation between the relatively Cu-rich areas and Cu-depleted areas in Figure 33 a) and b) is evident. Quantitative STEM EDS measurements of specific areas and also the average composition of the thin film have been conducted and the locations of some example regions used for measurements are indicated in Figure 33 a) using red rectangle (#1, view) and red circles (#2 - #7). The measured compositions in terms of atomic percent of Cu are tabulated in Table 8. It can be seen that the average composition of the Cu-rich phases is Al – 31.65 at.% Cu and Cu-depleted areas is Al – 2.2 at.% Cu, which correspond to the composition ranges that are consistent with the θ-$Al_2Cu$ and α-Al phases. The latter appears to be a super-saturated Al solid solution phase, since at room temperature the solubility of Cu in Al is well below 1 at%, while the former essentially agrees with the equilibrium composition expected for $Al_2Cu$ within the error margin of EDS measurements. By averaging EDS measurements from several large area scans, the composition of the hypo-eutectic as-deposited film is determined to be Al – 11Cu.

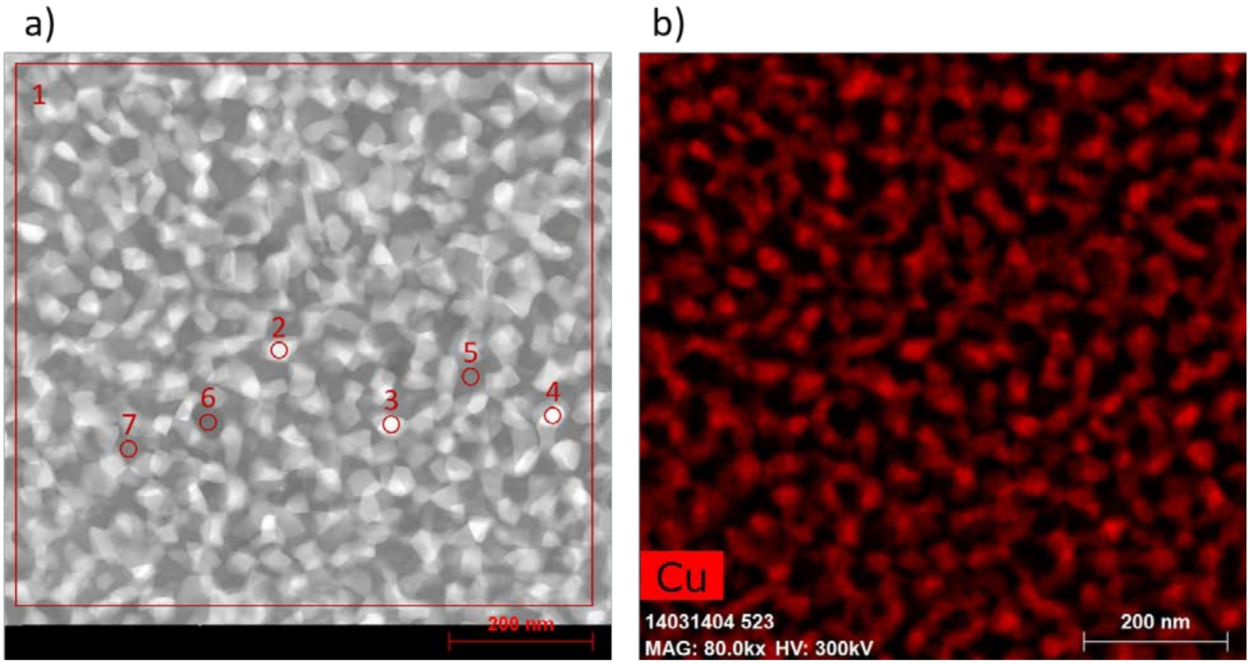

**Figure 33. a) HAADF image of the as-deposited hypo-eutectic Al-Cu thin film with red rectangle and circles indicating location for EDS measurements. b) color coded EDS mapping of Cu concentration.**

**Table 8. Atomic percent of Cu in EDS measurements shown in Figure 33 a)**

| Location | at.% Cu |
|---|---|
| **1 (view)** | 11.7 |
| **2** | 32.45 |
| **3** | 30.13 |
| **4** | 32.37 |
| **5** | 2.42 |
| **6** | 1.61 |
| **7** | 2.71 |

In order to effectively resolve the crystallographic information of the nanocrystalline grains in the as-deposited Al – Cu thin films, TEM PED based OIM scans have been utilized and representative Inverse Pole Figure based orientation maps (IPF map) extracted from such scans along with the standard triangle for IPF map color coding are shown in Figure 34. Figure 34 a) shows the grain orientation map viewed from a direction parallel to the incident beam direction (i.e. film normal) and there is a clear dominance of green colored grains, indicating a preferred orientation of {110} along the film normal. Figure 34 c) presents the complementary IPF map of grain orientation direction in the film plane (i.e., here the horizontal x direction). No preference or dominance of a specific color-coding can be observed, indicating a close to random distribution of grain orientations in the film plane. The associate pole figures in Figure 34 b) summarize the preference for <011> foil normal and lack of crystallographic orientation preference, texture, for the in-plane directions of the grains in the Al-11Cu thin films. These features are equivalent to those reported for the Al-4Cu films [28].

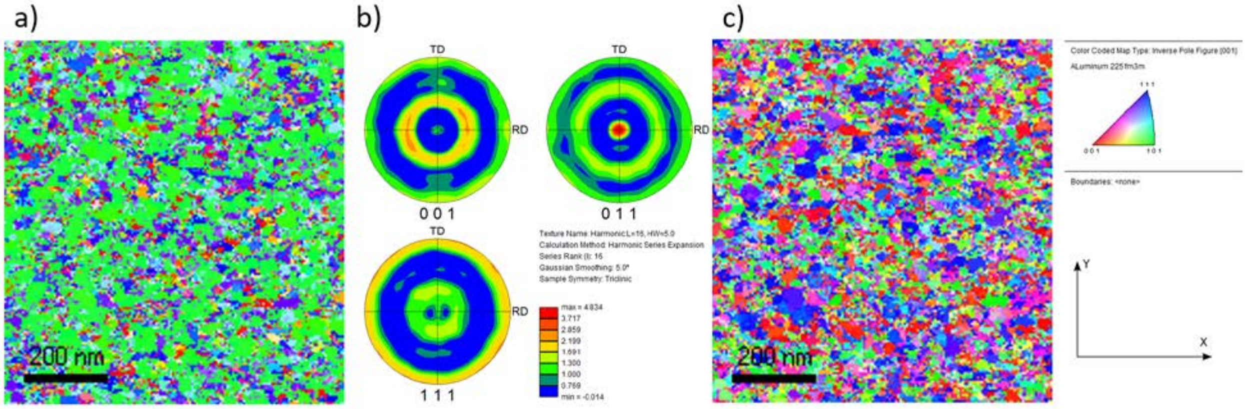

**Figure 34. IPF based color coded maps showing orientation of grains in as-deposited Al-Cu thin film. a) IPF map with view axis parallel to the film normal, showing preferred orientation of {110}. b) Pole figures associated generated from IPF map shown in a0, confirming the {110} type texture. c) IPF map with view axis parallel to the in-plane direction (horizontal x direction in images)**

In summary, the as-deposited hypo-eutectic Al – Cu thin films are continuous polycrystalline films with nanocrystalline grains of average grain size ~30 nm. Compositional analysis showed the as-deposited films are consisted of equilibrium α-Al phase and θ-$Al_2Cu$ phase and the average composition of the films is Al – 11Cu. TEM PED based OIM scans reveal a preferred grain orientation of <110> along the film normal but the in-plane distribution of grain orientations is close to random.

## 6.2 RAPID SOLIDIFICATION IN HYPO-EUTECTIC ALUMINUM-COPPER THIN FILMS BY IN SITU PULSED LASER IRRADIATION

### 6.2.1 In situ MM-DTEM experimentation and crystal growth velocity determination

With experimental methods established using pure Al thin films for observing rapid solidification process in thin film geometry by MM-DTEM, time-resolved MM-DTEM in situ experiments have been performed in the Al-11Cu thin films to record in situ the pulsed laser irradiation induced rapid solidification process in high Cu content hypo-eutectic Al – Cu alloys. A set of four MM-DTEM image sequences for four separate laser melting induced rapid solidification transformations obtained with different time-delays after the initial laser pulse are compiled in Figure 35.

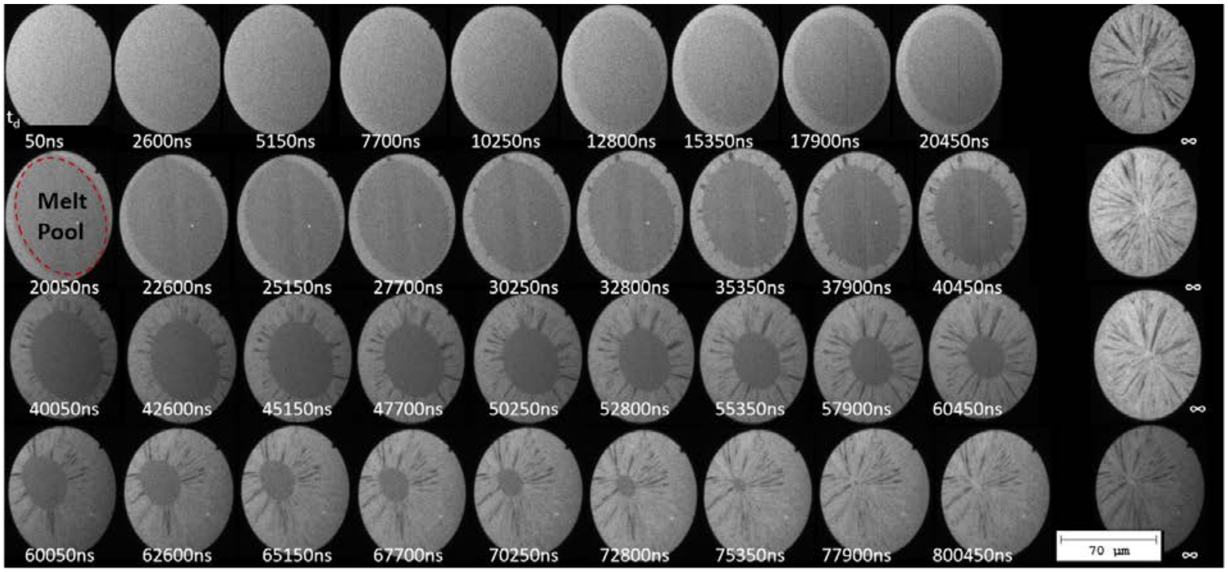

**Figure 35. MM-DTEM image sequences of images recorded during rapid solidification in Al – 11at.% Cu alloy thin film after pulsed-laser irradiation. The indicated times below each image are the time intervals between the peak of the Gaussian laser pulse and the 50 ns duration image formation electron pulse.**

Four low magnification DTEM sequences with 9 frames per sequence of 2.5 µs inter-frame time and 50 ns image formation electron pulse at different time delays were taken to cover the entire melting and re-solidification process of Al – 11Cu alloy thin films. The sequences are arranged in chronological order and presented in Figure 35. Each one of the four rows of image sequence correspond to one time-delay sequence of images recorded during rapid solidification of Al – 11Cu from a separate solidification experiment performed with initial delay times of 0, 20, 40 or 60 µs, respectively, as indicated under the first image of each row. The nanocrystalline grain structure was not resolved at the magnification used to obtain the time-resolved images in Figure 35 but the entire melt pool is clearly identifiable. The melt pool, as illustrated by the area circled with dashed line in the first image of second row of image sequence in Figure 35 (20.05 µs image), is the darker featureless region with fairly uniform contrast in each image. The diffraction contrast from newly formed solid in the MM-DTEM images distinguished the solid formed and the liquid melt pool. Therefore, the solid-liquid interface is evident in the images of Figure 35, allowing for tracking the evolution of melt pool during the transformation.

Similar to the case of pure Al, the solidification front velocity can be determined by tracking and measuring the dimensional evolution of the melt pool recorded in the MM-DTEM image sequences. The semi-major and semi-minor axes of the elliptical melt pool were measured by fitting an ellipse to the melt pool in the ImageJ software [102] for calculating velocity evolution. Starting from 12.8 µs, the solid-liquid interface becomes distinguishable and the last remaining liquid is barely discernible at 77.9 µs. Therefore, melt pool size measurements were performed on the MM-DTEM image frames obtained between 12.8 µs to 77.9 µs.

Normally, the melt pool at the starting time of one sequence has been observed to be smaller than the size of melt pool recorded at the end time of the previous sequence, even though they should have been of very similar size because they are only 0.4 µs apart from each other. It is speculated that the electron pulse used for in situ imaging would interact with the liquid and growing solid, introducing slight heating up of the thin film, and hence slow down the interface propagation. This beam effect would be minimal for the first frame of a given sequence and most significant for the last frame of a given sequence. As a result, the melt pool at the starting time of one sequence has been observed to be smaller than the melt pool recorded at the end time of the previous sequence. For example, the area of melt pool in the first frame at 40.05 µs of sequence #3 (40.05 µs to 60.45 µs) is 15% smaller than the area of melt pool in the last frame at 40.45 µs of sequence #2 (20.05 µs to 40.45 µs). Using the converted radius method to calculate velocity evolution is advantageous because it would, for instance, reduce the difference to 6% in this case.

However, when comparing the melt pool documented at 60.05 µs in sequence #4 to the melt pool recorded at 60.45 µs in sequence #3, the measured size of melt pool at 60.45 µs is larger than the measured size of the melt pool at 60.05 µs. Moreover, the melt pool at 20.05 µs (first frame in sequence #2, 20.05 µs to 40.45 µs) is noticeably larger than the size of the melt pool at 12.8 us displayed in the first sequence (sixth frame in sequence #1, 0.05 µs to 20.45 µs), which was considered to be the first identifiable frame for velocity calculation initially. This seemingly contradicting behavior can be attributed to the fluctuation in the energy of sample drive laser when triggering the rapid solidification event in Al-Cu alloy thin films. Laser irradiation on samples with higher energy will induce a larger melt pool to start with. As a result, the melt pools documented in a sequence with longer time delays could appear to be even larger than the melt pools captured in a sequence with shorter time delays. For experimental verification purpose, it would be ideal if a zero time-delay image of the initial melt pool can always be obtained for every sequence taken, which requires a laser system allowing for different inter-frame time within one sequence that current DTEM does not have access to. Since the difference between the 20.05 µs melt pool and 20.45 µs melt pool is significant while the difference between the 60.05 µs melt pool and 60.45 µs melt pool is within reason, the suitable time frame used for velocity evolution calculation is then determined to be from 20.05 µs to 77.9 µs.

At the magnification of the MM-DTEM observations presented in Figure 35, the solid-liquid interface of the melt pool in Al – 11Cu appears morphologically planar, with no sign of dendritic growth during rapid solidification. The melt pool dimensions monotonically decrease at times of 25.15 µs and longer after the delivery of sample drive laser irradiation pulse. Therefore, it can be concluded that the rapid solidification commenced between 22.6 and 25.15 µs, evidenced by the columnar grains that propagate radially inward, and completed slightly later than 77.9 µs (Figure 35). The initial dimensions of the melt pool at the discernible onset of rapid solidification have been determined with radii of ~ 42 µm and 32 µm along the semi-major and semi-minor axes, respectively (Figure 35). The time evolution of the associated area of the shrinking melt pool from 20.05 µs to 77.9 µs during rapid solidification is shown in Figure 36.

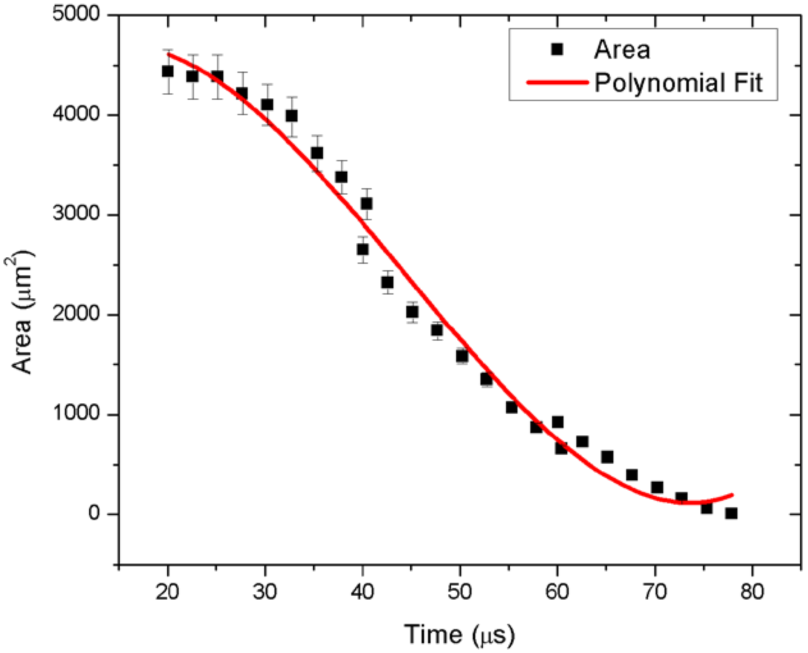

**Figure 36. Time evolution of the melt pool area in Al - 11 at.% Cu**

In order to deduce the velocity evolution during the rapid solidification process of Al – 11Cu, the converted radius method has been applied. This method uses the change of the geometric mean radius for the semi-major and semi-minor axes of the elliptical melt pool, the converted radius, $r_C$, to represent the overall temporal evolution of the mean melt pool size. This is the same procedure used in the case of pure Al (see section 5.3) and in prior published reports on MM-DTEM studies of other composition hypo-eutectic Al-Cu alloys [97,110]. However, since the entire solidification process of Al – 11Cu alloy lasts four times longer when compared to the process of pure Al, the converted radius, $r_{c,}$ for the three different MM-DTEM sequences between 25.15 µs and

77.9 µs (see Figure 35) are tabulated and then fitted with second or third order polynomial function separately in Figure 37Figure 38 and Figure 39.

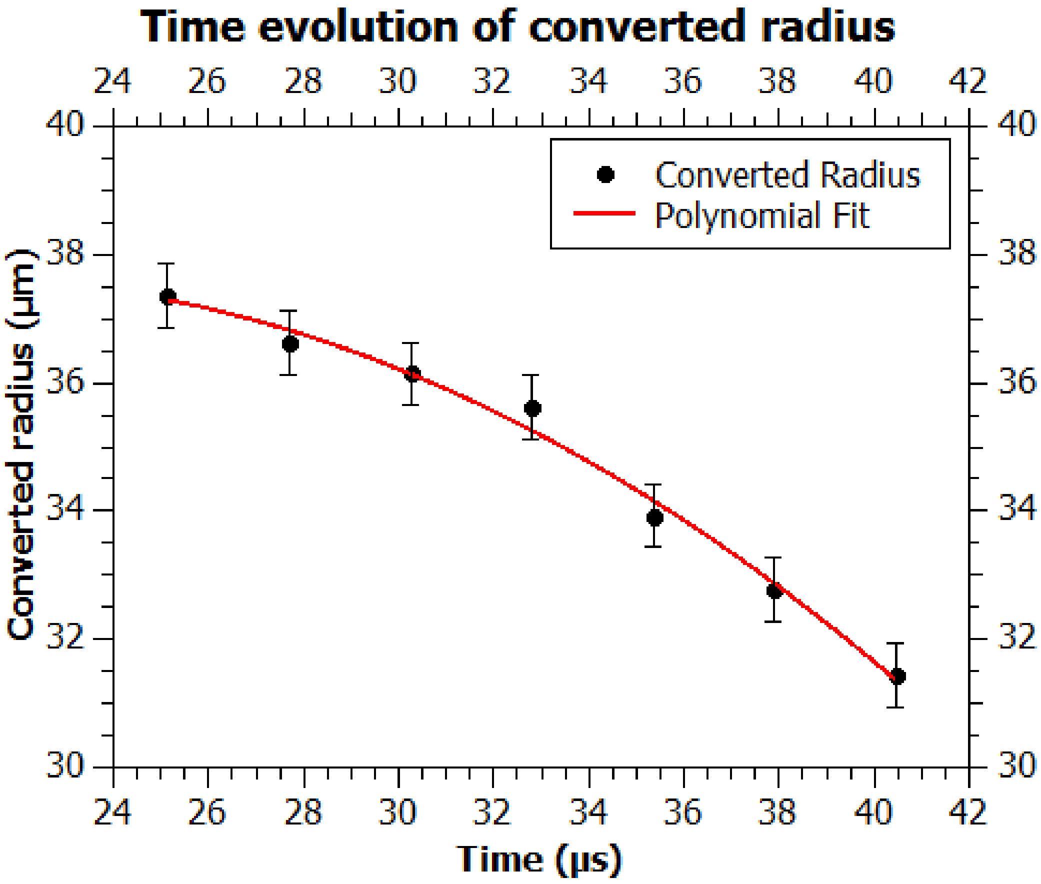

Figure 37. Time evolution of the converted radius between 25.15 µs and 40.45 µs (sequence #1)

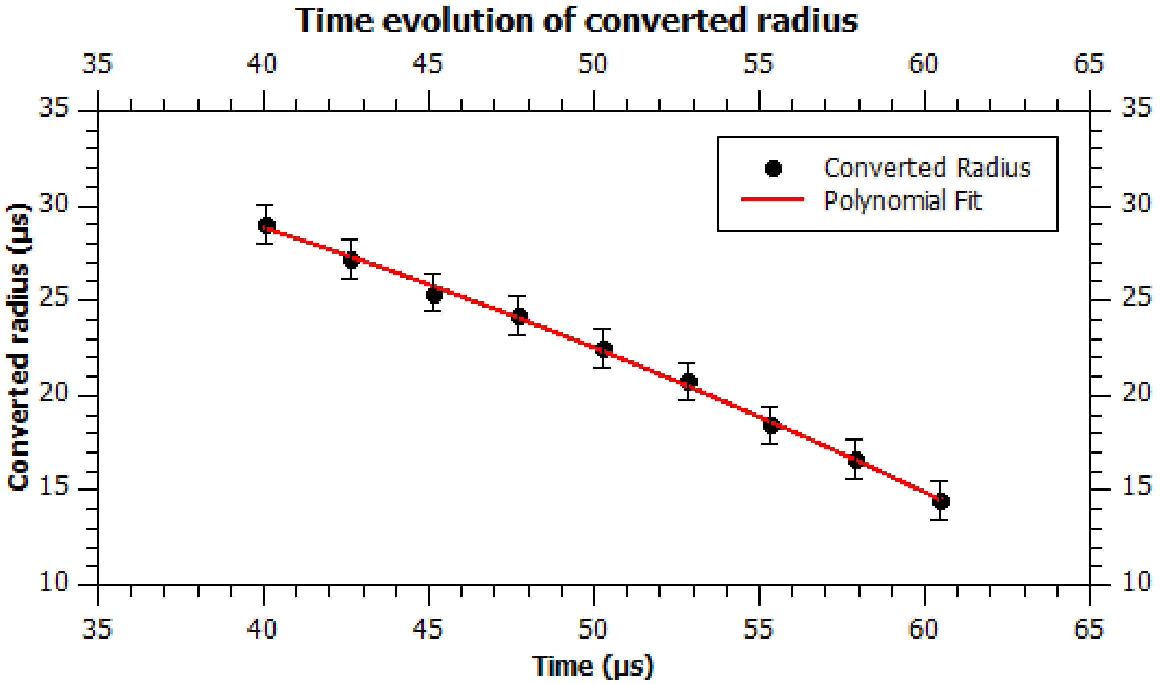

Figure 38. Time evolution of the converted radius between 40.05 µs and 60.45 µs (sequence #2)

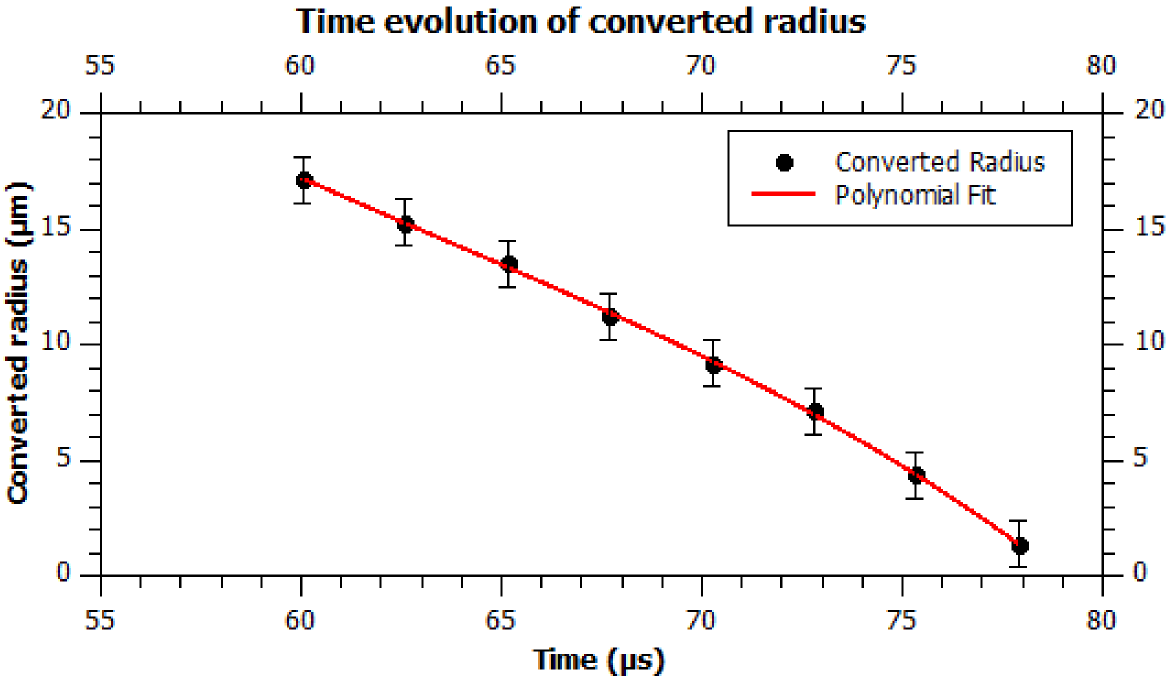

Figure 39. Time evolution of the converted radius between 60.05 µs and 77.9 µs (sequence #3)

The converted radius, $r_{c,}$ evolutions displayed in Figure 37, Figure 38 and Figure 39 correspond to the measurements from three different MM-DTEM time-resolved sequences, namely, sequence#1 (25.15 µs to 40.45 µs), sequence#2 (40.05 µs to 60.45 µs) and sequence#3 (60.05 µs to 77.9 µs), respectively, shown in Figure 35. The polynomial fitting used for sequence#1 and sequence#2 is a second-order polynomial fitting, corresponding to a constant acceleration of the solidification interface during the given time interval from 25.15 µs to 40.45 µs and from 40.05 µs to 60.45 µs, respectively. Third-order polynomial fitting provided the best fit for the evolution of converted radius for sequence#3, which corresponds to an increasing acceleration during the later stage of the rapid solidification process in Al – 11Cu. This fundamentally different behavior during the later stages of rapid solidification (sequence#3) with respect to the earlier constant acceleration of the earlier stages of rapid solidification will become clearer with the subsequently performed velocity evolution analysis.

The polynomial expressions for the time evolution of the converted radius were then differentiated with respect to time to obtain analytical expressions for the velocity evolution with time. In order to increase the data density during the span of the entire solidification process, the converted radius values with very small time intervals were extracted from the fitted functions of each of the MM-DTEM time-resolved image sequences presented above (Figures Figure 35Figure 37Figure 38 and Figure 39) for describing the overall velocity evolution compactly and the resultant solidification front velocity evolution is plotted in Figure 40.

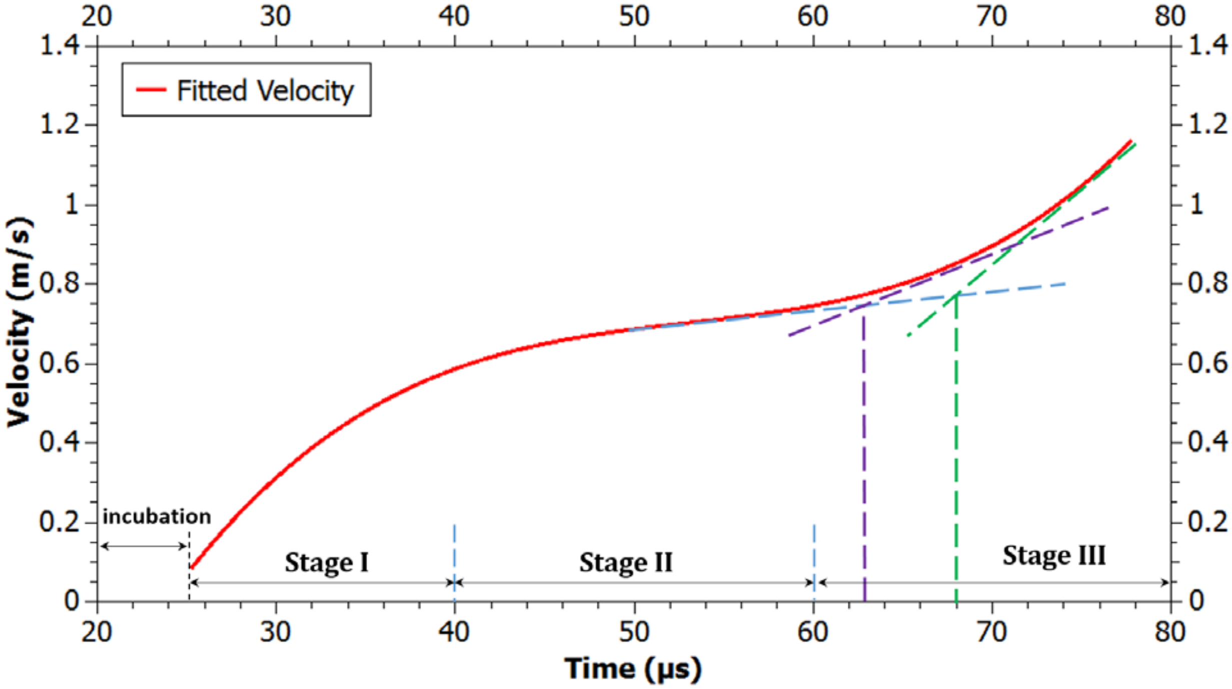

**Figure 40. Solidification velocity evolution during rapid solidification of Al - 11 at.% Cu. Distinct stages of incubation, rapid initial acceleration (stage I), steady state acceleration (stage II) and finally increasing acceleration (stage III) are discernible.**

Based on the analysis of MM-DTEM images sequences and the deduced solidification velocity evolution of Al – 11Cu (Figure 40), the incubation time before the onset of rapid solidification process has been determined as between 22 µs to 25 µs. In our hypotheses, it was postulated that the increase of Cu content in the hypo-eutectic Al – Cu alloys would lead to longer incubation time compared to pure Al. This was rationalized by the effect of the Cu addition on the melting point of hypo-eutectic Al – Cu alloys, which decreases as the Cu content increases. For the lower melting point alloys with higher Cu content, more thermal energy (enthalpy delivered by the sample drive laser) needs to be dissipated to establish the required undercooling at the liquid-solid interface to initiate the rapid solidification process. Given that small effects from Cu content changes in the hypo-eutectic range of Al-Cu alloys on the heat capacity and heat conduction, it is reasonable to conclude that they remain essentially constant and hence longer incubation times are required prior to onset of rapid solidification in hypo-eutectic Al – Cu alloys with higher Cu contents. The in situ MM-DTEM observation are consistent with this argument and therefore confirmed this postulate.

After rapid solidification commenced, it is evident from the velocity evolution plots in Figure 40 that the solid-liquid interface accelerated as rapid solidification progressed at about 25 µs after delivery of the sample drive laser pulse. In an initial stage of crystal growth, the solid-liquid interface velocity increased to ~ 0.56 m/s with a large and close to constant acceleration, possibly due to the steep thermal gradient initially, in the ~15 µs duration time interval from 25 µs to 40 µs. In a second stage of about 20 µs to 25 µs duration from about 40 µs to ~ 60 µs, the interface continues to accelerate at a constant but now reduced magnitude acceleration compared to the previous stage. At the end of the second stage of rapid solidification, the velocity of the crystal growth interface reached a value of ~ 0.8 m/s. In the third and final stage of rapid solidification crystal growth in Al – 11Cu, the solid-liquid interface velocity rapidly increases with an increasing rate of acceleration over the ~15µs duration of the final crystal growth stage, reaching ultimately a maximum of ~ 1.2 m/s before solidification completed (Figure 40). Accelerations of $3.4 * 10^4$ m/$s^2$ and $1.4 * 10^4$ m/$s^2$ have been determined as for the first and second stages that can be distinguished for the rapid solidification process of the Al-

11Cu (Figure 40). The average crystal growth rate associated with the solid-liquid interface velocity for the duration of the rapid solidification from 25 μs to 77.9 μs has been determined as $v_{SL}^{avg}$ ~ 0.72 m/s. The average velocity calculated based on in situ MM-DTEM observation demonstrates a clear advantage of this in situ method over some methods conventionally used in rapid solidification research that rely on indirect measurements to determine the start and completion of solidification (e.g. TCM method [45]). For example, in the case of rapid solidification depicted in Figure 40 for the Al-11Cu, the TCM method would treat t = ~ 0 μs as the starting point of the rapid solidification process and t = ~ 77.9 μs as the end point of solidification. Therefore, TCM method approaches would fail to take into account the incubation time before rapid solidification process actually commences. The average velocity calculated from dividing the total distance that the interface has migrated, 38 μm on average in this case, by the total solidification time of 77.9 μs would yield an average velocity of ~ 0.48 m/s, underestimating the average velocity of ~ 0.72 m/s determined from direct observation of the transformation interface by 32%.

Furthermore, TCM method based experiments are insensitive to the changes in velocity and thus the different stages of rapid solidification, which can be discerned clearly in Figure 40. If the transformation front velocities change in such a fashion that the cross-over some critical values, crystal growth mode changes may be associated with these apparent changes in the interface dynamics, captured clearly in the MM-DTEM based in situ experiments. Based on the SMSM of Al – Cu alloys proposed by Kurz *et al.* (see section 3.3) [35], in the hypo – eutectic Al – 11Cu (~ Al – 23 wt.%) alloy, for velocity values below ~ 1 m/s, i.e., the velocity developed in the thin film Al-11Cu studied here between 25 µs and a time point between 60 µs – 70 µs, should correspond to the growth of α-cells (see Figure 9 in section 3.3 and reference [35]). For velocities above 1 m/s, i.e., the final stage in Figure 40 characterized by the significant and increasing acceleration of the transformation interface, the SMSM predict a change of the crystal growth mode from α-cells to banded microstructure formation [Figure 9 in section 3.3 and reference [35]]. In this study, the tangential method [28] was used to determine the approximate times and this critical velocities for the growth mode transition from α-cells (stage II in Figure 40) to banded microstructure (stage III in Figure 40). Using without prejudice reasonable constraining ranges for fitting slopes to the increasing acceleration regime of the velocity in stage III, the starting time for the change of crystal growth mode (from α-cells to banded microstructure) can be estimated to occur between ~ 63 µs to ~ 68 µs. This corresponds to a critical interface velocity in the range of 0.76 m/s to 0.85 m/s or about 0.80 m/s on average.

Using the approximate time intervals determined from the in situ MM-DTEM experiments (Figure 35 to Figure 40) for critical transition from incubation to crystal growth (commencing with stage I in Figure 40) and the crystal growth mode transition from α-cells to banded morphology microstructure formation during rapid solidification as a guidance, time-resolved MM-DTEM imaging experiments at the relevant time delays with shorter inter-frame time and at higher imaging magnification were conducted on the Al – 11Cu alloy thin films. The purpose of the higher spatio-temporal resolution experiments was the capture of more highly resolved details of the rapid solidification process during these critical transitions between different stages of the solid-liquid-solid transformation processes in response to the sample drive laser pulse irradiation. Figure 41 presents three images extracted from one image sequence with higher spatio-temporal resolution that have been acquired at t = 23.5 µs, 24.5 µs and 25.5 µs after the laser pulse delivery, respectively. These images therefore corresponding to the temporal limit of the incubation period prior to onset of directional crystal growth of the rapid solidification process determined from the low-magnification MM-DTEM observation (Figure 40). The "after" image was taken minutes after the solidification process completed. It is evident that the "seeding grains" for subsequent directional crystal growth have formed around the perimeter of the melt pool at t = 23.5 µs, 24.5 µs and 25.5 µs and are evolving relatively slowly during the observed time window of 2 µs duration. For instance, the grey level and also shape of one single grain highlighted by the red dashed circle in Figure 41 is clearly different in the three images presented. It appears that the grain is relatively small at t = 23.5 µs and starts to increase in size, growing to protrude out further from the almost planar liquid – solid interface at t = 24.5 µs. However, it appears to shrink and revert back to become level with the liquid – solid interface again at t = 25.5 µs. The change of grey level can be associated with the change of physical aspects of the grain, such as grain orientation, degree of crystallinity or size of the grain. Both of the aforementioned phenomena are indicating that some of the grain at the liquid-solid interface are still evolving, fluctuating between different somewhat "unsettled" states. Notably, during this period of observation the average position of the liquid-solid interface remains unchanged and no noticeable directional growth is observed. It is proposed here, somewhat speculatively, but based on these characteristics of the in situ MM-DTEM observations of the liquid-solid interface towards the end of the incubation period, that these fluctuations are associated with the final transient of the thermal conditions prior to the onset of directional rapid solidification crystal growth. The excess heat (enthalpy) deposited by the sample drive laser pulse irradiation results in an initial melt pool that is superheated. Dissipation of this excess of heat is accomplished primarily by heat conduction through the metal/alloy thin film layer from the hot melt pool to the surrounding colder solid (see section 5.3 and Ref. [97]). Hence, initially during the incubation period immediately after sample driver laser pulse irradiation dissipation of this excess heat results in expansion of the melt pool, melting of the adjacent solid. During the incubation stage the required thermal and/or constitutional conditions develop that facilitate eventually the subsequent directional crystal growth stage.

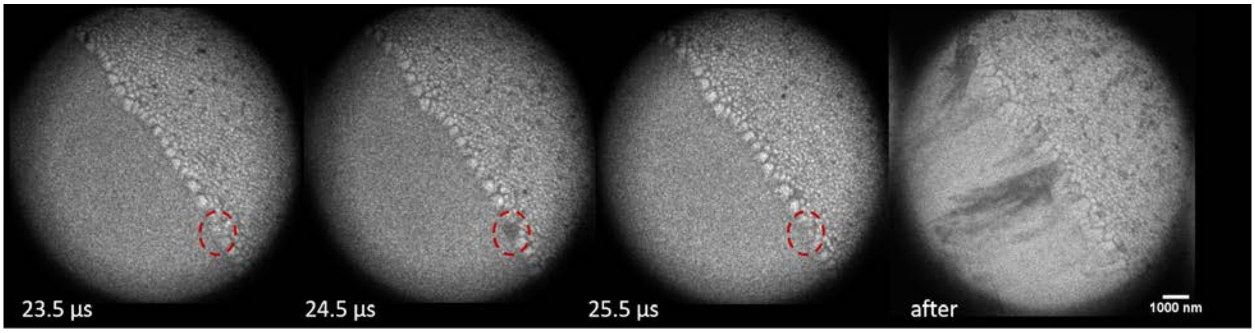

**Figure 41. Images extracted from one MM-DTEM image sequence showing the incubation period**

Figure 42 displays a high spatio-temporal resolution MM-DTEM image sequence taken with 65 µs delay time and 500 ns inter-frame temporal spacing and an enlarged view of the image at t = 65.55 µs, capturing the evolution of the center of the melt pool 65 µs after the initial laser irradiation. The time stamp below each image indicates the associated time delay of each image (in µs) and the image labelled as “Re-solidified” was taken after the solidification completed. The time span of the image sequence corresponds to a potential crystal growth mode change, marked by the rapidly increasing solidification velocity based on the velocity evolution analysis in Figure 40. At t = 65 µs, part of the melt pool is still out of the field of view so it is difficult to make a conclusive evaluation, but banded microstructure has already formed at t = 65.55 µs, which is more clearly illustrated in the enlarge view of image at t = 65.55 µs in Figure 42. This further demonstrates the unique capability of the in situ MM-DTEM technique to provide nano-scale spatio-temporal resolution for observing transient processes. Combining the MM-DTEM based high-magnification observation of locally resolved phenomena, low-magnification image sequences of the overall evolution of the in situ laser irradiation induced rapid solidification provided and the corresponding solidification interface velocity evolution analysis, it can be concluded that the crystal growth mode transition occurred slightly earlier than t = ~ 65 µs after the laser irradiation pulse delivery and the growth of α-cells switched to formation and growth of banded microstructure at a critical velocity of 0.8 ± 0.05 m/s.

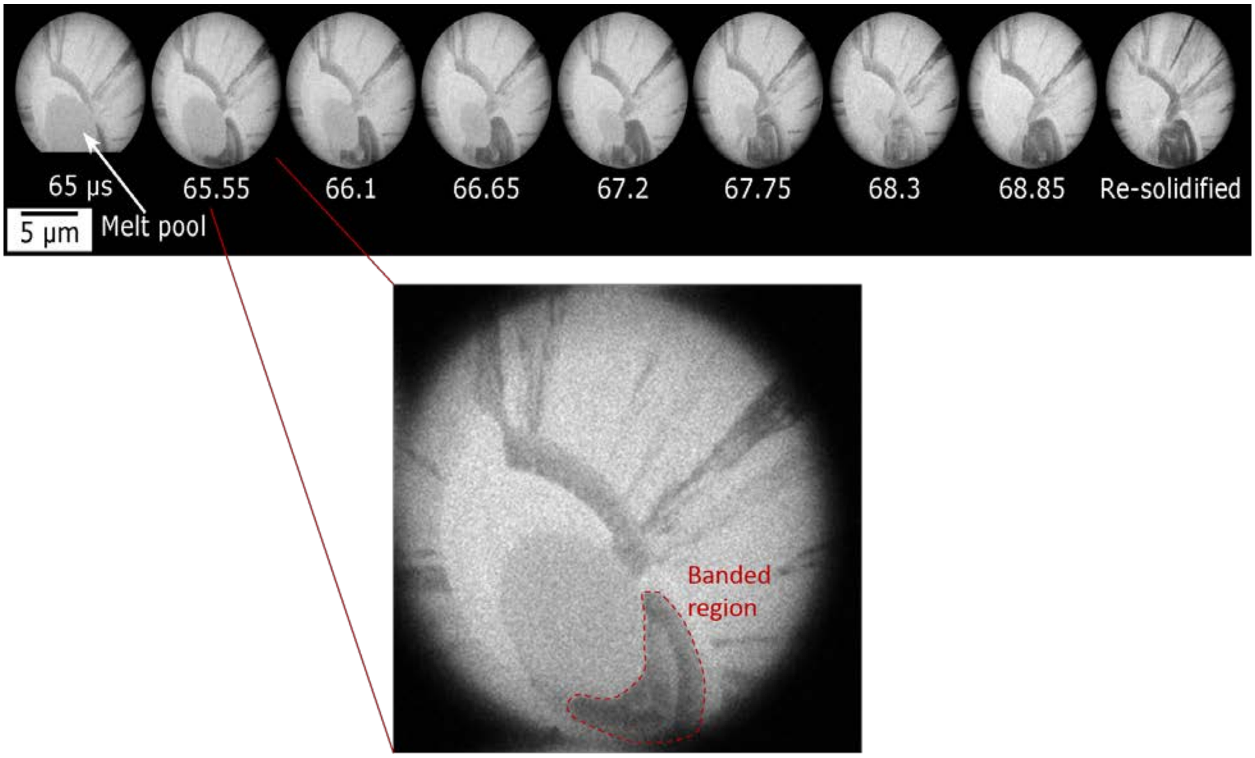

**Figure 42. High spatial-temporal resolution MM-DTEM image sequence with 65 μs delay and enlarged view of image at t = 65.55 μs, showing the evolution of the central region of the melt pool**

The existing solidification microstructure selection map (SMSM) of Al – Cu alloys suggests that the transition from growth of α-cells to banded morphology should occur at ~ 1 m/s for Al – 11Cu (~ Al – 22.5 wt.% Cu), as indicated by the yellow dashed line in Figure 43. As mentioned previously, the current SMSM is based on post-mortem characterization by nature. In addition, interface velocities above 0.5 m/s in the bulk specimen was not experimentally measured but actually calculated from numerical modeling results in the current SMSM. Therefore, large uncertainties are associated with the data points in the current SMSM. The result of current study on the rapid solidification behavior of Al – 11Cu is in reasonable agreement with existing SMSM predictions for Al – 11Cu. However, when determining the critical velocity for the change of crystal growth mode to occur, the estimated velocity based on direct observation has an error bar of only 6.25%, which is a drastic improvement over the data reported in previous work [35]. In addition to the current study, previous investigations by K. Zweiacker [28] on the rapid solidification process of Al – 4Cu (~ Al – 9 wt.% Cu) using the MM-DTEM experimentation has found that the microstructure evolution in Al – 4Cu is consistent with prior reports by W. Kurz and his co-workers [37,63] and the critical velocity for the change of growth mode from α-cells to banded morphology to occur is ~ 1.7 m/s, while the current SMSM predicts a critical velocity of ~ 2 m/s for the Al – 4Cu alloy, as indicated by the green dashed line in Figure 43. Therefore, results from in situ MM-DTEM experimentation on Al – 4Cu alloy and Al – 11Cu alloy are in reasonable agreement with prediction of the previously reported Al – Cu alloy SMSM proposed by W. Kurz *et al.*[35]. However, the MM-DTEM in situ experiments provide higher precision quantitative interface velocity measurements and interface velocity evolution determination than prior experimentation. The MM-DTEM based rapid solidification studies performed here support and confirm the general assessment and theory developed regarding the rapid solidification process in hypo-eutectic Al – Cu alloys suggested by W. Kurz and his co-workers [37,63,111]. The direct observation based velocity evolution analysis of Al – 4Cu and Al – 11Cu alloys showed vastly improved precision for interface velocity measurements, improved accuracy regarding details of the individual and discernible stages of the rapid solidification transformation sequences, and suggests potential minor but significant modification of the current SMSM of Al – Cu alloy in the hypo-eutectic range.  For instance, shifting the transition boundary between the growth of α-cells and banded morphology down because lower critical velocities have been consistently observed for the growth mode transition to occur in both Al – 4Cu and Al – 11Cu alloys by in situ MM-DTEM experimentation.

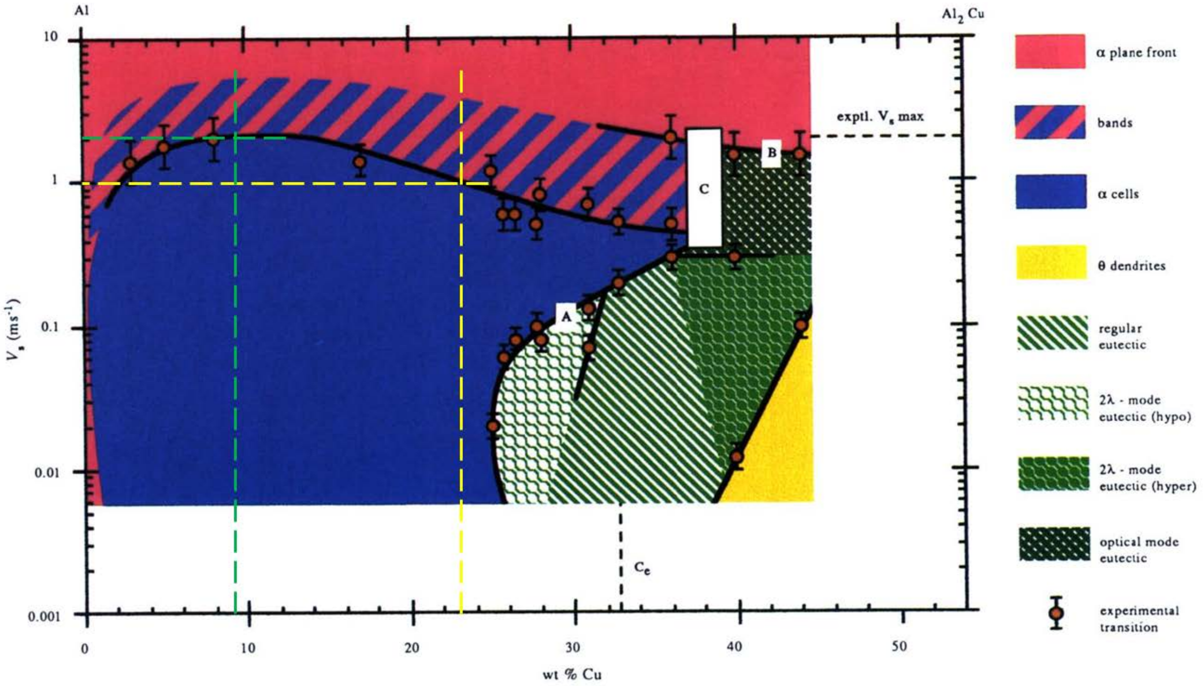

**Figure 43. Rapid solidification process of Al – 4Cu (Al – 9 wt.% Cu, indicated by green dashed line) and Al – 11Cu (Al – 23 at.% Cu, indicated by yellow dashed line) suggested by existing SMSM**

To summarize, the rapid solidification process in and Al – 11Cu alloy thin films lasted slightly longer than 77.9 μs with an incubation stage duration of ~ 25 μs. After the incubation stage, the solidification interface accelerated with different but close to constant acceleration values during 25 μs to 40 μs (Stage I in Figure 40) and 40 μs to 65 μs (Stage II in Figure 40). At ~ 65 μs, the solidification velocity reached 0.8 m/s, which lead to an interface instability [112,113] and a crystal growth mode change from α-cell growth to banded morphology growth. The solidification front migrated with increasing acceleration until the completion of the solidification process during the banded morphology growth (Stage III in Figure 40). The overall average velocity of the rapid solidification process has been determined as 0.72 m/s, with incubation stage duration accounted for. In general, the results and quantitative metrics obtained by the current in situ MM-DTEM study and previous investigation are in agreement with SMSM proposed by W. Kurz and co-workers. However, the higher precision and high accuracy direct observation based results of the current work suggested lower critical velocities for growth mode transition from a-cell to banded morphology crystal growth in the hypo-eutectic range of the Al-Cu than are predicted by the SMSM published by W. Kurz and co-workers.

### 6.2.2 Post-mortem characterization of rapidly solidified microstructure in hypo-eutectic Al – Cu alloy thin films

Although MM-DTEM experimentation provided direct observation of the rapid solidification process and enabled accurate identification of different stages in the rapid solidification process related transformation sequence and associated velocity evolution, post-mortem characterization of the rapidly solidified microstructure in the Al – 11Cu thin films is still necessary to further correlate the solidification conditions and quantify the influence of increased Cu content on the mechanistic details of the Al-11Cu alloy rapid solidification behavior.

A montage of TEM BF images of an example melt pool formed after in situ pulsed laser irradiation induced rapid solidification is shown in Figure 44 a). Similar to observations reported for rapidly solidified melt pools in Al – 4Cu thin films [28,114], four zones with morphologically distinct microstructure can be identified and named as zone 1 to zone 4 here. Zone 1 is the heat affected zone (HAZ) that consisted of significantly coarsened grains compared to the as-deposited film. Formation of zone 1 can be attributed to the initial heating of the as-deposited thin film by the laser pulse with a Gaussian profile that lead to partial melting of grain boundaries in the thin film, as discussed in section 5.3.2 and reference [28]. Also, similar to situations described in section 5.3.2, heat conduction from the superheated melt pool through the plane of the alloy film during the rapid solidification process can cause grain coarsening in this region. Zone 2, the transition zone, is defined as the region where decoupled crystal growth of the primary solidification product of α-Al phase and secondary eutectic product in the intergranular regions between the primary Al phase grains transitions to the coupled growth zone of the α-cells in Zone 3. The α-cells are dendritic cells constituted of a kinetically modified eutectic of irregular, i.e. non-lamellar, morphology. Zone 3, the columnar growth zone, developed during directional and coupled growth of dendritic cells of supersaturated α-Al and θ-$Al_2Cu$ related Cu-enriched phases. Eventually, as discussed in section 6.2.1, the solidification velocity surpassed the critical velocity for a change of crystal growth mode to occur and banded morphology microstructure forms. The banded morphology growth involves growth into the positive thermal gradient anti-parallel to the heat extraction direction and also laterally along the respective isotherms ahead to the advancing solidification front in the melt pool.

Details of the microstructural characteristics and composition variations that developed in the four morphological zones, i.e. zone 1 to zone 4, during rapid solidification are more clearly shown in Figure 45. Figure 45 compiles a series of high-angle annular dark field (HAADF) STEM images of a melt pool formed after rapid solidification. The brighter contrast regions corresponds to Cu-richer area and darker regions corresponds relatively Cu-depleted area, since the contrast in HAADF-STEM images strongly depends on the atomic number [109]. Figure 45 a) is a montage of HAADF-STEM images showing all four morphological zones in the melt pool and their relative scale and evolution path and Figure 45 b), c) and d) are enlarged HAADF-STEM images with more detailed information on the microstructural features of different morphological zones. The numbers in the images represent corresponding morphological zones (i.e. 1 means zone 1) and different zones are separated by yellow dashed lines. The yellow arrows in Figure 45 a) and b) indicate the direction of radially outward directional heat extraction through the film. Figure 45 a) indicates that the grains that underwent directional growth occupy the majority of the melt pool and only a small region of ~ 8 μm width along the major axis in the center of the melt pool exhibits banded morphology. The micrograph in Figure 45 b) has been obtained from the edge of the melt pool and the transition from the incubation stage with the “seeding grains” along the perimeter of the melt pool and shows the transition from the HAZ (Zone 1) via the transition zone (Zone 2) to the a-cell rapid solidification growth zone (Zone 3) (Markers 1, 2, and 3 in Figure 45b). The transition an associated morphological change from incubation and seeding to subsequent columnar growth is evident. Columnar morphology grains of the α-cell growth regime (Stage II, marked in Figure 40) located further away from the transition zone 2, deeper into the melt pool are shown in Figure 45 c). Based on the morphology of the banded microstructure presented in Figure 45 d) (bottom right corner) and the two surrounding grains labeled as B1 and B2, it is clear that the banded microstructure grew not only anti-parallel to the heat extraction direction but also along the isotherm present along the perimeter in the melt pool. The micrograph of Figure 45 d) indicates that multiple columnar α-cell grains more or less simultaneously reached the critical velocity for the growth mode change. The α-cells of the microstructural Zone 3 therefore grow competitively with each other, faster growing grains successfully occluding slightly slower growing adjacent grains. As a result, multiple α-cells columnar grains can reach the critical velocity and multiple banded morphology grains from them to produce the complex morphology at the center of the rapidly solidified Al-11Cu, Zone 4. Notably, Zone 4 is comprised of several but relatively few very large banded morphology grains (e.g. marked as B1, B2 and B3 in Figure 45 d)).

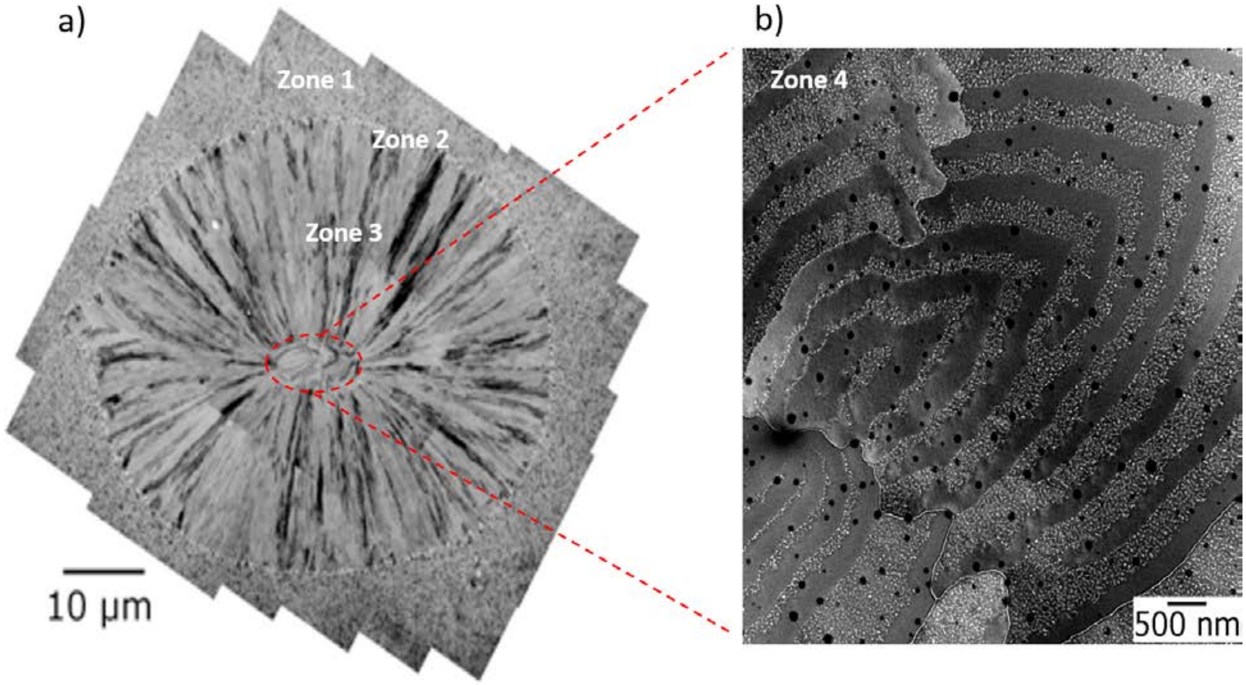

**Figure 44. a) Montage of TEM BF images showing an example melt pool formed after in situ laser irradiation and four morphological zones. b) HAADF of image of zone 4, the banded morphology region.**

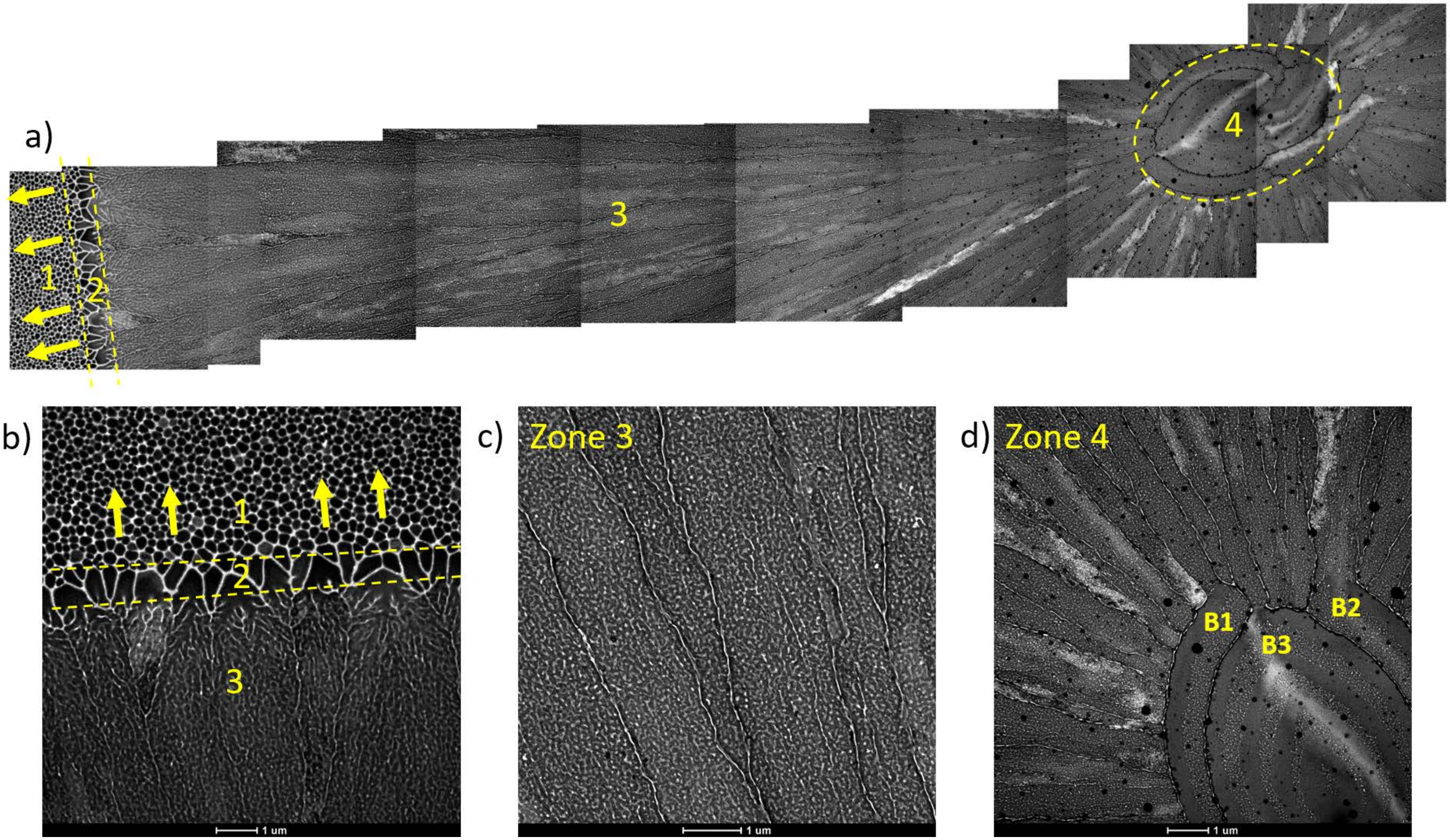

**Figure 45. HAADF STEM images showing a) Zone 1 to Zone 4 in the in situ melt pool, b) Transition from zone 1, HAZ to zone 3, columnar growth, c) Columnar grains further out in the melt pool and d) Banded morphology in the center of the melt pool comprised of only a few separate banded grains, marked as B1, B2 and B3.**

Figure 46 a) presents the HAADF STEM image taken at the edge of the in situ melt pool in Al – 11Cu alloy thin film and Figure 46 b) shows a HAADF STEM image, taken at an equivalent location in Al – 4Cu alloy thin film, at the same scale. A comparison reveals the effects of increased Cu content on the solidifed microstructure. First, the witdth of the inter-granular Cu-enriched area is in general wider in the Al – 11Cu alloy thin film, i.e., the α-Al grains are more celarly separated than the equivalent primary phase Al grains in the Al – 4Cu alloy thin film. This trend regarding the scale coarsening of the microstructural constituents becomes more obvious at locations that are closer to the edge of the in situ melt pool and most promient in zone 2, the transition region (double-headed arrow in Figure 46 a). The transition regions for the Al-11Cu and Al-4Cu hypo-eutectic alloys are schematically highlighted by the yellow dashed lines in Figure 46 a) and b) respectively. The average width of the transition region have been measured to be ~ 750 nm around the in situ melt pool in Al – 11Cu alloy thin film and ~ 550 nm for the Al – 4Cu alloy thin film. It is clear that the Cu-enriched phases are seperating the α-Al phase grains that are about to grow directionally in zone 2 of the Al – 11Cu alloy thin film, while the Cu-enriched phases only appear to be fine lines between the grains in zone 2 of the Al – 4Cu alloy thin film. Moreover, over a short (~100 nm wide) but noticeable distance along the directional crystal growth path towards the cneter of the melt pool, grains in zone 2 of Al – 11Cu alloy thin film exhibit evidence for an approximately lamellar eutectic solidifcation product (circled in Figure 46 a)). The coupled growth for a eutectic solidification product indicates the end of the transition region from crystal growth of solidificaiton products at two diferent temperatures, namely the pro-eutectic super-saturated α-Al (primary solidification product) and the Cu-enriched secondary solidification product (bright contrast in Figure 46 a) and b)), which represents a eutectic cosntituent. The small scale of the regions between the primary constituent α-Al phase grains (10 - 30 nm) prevented the formation of the more familiar two-phase lamellar morphology in the secondary eutectic constituent of the microstructure in Zone 1 and Zone 2 of the rapidly solidified microstructures. The steep acceleration of the crystal growth rate inferred by the solidification front velocity analysis presented in the previous section (e.g. Figure 40) would be consistent with the directional growth of the primary α-Al phase based solid solution grains, which are dendritic cells of kinetically modified, i.e. presumably supersaturated, α-Al that evolve to large width and occlude neighboring α-Al grains in the transition zone, Zone 2 (e.g. Figure 46). The freezing of the significantly Cu-enriched melt in the inter-dendritic/inter-cellular regions between these short and stubby α-Al dendricitc cell tips occurs at a lower temeprature than the tip temperature. The transition from approximately near-equilibrium solidifcation during the incubation period to the externally therml gradient driven directional rapid solidification crystal growth is accomplished over the width of the Zone 2 region, ~750 nm and ~550 nm for the Al-11Cu and Al-4Cu alloys. The increased Cu fraction in the Al-11Cu alloy relative to the Al-4Cu results in a discernible, albeit very narrow (≤ 0.2μm), region where single phase growth of the α-Al dendritic cell changes to coupled growth of two solid continues phses from the melt, a eutectic product, before transitioning to α-cell growth of the columnar morphology grains in Zone 3 (Figure 46 a)). For the Al – 4Cu alloy thin film the transitions from the single phase α-Al phase growth in Zone 2 to the coupled eutectic product growth in Zone 3 appears to be much sharper with a significanly less well developed or entirely absent continuous two-phase lamellar microstructure (Figure 46 b)). These observed microstructure characeristics can be attributed to the increased Cu content in the Al-11Cu relative to the Al-4Cu. With increased Cu content, the melting point of the Al-11Cu alloy is ~ 60 K lower than that of Al-4Cu, which leads to greater extent of partial melting, preferreably along the intergranular regions between Al-phase grains, giving rise to the wider inter-granular Cu-enriched areas and longer incubation time before columnar growth in zone 3. The longer incubation time and slower increase of solidification velocity in Al – 11Cu alloy compared to those of Al – 4Cu alloy allowed solidification closer to equilibrium condition for a short period of time. After this period of time, columnar growth of grains commenced and the dendrite-like morphology is retained over a short distance in zone 2 of in situ melt pool in Al – 11Cu alloy thin films. In addition, it can be observed that the majority of the Cu-rich phase features, likely to be θ-$Al_2Cu$ or θ-related phases, are interconnected in the columnar grains in zone 3 of the in situ melt pool in Al – 11Cu alloy thin film. Therefore, the Cu-enriched solidification product forms an interconnected but not lamellar morphology network with the majority Al-based phase in the eutectic cell grains of Zone 3. The equivalent Zone 3 grains in the microstructure of the in situ melt pool in Al – 4Cu alloy thin film exhibit also a two phases but the Cu-enriched solidification products are distincly seperated from each other within a matrix formed by the Al-phase. Since the equilbrium weight percentage of θ phase at room temperature for Al – 4Cu alloy is ~ 17 wt.% and ~ 43.4 wt.% for Al – 11Cu alloy, it is expected that the area/volume fraction of θ-$Al_2Cu$ phase are higher in the in situ melt pool of Al – 11Cu alloy. The increased equilibrium volume fraction of the θ-$Al_2Cu$ phase expected in the Al-11Cu alloy relative to the Al-4Cu alloy would be consistent with the clealry discontinuous distribution of the Cu-enriched phase within the columnar morphology grains formed in Zone 3 for the latter. Alternatively, this difference on the morphology of the Cu-enriched pahses in the eutecic cells of Zone 3 in the Al-11Cu and Al-4Cu alloys could also have been caused by the considerably higher solidification velocity in the latter. It has been observed that high solidification velocities can disrupt the continuity of the growth rate limiting phase, the $Al_2Cu$ based phase, in eutectic growth behavior in Al – Cu alloys [35].

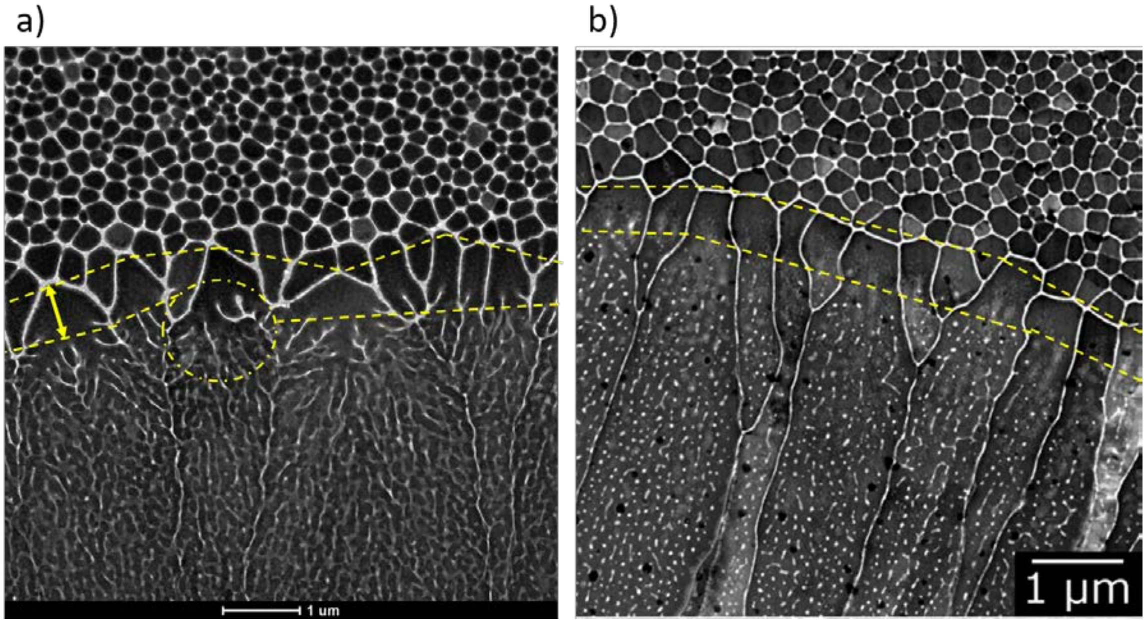

**Figure 46. a) HAADF STEM image taken at the edge of the in situ melt pool in Al – 11Cu alloy thin film. b) HAADF STEM image adapted from** [114] **showing the edge of the in situ melt pool in Al – 4Cu alloy thin film. Zone 2, the transition zone, is highlighted by yellow dashed lines in both images.**

STEM imaging and STEM-EDS based measurements and composition mapping have been performed at the edge (zone 1 to zone 3) of the in situ melt pool in Al – 11Cu alloy thin film. The composition mapping facilitates development of understanding of the composition variation developed during the initial stages of rapid solidification processes, i.e. stage I to beginning of Stage II marked in the interface velocity plot of Figure 40. A summary of the composition mapping results is shown in Figure 47. Figure 47 a) shows the HAADF-STEM image of the examined area and Figure 33 b) presents the associated color coded Cu concentration level map. In Figure 33 b) redder color represents higher concentration level of Cu. Obvious correlation between the contrast in Figure 47 a) and the Cu concentration level shown in Figure 47 b) can be noticed. Quantitative STEM-EDS measurements of specific areas and also line scans for detecting compositional change along the scanned direction have been conducted for specific locations marked in Figure 47 a) using yellow circles (#1 - #4) for area measurements and yellow arrows (#5, #6 and #7) for line scans. The compositions from area measurements in terms of atomic percent of Cu are summarized in Table 9. It can be seen that the composition of grains in the HAZ and the seeding grains at the edge of the melt pool (e.g. #1 - #3) for transition to directional crystal growth are very similar, with an average composition of Al – 3. 62 at.% Cu. The essentially equiaxial morphology α-Al phase grains in Zone 1 (HAZ) and the 'seed' region of the α-Al grains in the transition to Zone 2 correspond to supersaturated α-Al solid solution. The composition of the inter-granular phase was measured as Al – 31.48 at.% Cu, essentially corresponding to the equilibrium composition of θ-$Al_2Cu$ phase (e.g. region marked #4, Figure 47 a)). Composition variations in terms of Cu concentration along the line scans parallel to the directional growth towards the center of the melt pool are shown in Figure 47 c). There is a general trend of increasing Cu content along the scanned direction. For instance, in line scan 5, the Cu concentration started from 3 at.% Cu at the origin of the line scan, gradually increased to 6 at.% Cu at the end point of the line scan (arrowhead in Figure 47 a)), with some fluctuations in between. This trend is even more apparent in line scan 6 and line scan 7, in which the Cu concentration increased from 3.8 at.% Cu to 8 at.% Cu in line scan 6 and from 3.8 at.% Cu to ~ 10 at.% Cu in line scan 7, respectively. These consistently observed trends for increasing Cu content in the increasingly supersaturated α-Al grains in the transition zone (Zone 2) can be explained by the rapid increase of solidification interface velocity determined for this initial stage of the direction crystal growth processes during the rapid solidification of the Al-11Cu alloy (Figure 40). With the rapidly accelerating solidification interface, the width of the boundary layer in the liquid ahead of the solid rapidly decreases in nominal width. This results in an increasing level of Cu solute aggregation at the liquid-solid interface as the time available for solute, Cu, re-distribution by diffusion in the liquid ahead of the moving interface continuously decreases. This causes the rapidly solidified α-Al to become more and more supersaturated along the crystal growth direction as the crystal growth front velocity increases rapidly in stage I of the rapid solidification process (see Figure 40). Figure 47 further shows that after a short distance on the order of about 250 nm to 400 nm the single phase directional growth of increasingly supersaturated α-Al solid solution crystals reaches a critical velocity and composition that facilitates a first transition in crystal growth mode to the coupled growth of the kinetically modified eutectic product formed in the Zone 3 of the Al-11Cu microstructure during the rapid solidification, i.e. Stage II in the solidification interface velocity plot of Figure 40.

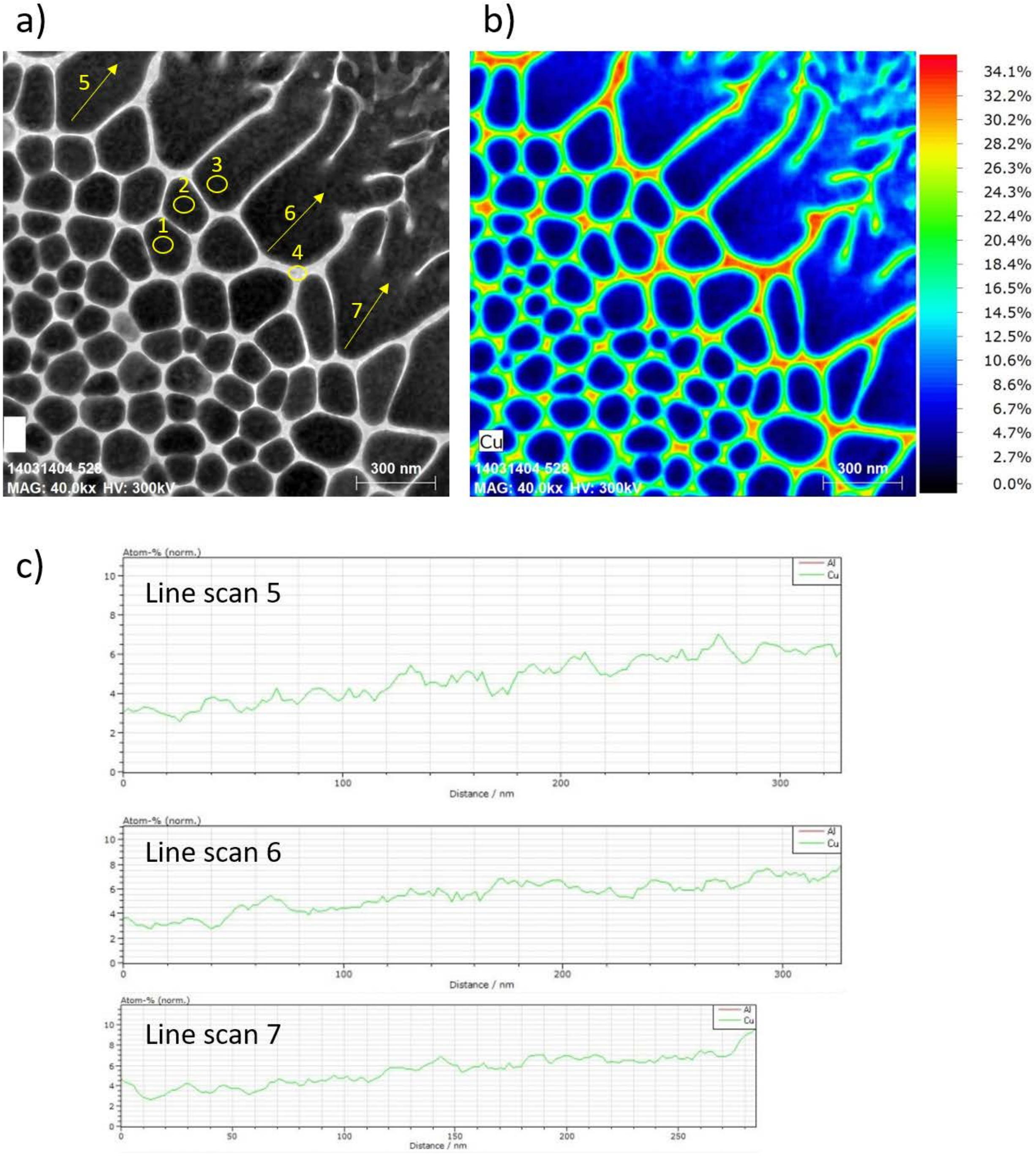

**Figure 47. a) HAADF image taken at the edge of in situ melt pool with yellow circles indicating location for area EDS measurements and lines for line scan. b) color coded EDS mapping showing Cu concentration levels. c) Atomic percent of Cu along corresponding EDS line scans**

**Table 9. Atomic percent of Cu in EDS measurements shown in Figure 47**

| Location | at.% Cu |
|---|---|
| **1** | 3.79 |
| **2** | 3.62 |
| **3** | 3.45 |
| **4** | 31.48 |

Similar STEM-EDS measurements and mapping have also been performed at the banded region of the in situ melt pool in Al – 11Cu alloy thin film for demonstrating the composition variation developed during the late stage of rapid solidification process (Stage III in Figure 40) and an example of the results is shown in Figure 48. Areas for which quantitative STEM EDS measurements have been performed are indicated by red rectangles (#1 - # 4) and red circles (#5 - #8) in Figure 48 a). Figure 48 b) presents the corresponding color coded Cu concentration map based on STEM EDS mapping of area shown in Figure 48 a). The atomic percent of Cu of the marked and labeled measurement areas are tabulated in Table 10. It can be seen that the measured composition from relatively large area measurements of the partitionless region and partioned region (scans #1 - #4) are the same as the film composition, i.e. Al – 11Cu. Averaged composition from measurements #5 and #6 on the Cu-rich phases is Al – 18.68 at.% Cu. This is significantly deficient in Cu content relative to the equilibrium composition of θ-$Al_2Cu$

phase. Nevertheless, it is still reasonable to associate the Cu-enriched product phase from the coupled two-phase crystal growth regime of the banded morphology grains with θ or θ-related phases. These now quite discontinuously distributed Cu-enriched phase entities are small and enveloped by the α-Al solid solution phase of the banded morphology grain. The X-ray based EDS signal is an average over the full through thickness of the thin film alloy, which given the embedded nature of the distribution of the Cu-enriched phase features results in a systematic deviation of the composition towards Al. The deviation towards Cu-deficiency for the composition measurements from thin film regions containing the θ or θ-related phases is attributed to the fact that the interaction volume between the scanning electron beam and the sample is considerably larger than the real volume of the Cu-enriched phase crystals and includes always significant contributions from the surrounding Al-matrix. The measurements (#7 and #8) from areas adjacent to Cu-rich phases show signs of Cu-depletion relative to the alloy composition. This is consistent with coupled growth of a strongly supersaturated α-Al phase with composition of about 9.5 at.% Cu, slightly Cu-deficient relative to the 11.7 at.% Cu of the alloy, and a θ or θ-related phase that exhibits Cu-enrichment relative to the alloy composition in the eutectic bands within the banded morphology grains. The STEM image and STEM-EDS measurements confirm the oscillating crystal growth behavior in the banded region, producing alternating bands of partionless crystal growth product regions of single phase α-Al with the alloy composition and bands of a two-phase region of eutectic solidification product. This is consistent with previous observations and associated theories suggested by previous researchers [62,113,115]. It needs to be noted, however, although termed as “partitionless region”, the elemental distribution of Cu in the partitionless bands of the banded region is not truly uniform at the nanoscale accessible by the sub-nanometer electron probe diameter STEM analyses performed here. Based on the color-coded STEM-EDS mapping, it is clear that the partionless region consists of a mixture of blue and green colored regions, which correspond to higher and lower level of Cu concentration, respectively. This indicates that variations of Cu concentration existed in the liquid adjacent to the rapidly migrating solidification interface, which was “frozen” into the newly forming crystal as rapid solidification progressed and retained after solidification completed. Notably, the crystal growth velocity along the bands of single phase α-Al in the banded morphology grains is predicted to exceed the critical velocity reached at the transition from Zone 3, eutectic α-cell growth of the columnar morphology grains to the banded morphology growth. This critical velocity has been estimated from the MM-DTEM measurements presented in Figure 40 as 0.8m/s for the Al-11Cu.

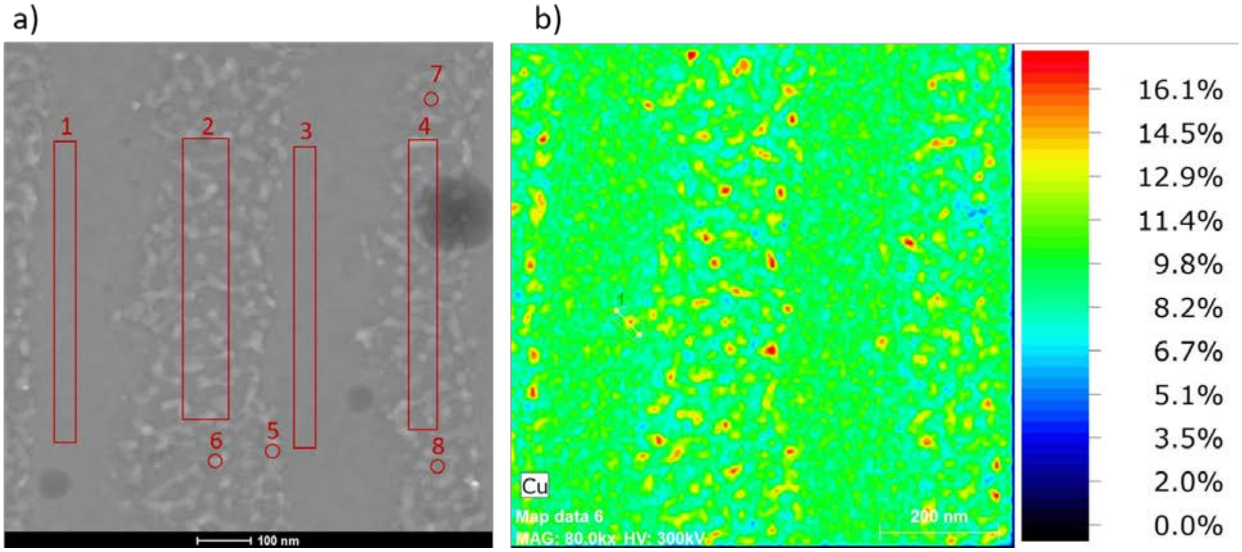

**Figure 48. a) HAADF STEM image taken at the banded region of in situ melt pool in hypo-eutectic Al-Cu thin film with red rectangle and circles indicating location for EDS measurements. b) Color coded EDS mapping of Cu concentration levels.**

**Table 10. Atomic percent of Cu in EDS measurements shown in Figure 48**

| **Location** | **at.% Cu** |
|---|---|
| **1** | 11.06 |
| **2** | 11.06 |
| **3** | 11.3 |
| **4** | 11.17 |
| **5** | 17.14 |
| **6** | 20.21 |
| **7** | 9.43 |
| **8** | 9.77 |

## 6.3 RAPID SOLIDIFICATION IN HYPO-EUTECTIC ALUMINUM – COPPER THIN FILMS BY EX SITU PULSED LASER IRRADIATION

It has been observed that the banded region always originates from the grains that grow along or very close to the major axis of the elliptical in situ melt pool [7,114]. This is due to the changing curvature along the perimeter of the elliptical melt pool. For a given length along the perimeter of the melt pool, parts with higher curvature have access to larger volume of adjacent solid material for heat dissipation, resulting in higher heat extraction rate and hence higher velocities during the solidification process. Areas along and close to the major axis experience the highest curvature and therefore highest crystal growth velocity should be found along the major axis.

Instead of calculating the solidification velocity from change of converted radius from the elliptical melt pool, length evolution of semi-major and semi-minor axes over time can also be used to evaluate and describe the velocity evolution during rapid the solidification process in the Al-11Cu thin films. Based on the low-magnification MM-DTEM sequence presented in section 6.2.1, Figure 35, it is also possible to track the length evolution of the semi-major and semi-minor axes separately during the rapid solidification of hypo-eutectic Al – 11Cu and the result is shown in Figure 49 a). For simplicity here, assuming a constant acceleration, a second-order polynomial can be fitted to the length evolution along each axis. By differentiating the second-order polynomials fitted to the length evolution of the semi-major and semi-minor axes with regard to time, linear expressions of the velocity evolution along each axis can be obtained and are shown in Figure 49 b). Although the velocity evolution determined based on this assumption does not capture the increasing acceleration during the late stage of rapid solidification that is associated with formation of banded microstructure, it still demonstrates that the velocity along the semi-major axis is always higher than that along the semi-minor axis until the solidification is complete. The local velocity of the solidification interface is the highest along the semi-major axis and lowest along the semi-minor axis. Local velocities at other locations around the perimeter of the melt pool should fall in between these two solidification interface velocity extremes. Therefore, grain(s) that grow along the semi-major axis should reach critical velocity that leads to interface instability earlier than other grains. As a result, banded region always originates from the grains growing along or close to the major axis of the elliptical in situ melt pool. This shows the dominant effect of preferred heat transport on the rapid solidification behavior in Al – Cu alloys. The rate of heat extraction drives the interface velocity during the directional crystal growth of the rapid solidification process for the Al-11Cu alloy thin films.

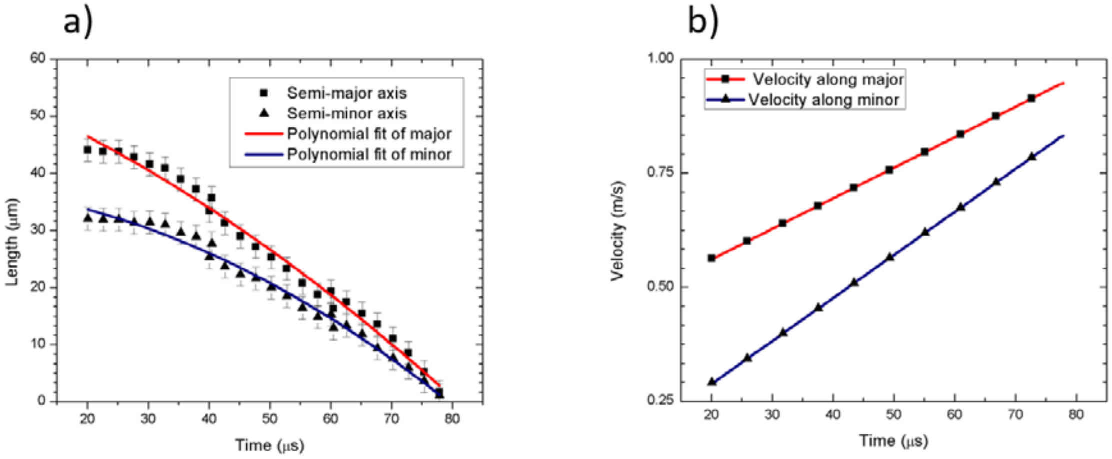

**Figure 49. a) Length evolution of major and minor axis of in situ melt pool. b) Deduced velocity based on length evolution and constant acceleration assumption**

This poses a challenge for investigating other potential governing factors that could significantly affect the rapid solidification behavior, e.g. crystallography of the growing crystals, in in situ experiments. In order to delineate the potential influence of other factors than the heat extraction rate on the rapid solidification behavior in hypo-eutectic Al – Cu alloys, ex situ laser irradiation experiments have been conducted using the set-up described in section 4.4, which facilitates creation of rapidly solidified melt pools with relatively long flat sections along the perimeter of the melt pool.

A typical melt pool formed after ex situ laser irradiation is shown in Figure 50. Figure 50 a) shows an optical microscopy overview image of the ex situ melt pool and Figure 50 b) presents a montage of TEM BF images of the ex situ melt pool. From the optical image displayed in Figure 50 a), the width / length ratio of the melt is ~ 1 / 10. With such a high aspect ratio, a large portion of the melt pool edge along the major axis, as indicated by the red dashed rectangle in Figure 50 b), can be considered as flat and hence will exhibit approximately constant heat extraction rate. Figure 50 b) clearly shows that the grains grew from each side of the melt pool and met at the centerline of the highly elongated elliptical melt pool, demonstrating the symmetrical nature of the laser induced melt pool and heat extraction rate on opposite sides of the melt pool. Banded morphology is not observed in the flat section of ex situ melt pools, indicating the solidification velocity did not reach or exceed the critical velocity, a velocity of ~ 0.8m/s for the Al-11Cu, in the center section. This can be attributed to the limited width of the melt pool, and hence limited time for the solidification interface to accelerate in order to reach and surpass the critical velocity. Notably, along the highly-curved segments at the narrow ends of the elliptical melt pool Figure 50 b)) banded morphology and even a small amount of single phase partionless crystal growth occurred.

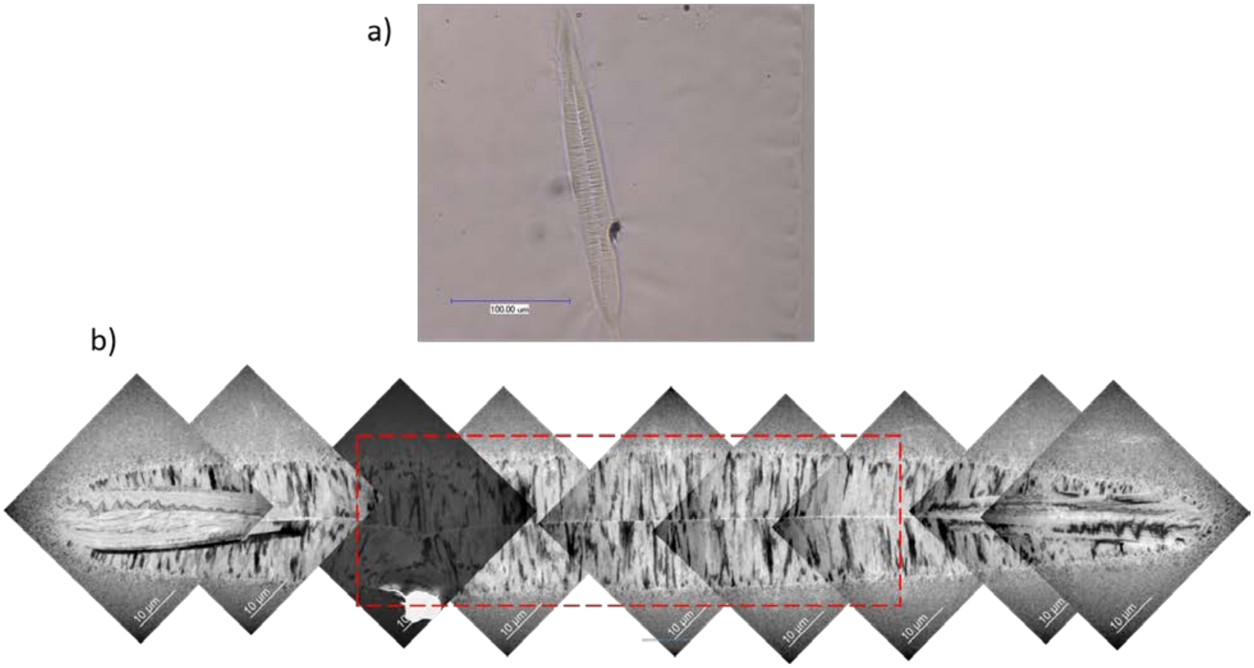

**Figure 50. a) Optical overview of the ex situ melt pool and b) Montage of TEM BF images showing centerline and more details of the ex situ melt pool**

The ex situ laser melting experiments have been performed with a KrF-excimer laser operating at 264nm wavelength in the deep UV-range delivering a ns-duration pulse with a top-hat like profile. Since the laser profile used in the ex situ experiments is different from the Gaussian laser profile used in in situ experimentation, post-mortem characterization of the ex situ melt pool has been performed. Figure 51shows a STEM BF image taken at the edge of the flat section of the ex situ melt pool and three morphological zones, i.e., the heat affected zone (HAZ), the transition zone and the columnar growth zone, can be identified, representing a close resemblance of the morphological zones found at the edge of the in situ melt pool. STEM BF images taken at the edge of flat section of the ex situ melt pool with higher magnification reveal more details of the rapidly solidified microstructure in the ex situ melt pool and an example of such STEM BF image is shown in Figure 52. Akin to what has been observed at the edge of the in situ melt pool (see Figure 46 and Figure 47 in section 6.2.2), the microstructure in zone 2, the transition zone, with the transition from single phase to coupled two-phase crystal growth under the directional rapid solidification conditions is clearly resolved and the columnar morphology grain growth is strongly directional and anti-parallel to the dominant in-plane heat extraction direction. This further proves the similarity between the rapidly solidified microstructure in the ex situ melt pool and the in situ melt pool. Therefore, despite the difference of the laser profiles, it can be concluded that the rapid solidification process induced by ex situ laser irradiation based melting is equivalent and comparable to the in situ pulsed laser irradiation induced rapid solidification process in the hypo-eutectic Al – Cu alloy thin films studied in the in situ time resolved MM-DTEM experiments.

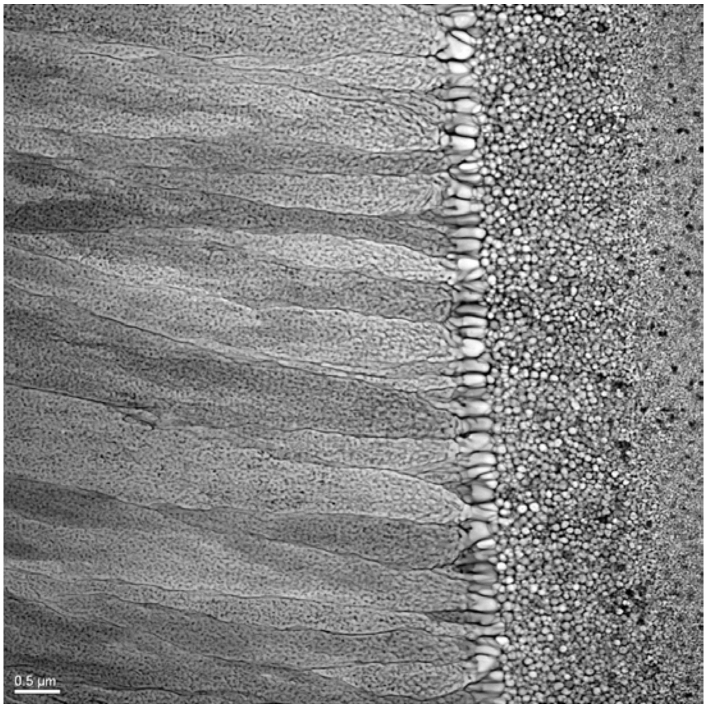

Figure 51. STEM BF image showing the overview of rapidly solidified microstructure around the flat section of ex situ melt pool

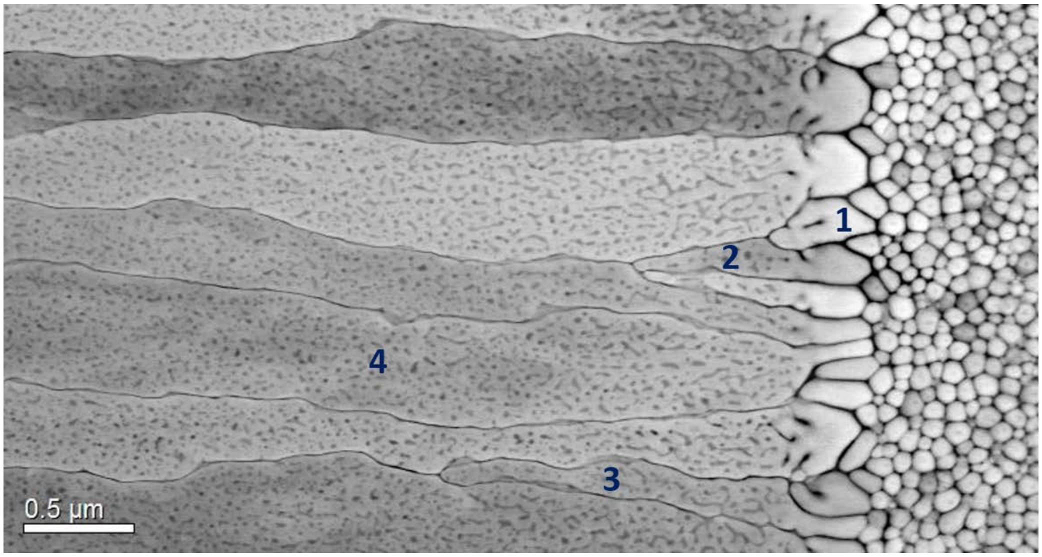

Figure 52. STEM BF image of rapidly solidified microstructure around the flat section of ex situ melt pool at higher magnification. Numbers indicating grains occluded at different stage of solidification process

In Zone 2 and Zone 3, i.e., in the transition zone and during the directional crystal growth of the columnar morphology eutectic α-cell grains competitive growth behavior results in some grains being prevented or blocked from further growth by other adjacent grians more favoured for growth (e.g. see Figure 52). The grains labeled 1 to 4 in Figure 52 can be used to illustrate the different fates of grains associated with the competitive growth behavior:

i. Growth of grain #1 was blocked before or at most right after the initiation of directional gowth at the end of the incubation period.
ii. Grain #2 clearly started to grow directionally and tranitioned from single to coupled two-phase growth of the α-cells of Zone 3 but was blocked by other columnar morphology α-cell grains shortly after directional growth initiated.
iii. Grain #3 grew directionally even further into the liquid under the columnar grain growth regime when compared to grain #2, but ultimately was also blocked by adjacent grains from continued growth.
iv. Grain #4 started out from a relatively small and very narrow grain but quickly grew laterally larger, occluding two initially larger neighboring α-Al grains from reachign the coupled growth zone, and completed growth all the way to the centerline of the ex situ melt pool.

The blocked grains are termed here as occluded grains (e.g. grains #1 - #3 in Figure 52) and the grains that grew all the way to the centerline are termed as favored grains (e.g. grain #4 in Figure 52) in this study. Subsequent investigations aiming at understanding the reason for favored growth of certain grains versus the fate of occlusion during the directional crystal growth have then been conducted.

It is well documented that cubic metals exhibit a preference of growth for dendrites along the <001> direction under conventional solidification conditions [1,104]. During solidification process, the interface migration rate is proportional to the net rate of atom attachment from liquid to solid, i.e., the number of atoms leaving the liquid and attaching to the crystallizing and thus growing solid interface during solidification. In cubic metals {001} surfaces are more open surfaces than the close-packed and lowest interfacial energy {111} planes and other low-index and low interfacial energy planes. The atomic level roughness of the {001} interfaces of cubic metals therefore provides for the most effective accommodation of incoming atom attachments and the <001> directions show the fastest growth for cubic metals during solidification at close to equilibrium conditions. It has been hypothesized that even at the far-from-equilibrium solidification conditions applied in the current study, crystallography can still potentially be an important contributing factor to the favored growth of certain grains and lead to their success in the crystal growth competition we have observed in the columnar morphology grains of the Al-11Cu rapidly solidified microstructures.

In order to examine this hypothesis, TEM PED based OIM scans have been performed at the HAZ adjacent to the ex situ melt pool and the color-coded IPF maps based on the OIM scan is shown in Figure 53. Figure 53 a) shows the a color-coded IPF map viewed from z-direction (parallel to the electron beam and film normal). The majority of the grains are colored as green or close to green, representing preference for selection of <011> directions parallel to the film normal. Meanwhile, the color-coded IPF map for the x-direction (parallel to the in-plane horizontal direction) shown in Figure 53 b) does not exhibit noticeable preference for directions. The pole figures associated with the HAZ clearly exhibit a minor <001> texture with respect to the film normal direction and an essentially random distribution for in-plane directions. Recall that the crystallographic characteristics of the as-deposited hypo-eutectic Al – Cu films were investigated using PED TEM based OIM scans as well and have been presented in Figure 34, section 6.1. Comparison of the IPF maps of the as-deposited film and the HAZ lead to the conclusion that the crystallographic characteristics of the as-deposited film are retained in the HAZ around the ex situ melt pool, i.e., a preferred grain orientation of <011> along the film normal but the in-plane distribution of grain orientations is close to random.

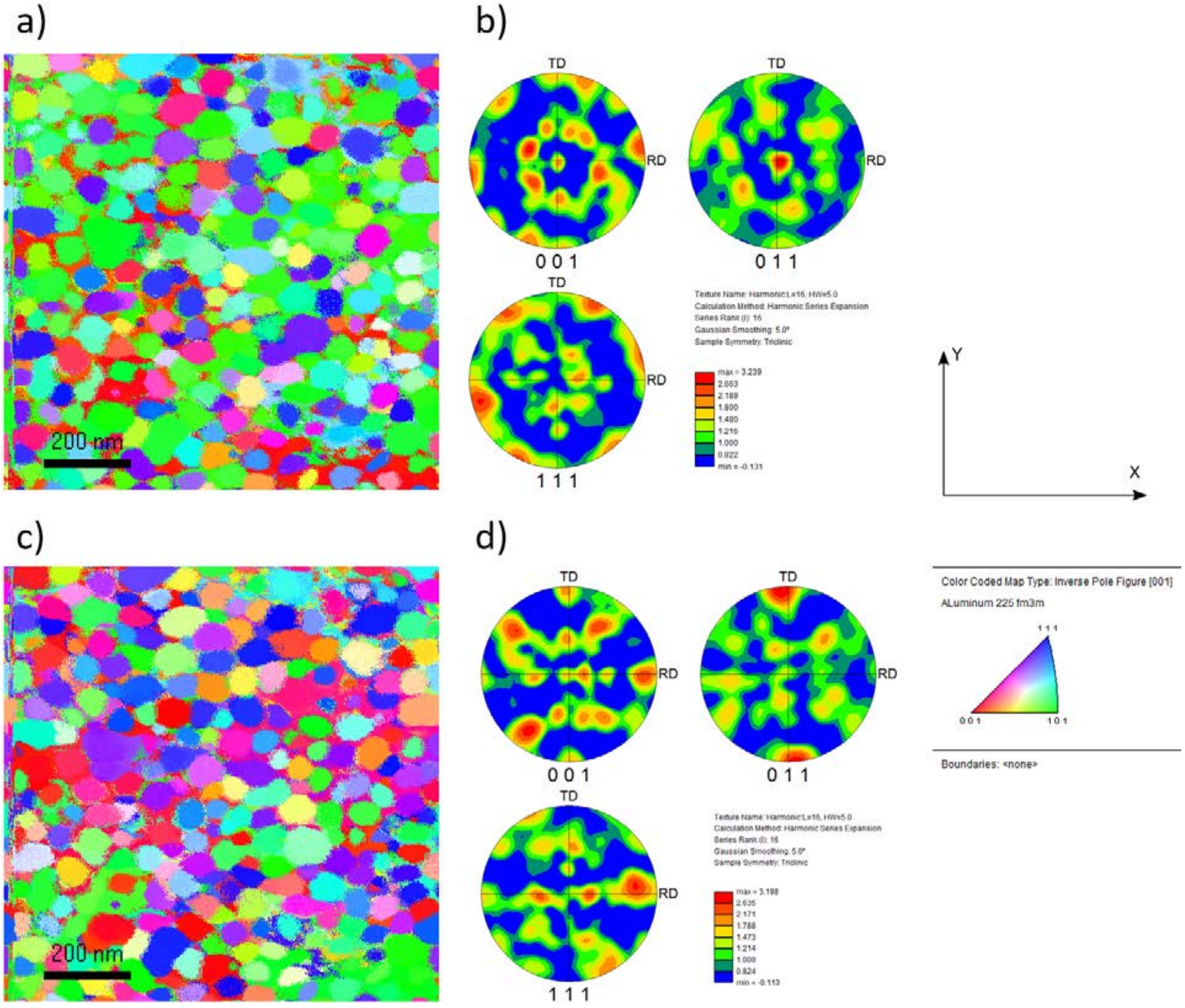

**Figure 53. Color-coded IPF map from PED OIM scan performed in HAZ adjacent to ex situ melt pool. a) IPF map viewed from z (film normal) direction and b) Pole figures corresponding to IPF presented in a). c) IPF map viewed from x (in-plane) direction and d) Pole figures corresponding to IPF presented in b)**

PED OIM scans of largest allowed area and 20 nm step size have then been performed around the centerline region of the ex situ melt pool to collect statistically significant crystallographic information of the favored grains. An example of a set of

OIM scan based IPF maps and corresponding pole figures are displayed in Figure 54 and Figure 55. Figure 54 presents the IPF map viewed from the z-direction (parallel to the film normal) and the corresponding pole figures generated from the IPF map. It is immediately apparent that the scanned area around the centerline is primarily comprsied of grains with <011> direction as their foil normal (represented by green color in the standard triangle). Thus, the preferred orientation along the film normal of the as-deposited film and HAZ remains qualitatively unchanged in the favored grains. However, quantitatively the strength of the <011>-fiber texture, i.e. preference for <011> direction orientation parallel to the thin film normal, increased by approximately a factor of two. Figure 55 a) displays results from the same set of OIM scan data shown in Figure 54 but the color-coded IPF map is based on a view from the x-direction, i.e., the poles parallel to the in-plane solidification direction are plotted in the color-coded orientation map of Figure 54 a). Unlike the random distribution of in-plane directions found in the as-deposited films and HAZ, the in-plane directions exhibit a preference of <001> directions (represented by red color in the standard triangle) and directions close to <001>, as demonstrated by the color-coded IPF map. The associated pole figures and the density of data points in the IPF projected on the standard triangle shown in Figure 55 b), perhaps, more clearly illustrate the considerable preference for a <001>-type growth direction of the columnar morphology grains that are favored for directional growth during the Zone 3 formation of the rapidly solidified microstructure of the Al-11Cu alloy. Considering previous PED OIM scans have shown that the original in-plane crystallographic orientation distribution of the grains in the as-deposited film and HAZ adjacent to the ex situ melt pool are close to random, the preference of solidification direction along the <100> direction is clearly not inherited from the starting microstructure of the film but must have developed during the rapid solidification process in the flat section of the ex situ melt pool after laser irradiation. This preferred <001> growth direction developed during rapid solidification is consistent with the preferred growth direction commonly observed during solidification of cubic metals under conventional solidification conditions, i.e., during cellular dendritic and full dendritic growth. This indicates that crystallographic effects still play an important role during rapid solidification crystal growth at velocities approaching the critical velocity for crystal growth mode transition, here determined as 0.8m/s for the Al-11Cu alloy. The microstructures established during rapid solidification process in hypo-eutectic Al – Cu alloys is influenced by crystallographic aspects of the growth interface of the majority fraction Al solid solution phase.

With the rapidly solidified microstructure in the ex situ melt pool in hypo-eutectic Al – Cu alloy thin films comprehensively evaluated by imaging, spectroscopic and diffraction based TEM and STEM techniques, it can be concluded that the ex situ laser irradiation on the hypo-eutectic Al – Cu alloy thin films enabled formation of melt pool with high aspect ratios. As a result, the curvature dependent heat extraction rate should only change slightly along the flat section of the melt pool edge. At these locations, rapid solidification processes induced by ex situ laser irradiation are qualitatively identical to its in situ counterpart, with the exception that no banded morphology was observed in the rapidly solidified microstructure originated from the flat section of ex situ melt pool. The latter has been attributed to the dimensional restrictions of the ex situ melt pool. Therefore, based on the previous analysis of the in situ experimental observations in section 6.2.1, it is reasonable to conclude that the maximum solidification velocity reached in the columnar morphology grains formed in the ex situ rapid solidification microstructures remained below the critical velocity of 0.8 m/s. Given the overall morphology of the two-phase microstructure of the about 12μm length of the α-cells in the ex situ laser irradiated rapid solidification microstructure of the Al-11Cu it appears reasonable to propose that the favorable grains grew at a maximum velocity approximately have way between the minimum and the maximum, i.e., the average, for the stage II region identified in the velocity plot of Figure 40, namely 0.68m/s or about 0.7m/s. A lowest bound estimate for the velocity of the α-cell growth would be 0.56 m/s, the velocity for the transition from stage I to stage II identified in the velocity plot of Figure 40. At these high crystal growth interface velocities of 0.56 m/s to ~0.7 m/s the interfacial crystallography still affects the rapid solidification behavior and resultant microstructure evolution. However, if there is a significant difference in the local heat extraction rates present, the difference in heat extraction can override the crystallographic effects and rapid solidification processes can be dominated by the preferred heat transport effect, as demonstrated by the rapidly solidified microstructure in the in situ melt pools.

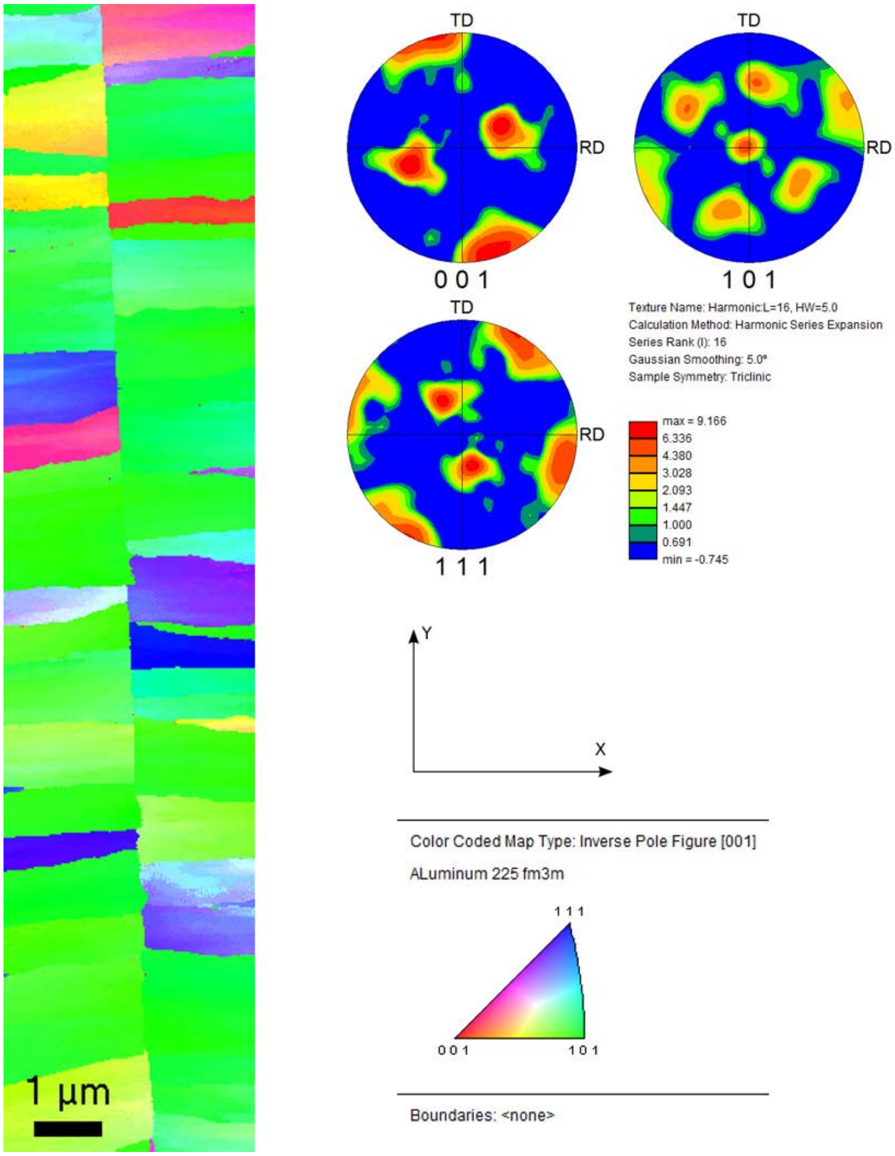

**Figure 54. Color-coded IPF map and associated pole figures from PED OIM scan performed in the centerline region of ex situ melt pool viewed from z (film normal) direction**

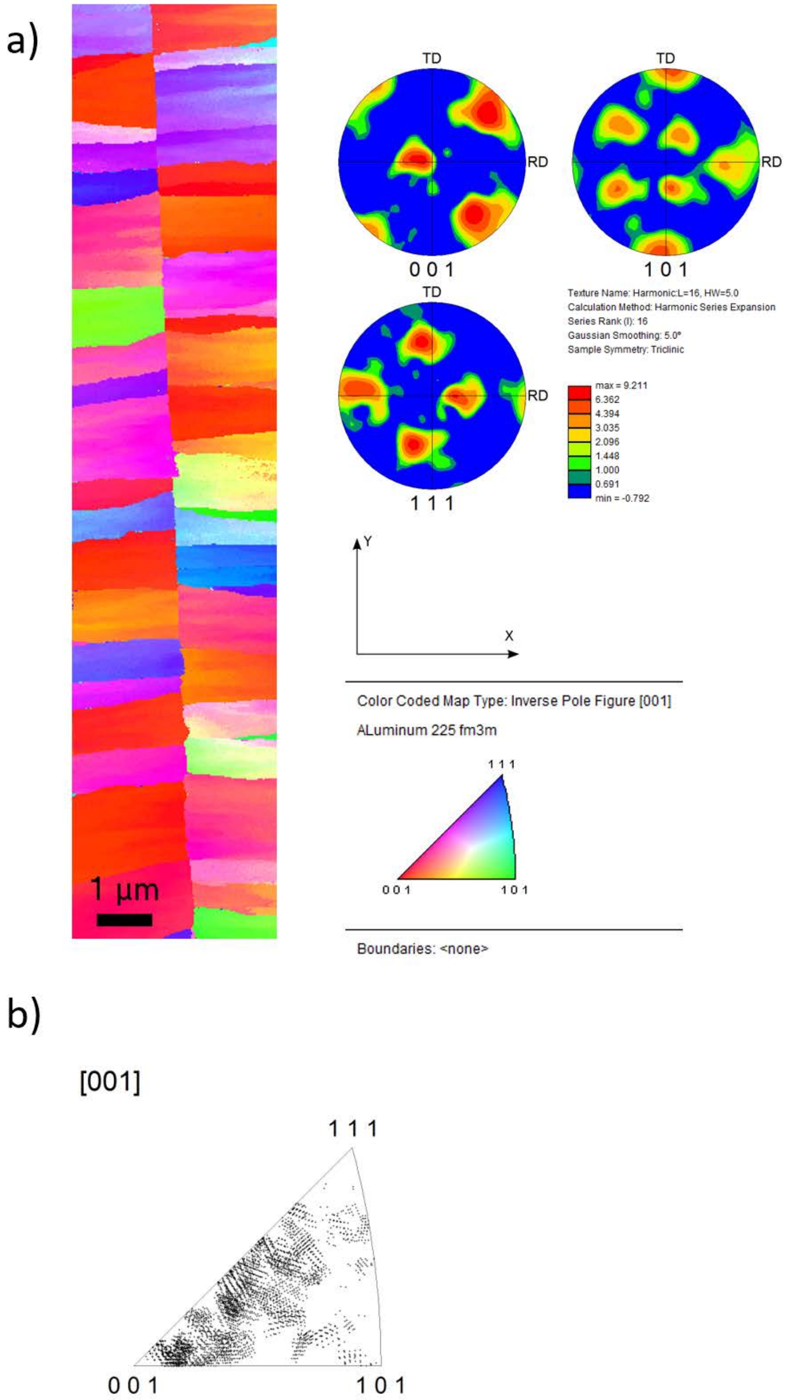

**Figure 55. a) Color coded IPF map and associated pole figures from PED OIM scan performed in the centerline region of ex situ melt pool viewed from x (in-plane) direction and b) IPF map projected on the standard triangle**

## 6.4 SUMMARY

Rapid solidification induced by in situ pulsed laser irradiation and ex situ pulsed laser irradiation in nanocrystalline hypo-eutectic Al – Cu alloy thin films have been investigated. The solidification behavior, velocity evolution during rapid solidification process, influence of increased Cu content on the solidification behavior and resultant microstructure and effect of crystallography on the rapid solidification process in hypo-eutectic Al – Cu alloy thin films have been examined and quantified.

In situ MM-DTEM observations showed that the incubation time for rapid solidification process in hypo-eutectic Al – 11Cu alloy thin films is ~ 25 μs and the solidification interface accelerated during the entire solidification process. Velocity evolution during the rapid solidification process has been determined with high accuracy (~ 6% uncertainty) based on DTEM experiments and the critical velocity for change of crystal growth mode to occur is 0.8 ± 0.05 m/s. Results from current study combined with prior work [28,114] on the rapid solidification in Al – 4Cu alloy thin films suggest lower critical velocities than that predicted by previously proposed SMSM of Al – Cu alloys [35].

Post-mortem characterization of rapidly solidified microstructure in the in situ melt pool revealed the influence of increased Cu concentration on the rapid solidification process in hypo-eutectic Al – Cu alloy thin films. Higher Cu content lead to longer incubation time, a wider transition zone of ~ 750 nm at the edge of the melt pool and formation of dendrite-like microstructure in the transition zone. STEM-EDS mapping demonstrated that variation of Cu concentration at nano-scale was present in the liquid during rapid solidification and this variation was frozen into the partitionless region in the banded microstructure and retained after solidification completed.

Ex situ laser irradiation provided a venue for modification of heat extraction geometry during rapid solidification process. Although the laser profile and heat extraction geometry are different in the ex situ experiments, upon scrutiny of the rapidly solidified microstructure in the ex situ melt pool, it can be concluded that the rapid solidification process induced by ex situ laser irradiation is comparable to the in situ process. Combining the results from PED OIM scans of the ex situ melt pool and in situ experiments, a conclusion that crystallography still affects the rapid solidification behavior and hence resultant microstructure when solidification velocities are lower than 0.8 m/s can be drawn.

# 7.0 RAPID SOLIDIFICATION OF HYPER-EUTECTIC ALUMINUM – COPPER THIN FILMS

As mentioned in section 3.3, the hyper eutectic Al-Cu part of the current SMSM is rather incomplete due to critical challenges arising from sample crack during the thermal cycles of the laser surface melting process, which has been attributed to the formation of relatively more brittle θ-$Al_2Cu$ phase as the primary phase. This chapter presents results from the first investigation by in situ DTEM experimentation combined with post-mortem characterization on the rapid solidification process in the hyper-eutectic Al – Cu thin films. Cracking of these thin-film alloy samples was not observed during the in situ experiments, demonstrating the feasibility of the thin film geometry and DTEM experiments for investigating rapid solidification process in hyper-eutectic Al – Cu alloys to complement the current SMSM of Al – Cu alloys. It is the author's hope that these initial results can serve as a stimulus as well as guidance for continued exploration on the rapid solidification behavior in hyper-eutectic Al – Cu alloys and other otherwise challenging multicomponent material systems of interest.

## 7.1 AS-DEPOSITED HYPER-EUTECTIC ALUMINUM – COPPER THIN FILMS

The microstructure characteristics of the as-deposited hyper-eutectic Al – Cu alloys were investigated using conventional transmission electron microscopy and the results are presented in Figure 56. Figure 56 (a) displays an example BF TEM image of the as-deposited hyper-eutectic Al-Cu alloy thin film prior to solidification experimentation, showing that the initial state of the film is continuous with nanocrystalline grains. Figure 56 (b) shows a typical DF TEM image of the hyper-eutectic Al-Cu thin film, showing the film is indeed constituted of nanocrsystalline grains with an average grain size of ~ 40 nm. A SADP taken from the as-deposited film is presented in Figure 56 (c). In the example SADP, the first two diffraction rings can be indexed as $\{110\}_{\theta}$ and $\{200\}_{\theta}$, respectively, and the third diffraction ring correspond to $\{111\}_{\alpha\text{-Al}}$. Although not all the diffraction rings are labeled in Figure 56 (c), all diffraction peaks can be indexed as either α-Al or θ-$Al_2Cu$ phases, indicating the alloy thin film is comprised of α-Al and θ-$Al_2Cu$ phase.

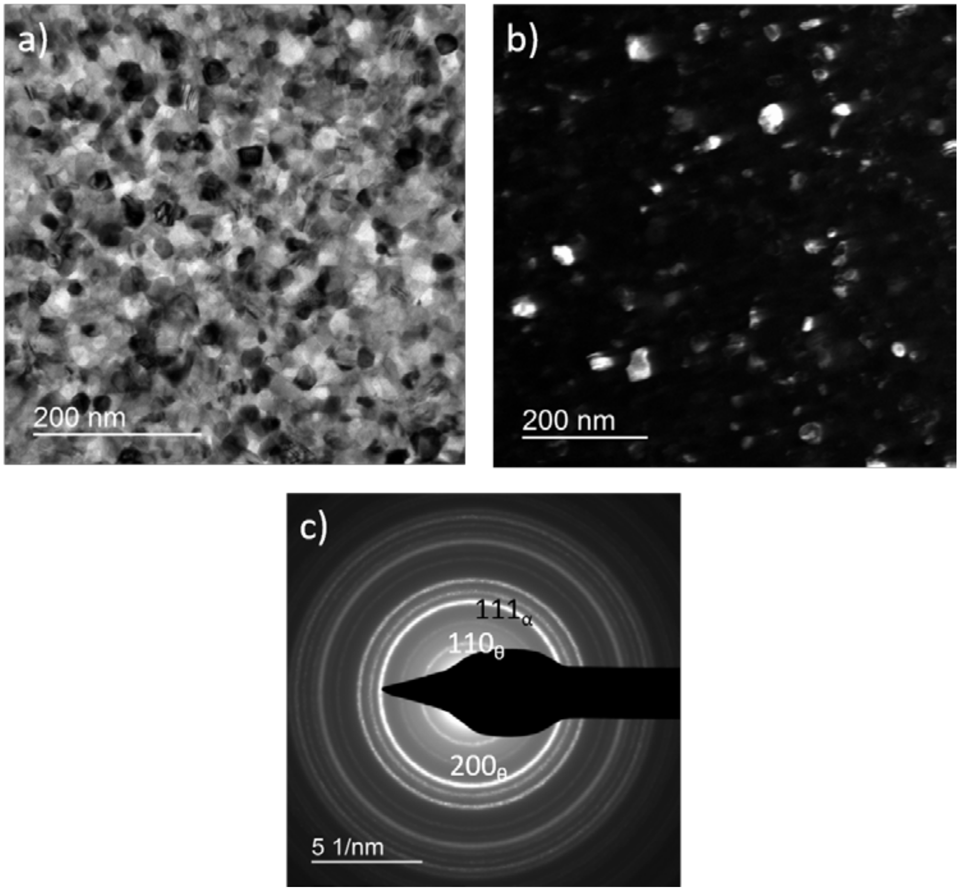

**Figure 56. a) A BF TEM image of the as-deposited hyper-eutectic Al-Cu thin film. c) Typical DF TEM image of the hyper-eutectic Al-Cu thin film showing the nanocrystalline grain size. c) Example SADP of the as-deposited hyper-eutectic Al-Cu thin film with the first three diffraction rings indexed.**

Compositional analysis of the as-deposited hyper-eutectic Al – Cu thin films using HAADF STEM imaging accompanied with STEM-EDS measurements and mapping have also been performed. An example of the results is shown in Figure 57. HAADF image of the examined area is shown in Figure 57 a), with Cu-rich regions appear brighter and Cu-depleted regions appear darker. Figure 57 b) presents color-coded Cu concentration map based on STEM-EDS mapping of area shown in Figure 57 a), with redder color representing higher concentration level of Cu, showing excellent contrast correlation between the relatively Cu-rich (bright, green-red) areas and Cu-depleted (darker, blue) areas in Figure 57 a) and b). Quantitative STEM-EDS measurements of certain areas and also the average composition of the thin film have been conducted. The locations of such measurements are indicated in Figure 57 a) and b) using green rectangle (#1, view) and green circles (#2 - #12) and the measurement results in terms of atomic percent of Cu are arranged in Table 11. The average composition of the Cu-rich regions is Al – 33.68 at.% Cu, which corresponds within the measurement uncertainty to the equilibrium composition of θ-$Al_2Cu$ phase and the average composition of Cu-depleted areas is Al – 3.3 at.% Cu. By averaging EDS measurements from several large area scans, the composition of the hypo-eutectic as-deposited film is determined to be Al – 18.5 at.% Cu. The denser distribution of Cu-rich regions when compared to the results from STEM-EDS measurement performed on the Al – 11 at.% Cu thin films presented in Figure 33 is expected as the primary phase of hyper-eutectic Al – Cu thin films should be θ-$Al_2Cu$ phase.

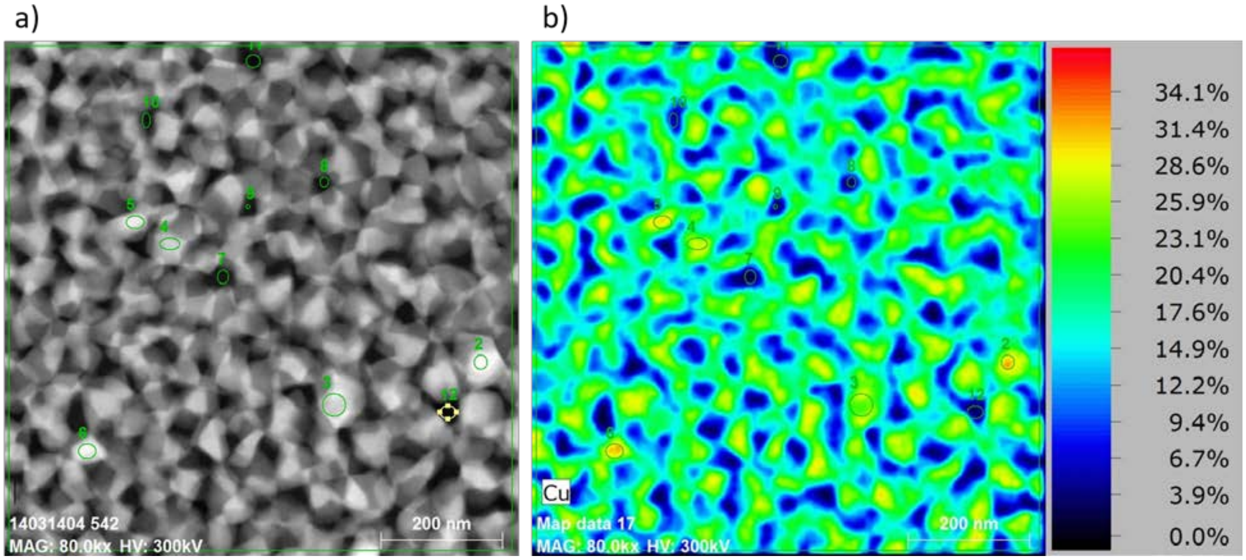

**Figure 57. a) HAADF image of the as-deposited hyper-eutectic Al-Cu thin film with green rectangle and circles indicating location for EDS measurements. b) Color-coded EDS mapping of Cu concentration levels**

**Table 11. EDS measurements results in Figure 57 in terms of atomic percent of Cu**

| **Location** | **at.% Cu** | **Location** | **at.% Cu** |
|---|---|---|---|
| **1 (view)** | 20.16 | **7** | 2.77 |
| **2** | 35.33 | **8** | 3.59 |
| **3** | 29.41 | **9** | 3.23 |
| **4** | 31.85 | **10** | 5.54 |
| **5** | 36.05 | **11** | 3.41 |
| **6** | 35.76 | **12** | 3.62 |

## 7.2 RAPID SOLIDIFICATION OF HYPER-EUTECTIC ALUMINUM – COPPER THIN FILMS BY IN SITU LASER IRRADAITION

In situ MM-DTEM experimentation has been performed on the hyper-eutectic Al – 18.5 at.% Cu (referred as Al – 18.5Cu from here on for brevity) thin films to record in situ pulsed laser irradiation induced rapid solidification processes. Results from a set of time-resolved low-magnification MM-DTEM imaging series are presented in Figure 58. Full documentation of the entire melting and re-solidification process of Al – 18.5Cu alloy thin films required acquisition of seven low magnification MM-DTEM sequences with nine frames per sequence of 2.5 μs inter-frame time and 50 ns image formation electron pulse at different time delays that span from t = 0 μs to t = 120 μs (Figure 58). The MM-DTEM sequences are presented in chronological order in Figure 58. Each of the seven rows of MM-DTEM image sequences corresponds to one specific time-delay sequence of nine images recorded over a duration of 20.45 μs during the rapid solidification of Al – 18.5Cu from a separate laser pulse irradiation in situ TEM experiment. The seven different MM-DTEM experiments have been performed with initial delay times of 0, 20, 40, 60, 80, 100 and 120 μs after the transformation initiating laser pulse, as indicated under the first image of each row in Figure 58. The time stamp under the last image of each row indicates the end time of the corresponding image sequence, with a normal BF TEM image taken after each solidification experiment to show the overview of the solidified in situ melt pool and labeled as “After” in Figure 58.

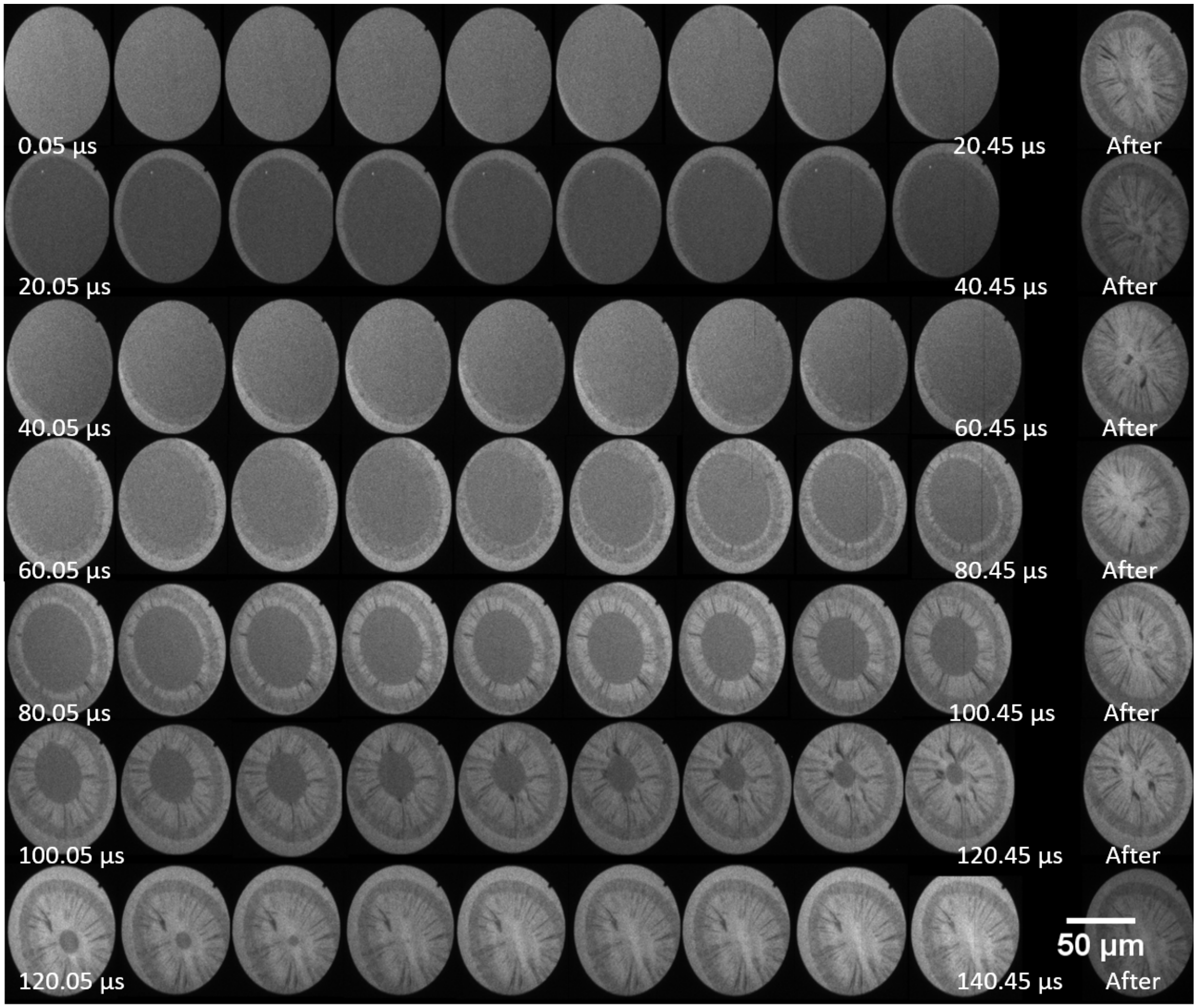

**Figure 58. Low-magnification MM-DTEM image sequences of images recorded during rapid solidification in hyper-eutectic Al – 18.5Cu alloy thin film after pulsed-laser irradiation. The indicated times below the first and last images are the time intervals between the peak of the Gaussian laser pulse and the 50 ns duration image formation electron pulse. The time interval between images in each frame is 2.5 μs.**

The converted radius method that was used to determine the evolution of the melt pool for pure Al and hypo-eutectic Al – Cu alloy (see sections 5.3.1 and 6.2.1) has also been applied here. Thus, the temporal evolution of the in situ melt pool has been quantified by tracking and measuring its dimension recorded in the low-magnification MM-DTEM image sequences. The length of the semi-major and semi-minor axes of the elliptical melt pool were measured by fitting an ellipse to the melt pool in the ImageJ software [102] and the geometric mean of the two measured lengths is defined as the converted radius. Based on the MM-DTEM observations displayed in Figure 58, the measured melt pool dimensions begin to decrease monotonically at t = 22.6 μs after the delivery of sample drive laser irradiation pulse and the last measurable remaining liquid was observed at $t_{img}$ = 125.15 μs (second image of the last sequence in Figure 58). Therefore, t = 22.6 μs is treated as the onset of rapid solidification processes and t = 125.15 μs is considered as the terminus of the rapid solidification process.

In principle, the melt pool dimension documented in the last image of one sequence and the melt pool dimension documented in the first image of the subsequent sequence should have been very similar, if not the same. However, with the number of sequences required to document the rapid solidification process in hyper-eutectic Al – Cu thin films, it is inherently challenging to maintain the exact same energy in each sample-drive laser pulse for each of the seven sequences. As a result, deviations in the size of the melt-pool in the first image frame of each series relative to that in the last frame of the preceding series range from 0.5% to 8% between the two sets of melt pool dimension documented otherwise at similar time points. In order to address this inherent uncertainty, for the two overlapping time frames, $t_{img}$ = 40.45 μs and $t_{img}$ = 40.05 μs, for example, an average value was taken from the measured major and minor axes at the two different time points and treated as the melt pool dimension at an averaged time, e.g., 40.25 μs, the average of 40.45 μs and 40.05 μs. The evolution of the converted radius of the in situ melt pools in hyper-eutectic Al – Cu thin films after the aforementioned data processing and adjustments is shown in Figure 59.

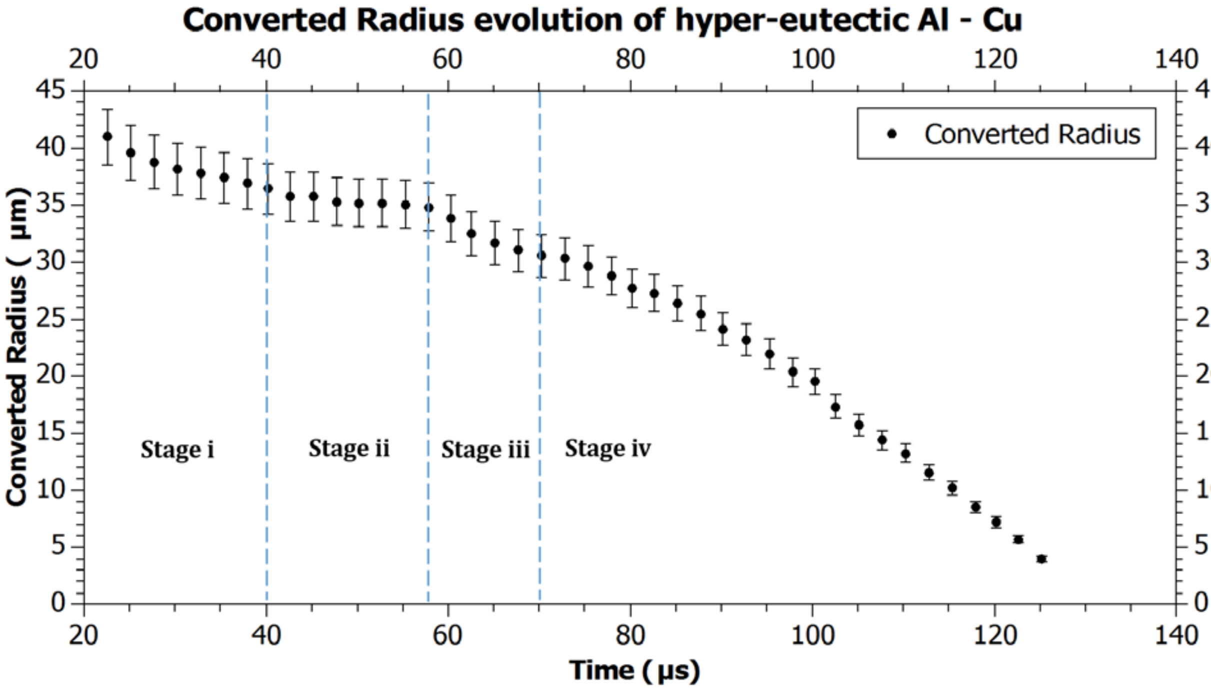

**Figure 59. Converted radius evolution of the in situ laser irradiation induced melt pool in hyper-eutectic Al - Cu alloy thin film with different stages illustrated**

Unlike the rapid solidification process in pure Al and hypo-eutectic Al – Cu thin films, during which the solidification interfaces were always accelerating, the evolution of converted radius during the rapid solidification process in hyper-eutectic Al – Cu thin films indicates that the liquid-solid interface was not consistently and monotonically accelerating (as shown in Figure 59). Instead, melt pool dimension changes, represented by the converted radius metric evolution, exhibited rather complex behavior for the different stages throughout the entire solidification process. After carefully performing repeated measurements, consistently reproduced the unexpected evolution trend for the converted radius in hyper-eutectic Al – Cu thin films. This behavior therefore does not appear to represent an irreproducible artifact. The apparent decelerations of the solidification interface in Stage i and Stage ii marked in Figure 59 during the rapid solidification process of the hyper-eutectic Al-18.5Cu alloy represent characteristic behaviors. Therefore, instead of using a continuous fitting function to represented the velocity evolution during the entire solidification process in a closed algebraic form, the rapid solidification process in hyper-eutectic Al – Cu thin films has been analyzed by separation into the four distinct stages illustrated in Figure 59 , which are based on the changes in the rates of melt pool dimension decrease during the rapid solidification process. The four stages are described separately as follows:

Stage i: Initial stage.

After 22.6 µs of incubation time, the converted radius decreased noticeably from 41.02 µm to 36.44 µm during 22.6 µs to 40.25 µs, with an average velocity of ~ 0.26 m/s. Judging from the convex trend of the converted radius, the interface was actually decelerating during this stage. This implies that the initial velocity of the interface must be higher than 0.26 m/s. Since the solidification interface that grows the crystal into the liquid alloy of the shrinking melt pool has to start from a stationary initial state with trivial velocity, $v_{t\leq 22\mu s} = 0$ m/s, an initial very rapid acceleration of the interface to a velocity larger than about 0.26 m/s has to be postulated and was not captured in the low-magnification MM-DTEM sequences to date. This initial rapid acceleration, potentially due to the large initial thermal gradient, while not captured here, would then mark the onset of the directional crystal growth behavior of the rapid solidification process. Assuming a constant deceleration in this Stage i regime of rapid solidification in the hyper-eutectic Al-18.5Cu, the average solidification velocity evolution during stage i can be deduced from the converted radius evolution and is displayed in Figure 60 (marked as stage i by dashed lines). The initial velocity at time t=22.6μs can be estimated to be limited to $v_{t=22.6\mu s} \approx 0.43$ m/s and decelerates to a velocity no larger than $v_{40.25\mu s} = 0.10$ m/s at the terminus and transition to Stage ii.

Stage ii: Stagnation stage.

The converted radius decreased very slowly from 36.44 µm to 34.83 µm during the time interval between t=40.25 µs to t=57.9 µs. This represents an average velocity of ~ 0.09 m/s for the solidification interface for the duration of 17.65 µs of Stage ii. The slow migration rate is clearly reflected in the MM-DTEM observations. The combined time frame of Stage i and Stage ii corresponds to the processes for formation and development of the “dark grey ring” observed in sequence #2 (20.05 µs to 40.45 µs) and in the majority part of sequence #3 (40.05 µs to 60.45 µs) in Figure 58. The development of the “dark grey ring” in sequence #2 is still distinguishable while the change of the ring is minimal and hardly discernible in sequence #3. Therefore, this stage is termed as the stagnation stage, during which quite slow crystal growth has been observed to facilitate formation of the “dark grey ring” feature characteristically present in the rapid solidification microstructure of the Al-18.5Cu alloy. This stage is presented in Figure 60 and marked as stage ii, showing a relatively low velocity of ~ 0.09 m/s. As a reminder to the reader, a crystal growth rate on the order of cm/s still represents very fast solidification under conditions significantly far from equilibrium.

Stage iii: Transition stage.

During this stage, the converted radius decreased considerably again from 57.9 μs to 72.8 μs, with the length of converted radius decreasing from 34.83 μm to 30.31 μm at an average velocity of ~ 0.30 m/s. This stage is documented in the last two frames of sequence #3 (40.05 μs to 60.45 μs) and first six frames of sequence #3 (60.05 μs to 80.45 μs) in Figure 58. Upon examining the MM-DTEM frames, the solidifying Al – Cu alloy started to exhibit light grey contrast that is clearly different from the “dark grey ring” at $t_{img}$ = 70.25 μs, implying a potential change of the crystal growth mode and resultant microstructure at t $\approx$ 70 μs. Therefore, this stage is termed as the transition stage, representing the end of the growth of the “dark grey ring” region and initiation of a new crystal growth mode. This stage is distinguished from the subsequent stage, Stage iv, because the rate of reduction of the converted radius during the time interval of Stage iii shows a mildly convex or linear trend, as displayed in Figure 58. Considering the actual measured values of the converted radius a mildly convex trend exists for the Stage iii interval. However, also taking into account the uncertainty ranges for this series of measurements, a linear trend, i.e., a constant rather than mildly decreasing (slowing) rate for the reduction of the converted radius, would also provide a reasonable description. This implies either a mildly slowing or a constant velocity for the solidification interface in stage iii during the rapid solidification of the Al-18.5Cu hypereutectic alloy. In the low-magnification MM-DTEM sequences, contrast change in the solidifying melt pool is clearly evident. This contrast change likely corresponds to a change in the morphology of the associated solidification microstructure and probably signals a change in the dominant crystal growth mode. So, a transition in the growth mode processes should have to occur, but it is challenging to determine the exact starting and end time for this transition stage based on the MM-DTEM data sets currently available. Further DTEM experimentation on thin films with similar composition and other compositions in the hyper-eutectic Al – Cu regime would be indicated and needed to collect more data sets and in formation in order to draw more concrete conclusions regarding whether a distinct transition stage is truly present and to determine more accurately its duration and the velocity evolution associated with this stage. Based on the current data and within the error bars of the sets of radii measured for the time interval of about 58μs to 73μs after delivery of the laser irradiation pulse, this stage is depicted in Figure 60 with the solidification interface maintains a finite and constant velocity of about 0.3m/s.

Stage iv: Rapid growth stage

After the transition stage, the converted radius evolution with time develops a stable concave-shaped trend, which resembles qualitatively the behavior of the converted radius evolution during the rapid solidification of pure Al and hypo-eutectic Al – Cu alloy thin films. This concave topology in the radius versus time plot therefore indicates an uninterrupted accelerating solidification interface. From 72.8 μs to 125.15 μs, the length of converted radius decreased from 30.31 μm to 3.95 μm with an average velocity of ~ 0.5 m/s. As shown as stage iv in Figure 60, the initial and terminal velocity values for the rapid growth stage, Stage iv, were 0.30 m/s and 0.70m/s, respectively. This stage corresponds to the growth of solidifying microstructure exhibiting the light grey contrast in the MM-DTEM image sequences in Figure 58 and exhibited the highest average solidification velocity among all four stages.

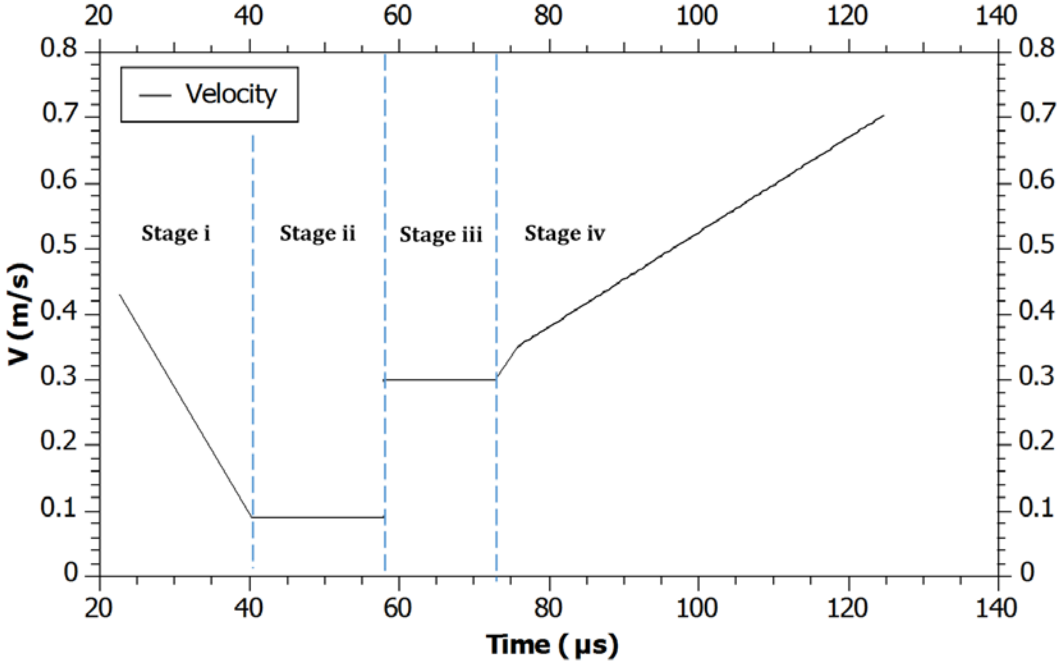

**Figure 60. Schematic illustration of the average velocity evolution in stage i to stage iv during the RS process of Al-18.5Cu**

It can be seen in Figure 60 that the velocity transition from stage ii to stage iii behaved discontinuously and this can be attributed to the relatively low temporal resolution of the low-magnification MM-DTEM experimentation. In the attempt to resolve the transition between different stages by collecting more data points with higher temporal resolution, some select MM-DTEM experiments with high spatio-temporal resolution (typically 500 ns inter-frame time and 1200X – 1500X magnification with the field of view of an approximate diameter of ~ 12 µm) have also been conducted for specific time delays for the Al – 18.5Cu alloy thin films, with the aim of capturing more detailed information of the transition between the different stages associated with the rapid solidification process as reflected by the characteristic discontinuities in the temporal evolution of the converted radius and the average solidification velocity (Figure 59 and Figure 60). Figure 61 presents three images extracted from one of the high spatio-temporal resolution image sequences, with initial time delay of 120 µs, at t = 120.6 µs, 122.25 µs and 123.9 µs, respectively, after the laser irradiation pulse delivery. The "After" image was taken minutes after the solidification process completed.

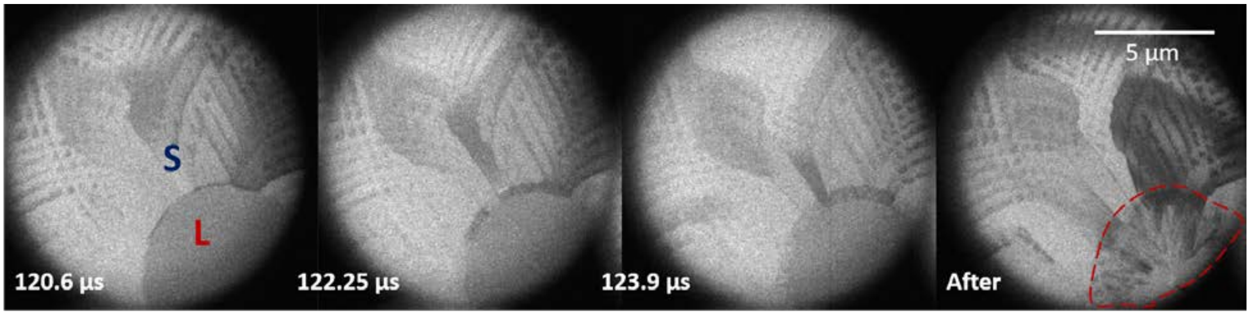

**Figure 61. Images extracted from one high spatio-temporal resolution MM-DTEM image sequence with an initial time delay of 120 µs. Unexpected feature is highlighted by dashed line in the "After image"**

It was expected that a high spatio-temporal resolution DTEM experiment with an initial time delay of 120 μs could capture the evolution of melt pool just before solidification completes in the Al – 18.5Cu alloy thin film. However, surprisingly, the melt interface (i.e., in Figure 61, delineating the darker grey melt, labeled as L, from the crystal newly formed, labeled with S) only migrated very little as shown in the three images in Figure 61 between 120.6 μs and 123.9 μs. This is contrary to the rapid shrinkage of melt pool after 120 μs observed in the low spatio-temporal resolution MM-DTEM image sequences (Figure 58). Based on the MM-DTEM image sequence of Figure 58, performed for fields of view large enough to encompass the entire melt-pool, an anticipated completion of solidification at slightly later than 125.15 μs can be estimated. This is inconsistent with the dynamics of the rapid solidification events recorded in the high-magnification MM-DTEM sequence in Figure 61. In addition, an unexpected feature that has not been observed in the after images of rapid solidification process in pure Al thin films or hypo-eutectic Al – Cu thin films before is evident in the after image presented in Figure 61 and has been highlighted by a red dashed line.

In order to understand the unique feature in the center of the microstructure of the rapidly solidified Al-18.5Cu after performing the high spatio-temporal MM-DTEM experimentation and to correlate the different stages of the solidification front velocity reflected by the converted radius evolution with the respective microstructure formed during RS process of hyper-eutectic Al – Cu thin films, post-mortem characterization of has been performed.  An example of representative the results is shown in Figure 62. Figure 62 a) presents a montage of BF TEM images to give an overview of the in situ melt pool. The individual BF TEM images of Figure 62 b), c) and d) depict enlarged views for select regions of the solidification microstructure to provide a clearer illustration of the morphology and scale of the microstructural features of the corresponding regions. Four morphologically distinct zones and a central feature can be observed, which are marked by yellow number labels 1, 2, 3, and 4, respectively, in Figure 62. Zone 1, the heat affected zone (HAZ), is equivalent to the HAZ also commonly observed around all in situ melt pools of the pure Al and the hypo-eutectic Al – Cu thin film samples (e.g. compare to Figures Figure 31 and Figure 46). Zone 2 exhibits characteristics of a typical eutectic growth morphology (Figure 62 b)). Based on the evident dark grey contrast displayed in the montage of the BF images and Figure 62 b), the microstructure of zone 2 can be correlated with the solidification interface velocity regimes to previously defined with reference to Figure 59 as stage i, the initial stage, and stage ii, the stagnation stage. During these first two stages of directional crystal growth of the rapid solidification process, the formation and development of a "dark grey ring" region was observed (Figure 58). A boundary between zone 2 and zone 3 can be observed due to the contrast difference and clearly distinct microstructure morphology. This morphological change of the solidification microstructure exhibited in zone 2 to that of zone 3 should correspond to the transition stage, Stage iii in Figure 59. However, as mentioned previously, more experiments are required to evaluate and confirm the presence and details of the transition stage. Zone 3 exhibits an apparent directional growth morphology consisted of columnar grains and zone 4, a banded morphology, is clearly demonstrated in Figure 62 c), as the columnar grains approaching the center of the in situ melt pool. The unexpected central feature that has not been observed in MM-DTEM experiments performed at the lower spatio-temporal resolution (e.g. Figure 58) is shown in Figure 62 d). After examining several BF TEM images of this feature in different in situ melt pools that have been established during higher spatio-temporal resolution MM-DTEM in situ experiments (not all presented here), it was found that the central feature exhibits microstructural morphology that closely resembles the characteristics of an in situ melt pool, with eutectic-type microstructure growing from the perimeter of this feature, followed by columnar grains originating from the eutectic-type microstructure and eventually meeting at the center of this feature. It therefore appears reasonable to conclude that the central feature was formed by solidification and directional crystal growth radially inward from its clearly discernible boundary to its center (Figure 62 c) and d)). The processes associated with the formation of this solidification microstructure therefore would be equivalent to those active during rapid solidification observed in the low-resolution MM-DTEM image sequences (e.g. Figure 58). An alternative hypothesis would be the nucleation and rapid growth from the supporting nitride substrate layer. However, if the formation of the central feature was induced by nucleation in the evolving melt pool or from the substrate that is similar to what has been observed in other experiments (see section 3.4), the origin of the columnar grains should appear to be from the center without formation of eutectic-type microstructure along the perimeter of it. In addition, the nearly elliptical shape of the central feature is also suggesting it was grown from the perimeter instead of from the center of the melt pool as nucleation induced growth is typically less controlled and should exhibit a more irregular shape [69,116]. EDS measurements performed on the columnar grains of the central feature provides an average composition of 18.36 at.% Cu, which is essentially the same as the film composition. Therefore, the hypothetical scenario for the central feature formation involving nucleation in the liquid or from the substrate and subsequent growth can be dismissed.

Instead, the formation of the unique central feature observed in the high-magnification MM-DTEM experiments for the Al-18.5Cu alloy is likely related to the heating effects of the electron irradiation pulse incident on the small field of view over the 50 ns duration time interval utilized for the formation of the individual images in the MM-DTEM sequences (e.g. Figure 61). Notably, comparing Figure 61 and Figure 62 c), the size of the field of view illuminated by the electron pulses in the MM-DTEM series shown in Figure 61 (diameter ≈12 µm) is slightly larger than the major axis of ~ 9 µm of the unexpected elliptical central feature. With quite localized illumination of the image formation pulse at higher magnifications, the significant energy density of the image formation pulse could be sufficiently high to heat up the imaged area. Thus, introducing a change of thermal gradient and extra amount of heat that needs to be dissipated for solidification processes to proceed. Towards the end of the solidification process at long times after the laser pulse induced melting, the thermal profile in the remaining liquid has become quite flat with very small amount of superheat remaining. This can be concluded based upon the thermal profile temporal evolution calculations performed for the Al thin film rapid solidification presented in chapter 5.0 of the current document. Hence, even the relatively short 50ns duration 200kV electron pulse used for image formation in the

MM-DTEM experiments would induce an increase in the temperature of the melt and the solid adjacent to the migrating solid-liquid interface in the field of view. Furthermore, the liquid state has a lower reflectivity for the electrons than the crystalline state of the alloy. Therefore, in the vicinity of the liquid-solid interface the liquid would heat up more than the solid, resulting in an increased magnitude of the positive thermal gradient in the liquid due to a heating effect from the pulsed electron beam illumination. This would establish conditions to slow down or stop the solidification front. As a result, the process of rapid solidification crystal growth would have to initiate anew at the stagnant melt pool perimeter established by the electron pulse heating effect and the velocity dependent growth mode would revert back to regular eutectic growth mode that correspond to lower solidification velocities to form the eutectic-type morphology along the perimeter of the melt pool. After the thermal conditions are balanced again, directional columnar growth is re-initiated from the perimeter again. Eventually, the columnar grains met at the center of the melt pool and a microstructural set of features consistent with the re-solidification of a smaller secondary melt pool formed. Considering the hyper-eutectic Al – 18.5Cu alloy have lower melting point than pure Al or hypo-eutectic Al – 11Cu alloys, it is reasonable to expect that the Al – 18.5Cu thin films and associated RS processes are more susceptible to significant modification by small temperature excursions from electron beam pulse induced heat than would be the case in pure Al or Al – 11Cu alloy thin films. Hence, the unexpected features have not been observed for the latter systems. This scenario would be consistent with the morphology of the microstructure and the scale of the unexpected feature observed in the high-magnification MM-DTEM experiments at long delay times after the initial laser pulse melting event for the Al-18.5Cu hyper-eutectic alloy thin films. It is evident that the formation of secondary melt pool induced by the pulsed electron beam illumination heating effect hampers effective high spatio-temporal DTEM observation, suggesting adjustment of parameters of the imaging pulse for high spatio-temporal DTEM, such as the laser energy, inter-frame time spacing or laser profile, is necessary in future high-magnification DTEM experiments to obtain meaningful MM-DTEM image sequences with high spatio-temporal resolution in hyper-eutectic Al – Cu alloy systems or other material systems with relatively low melting point and during stages of the solidification processes that involve relatively flat thermal gradients adjacent to the migrating transformation interface.

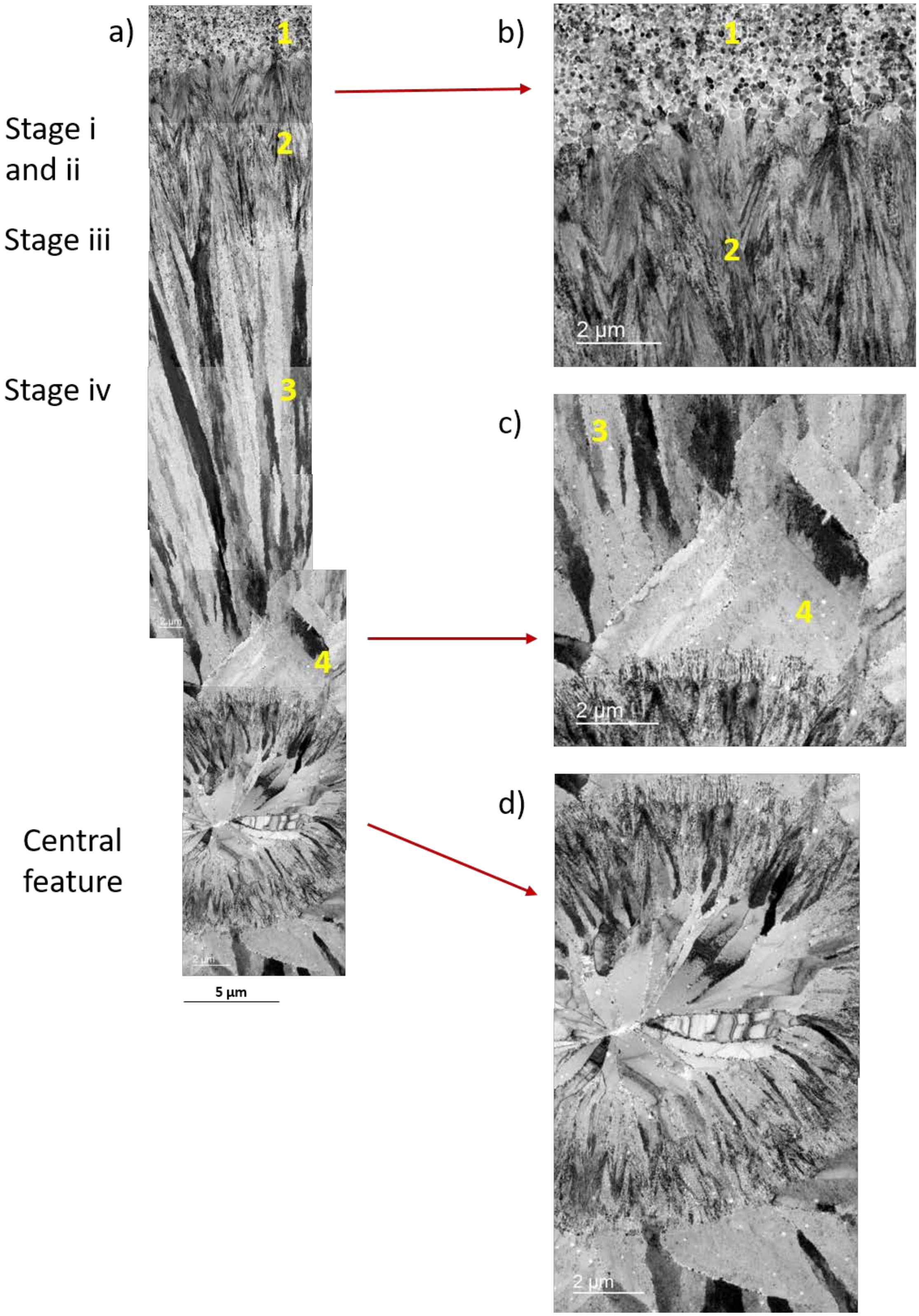

**Figure 62. Montage of BF TEM images and enlarged individual BF TEM images of the in situ melt pool in Al – 18.5Cu thin film**

Figure 63 presents more detailed BF TEM images and corresponding SADP in the eutectic growth zone (Figure 63 a)) and columnar growth zone (Figure 63 b)), with yellow circles indicating where the respective SADP was taken. The strong diffraction spots in SADP shown in top right corner of Figure 63 a) correspond to a Al [111] zone axis and strong diffraction spots in SADP shown in top right corner of Figure 63 b) demonstrates a Al [110] zone axis pattern. The average compositions measured in the eutectic growth zone and columnar growth zone are Al – 17.88 at.% Cu and Al – 17.64 at.% Cu, respectively. These values are both very close to the eutectic composition of Al – 17.3 at.% Cu in the Al – Cu alloy system. The SADP and composition measurements for this region of the rapid solidification microstructure indicate that the eutectic growth zone is constituted of $\alpha + \theta$ eutectics and that the majority phase, the matrix of the subsequently forming columnar grains are supersaturated α-Al cells with the film composition frozen into solid.

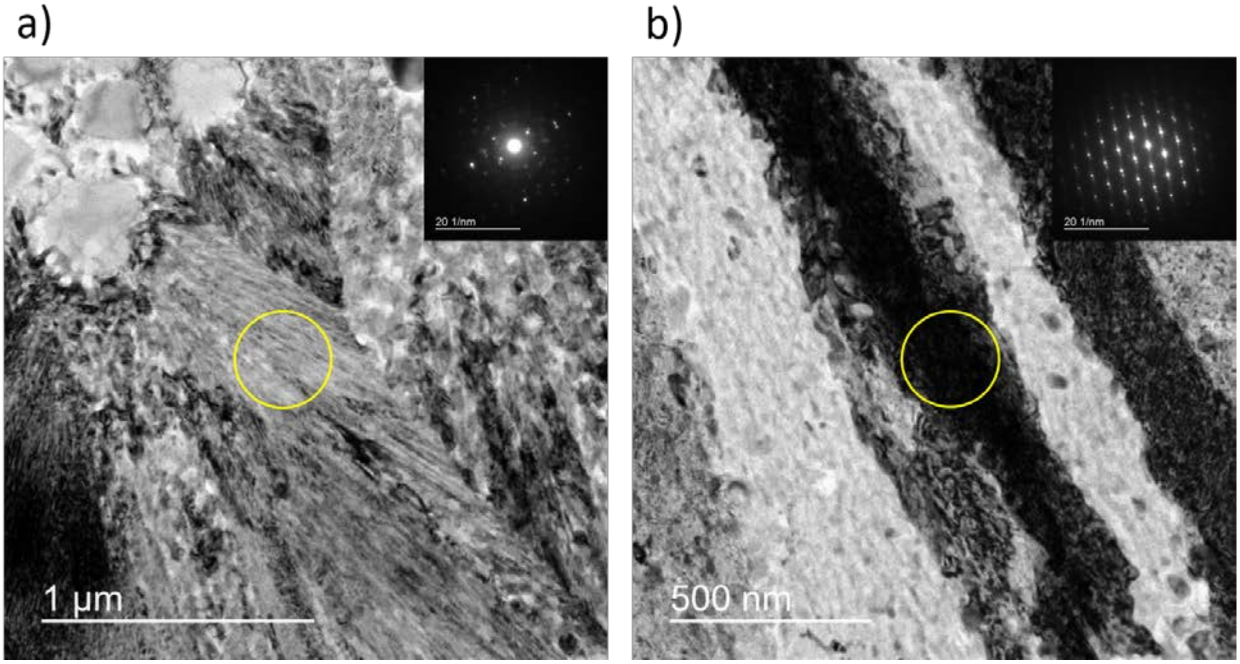

**Figure 63. a) BF TEM image of the eutectic growth region and corresponding SADP (top right corner) taken from the area indicated by the yellow circle. b) BF TEM image of a columnar grain and corresponding SADP (top right corner) taken from the area indicated by the yellow circle.**

The development of the morphological zones observed in the in situ melt pools of hyper-eutectic Al – 18.5Cu (Al – 35 wt.% Cu) thin films is consistent with prior reports on the morphological zones developed during laser surface melting induced rapid solidification process in Al – 36 wt.% Cu and current SMSM for Al – Cu alloys [35], as shown in Figure 64, in which the yellow dashed line indicates the composition of the films used in current study. It can be seen that, as the solidification velocity increases, the microstructure development predicted for Al – 18.5Cu (Al – 35 wt.% Cu) alloy by the current SMSM starts with regular eutectic growth (stage i and ii, zone 2 in current study) and then transition into growth of supersaturated α-cells (stage iii and iv, zone 3 in current study). When solidification velocities exceed a critical velocity of ~ 0.5 ± 0.2 m/s, the α-cells are anticipated to exhibit banded morphology (later part of stage iv, zone 4 in current study as shown in Figure 62 c)).

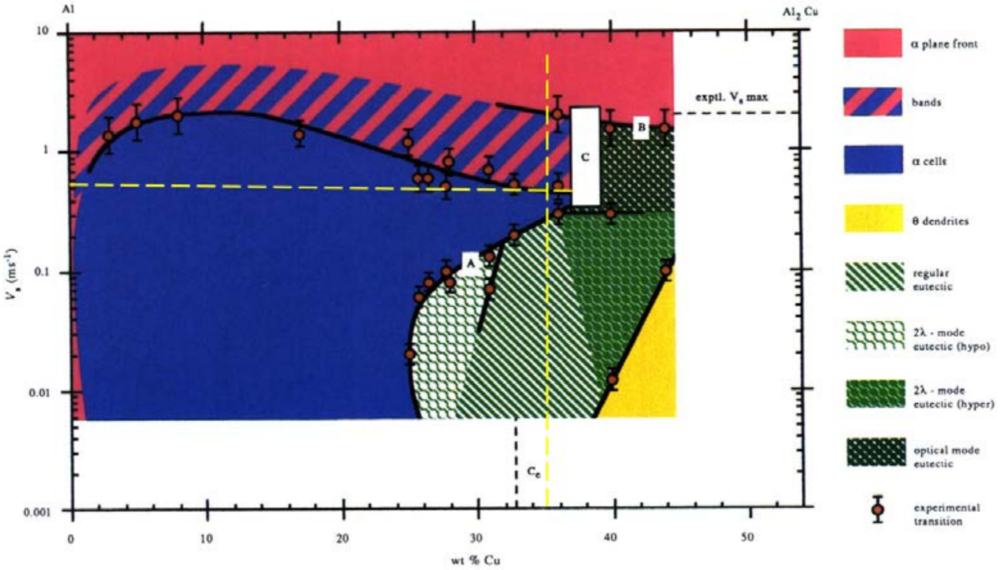

**Figure 64. Rapid solidification process of Al - 35 wt.% Cu predicted by current SMSM**

Although high-magnification DTEM experimentation is hindered by the beam effect, it is still possible to deduce the critical velocity for change of crystal growth mode from α-cells to banded morphology by combining post-mortem characterization results and low-magnification MM-DTEM observations. The distances between the ending location of the eutectic growth region and starting location of banded morphology have been measured in several montages of BF TEM images of the in situ melt pool. An average distance of ~ 18.7 um between the onset of columnar growth and commencement of the banded morphology has been determined. After scrutinizing the individual images in the low-magnification MM-DTEM sequences presented in Figure 58, it can be noticed that interface instability begins to appear at the start of the second last sequence between t = 100.05 μs and t = 105.15 μs. These three frames of low-magnification MM-DTEM sequence images are enlarged and shown in Figure 65.

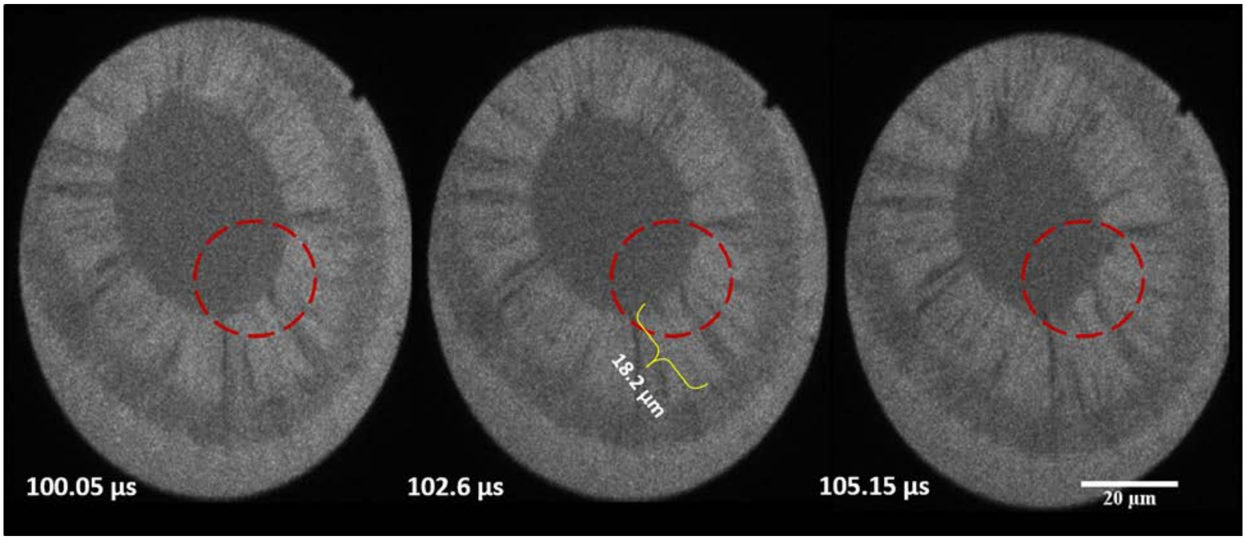

**Figure 65. Enlarged view of images extracted from low-magnification DTEM sequence at t = 100.05 μs, 102.6 μs and 105.15 μs, with red dashed circle highlighting the evolving interface stability**

As shown in Figure 65, the shape of the melt pool at t = 100.05 μs is still quite close to elliptical and the interface is mostly planar at this scale. However, at t = 102.6 μs, part of the interface, as illustrated by red dashed circle in Figure 65, is obviously protruding further out into the melt, disrupting the elliptical shape of the melt pool and the planar liquid-solid interface. This interface instability continues to develop and becomes distinct in the micrograph obtained at t = 105.15 μs, resulting in the shape of melt pool developing significant deviation from the symmetry of an ellipse. The distance between the origination of columnar grains and the location where the interface instability occurs is measured to be ~ 18.2 µm (shown in Figure 65). Combining these observations with the same type of distance of ~ 18.7 µm measured from post-mortem characterization results, it is reasonable to propose that the observed interface instability corresponds to the initiation of growth of banded morphology grains. Hence, the banded morphology crystal growth mode initiated between t = 100.5 µs and t = 102.6 µs. Since the evolution of converted radius shows a stable concave-shaped evolution trend from 72.8 µs to 125.15 µs, the interface was accelerating during this time frame. Assuming the interface was accelerating with a constant acceleration, a second-order polynomial can be fitted to the converted radius evolution and a linear expression of the velocity evolution from 72.8 µs to 125.15 µs can be obtained by differentiating the second-order polynomial with regard to time. The velocity evolution of the solidification interface of the in situ melt pool in hyper-eutectic Al – Cu thin films from 72.8 µs to 125.15 µs that was shown in Figure 60 is separately displayed here in Figure 66 for convenience. From the deduced velocity evolution, it can be determined that the solidification velocity was ~ 0.52 m/s at t = 100.5 µs, and ~ 0.54 m/s at t = 102.6 µs. Therefore, the critical velocity for change of crystal growth mode from α-cells to banded morphology can be estimated as 0.53 ± 0.01 m/s. This value is in good agreement with the average value of 0.5 m/s estimated in prior work [35]. But results from current work drastically reduced the uncertainty associated with previously estimated critical velocity of 0.5 ± 0.2 m/s by 95%, from 40% uncertainty to ~ 2% uncertainty.

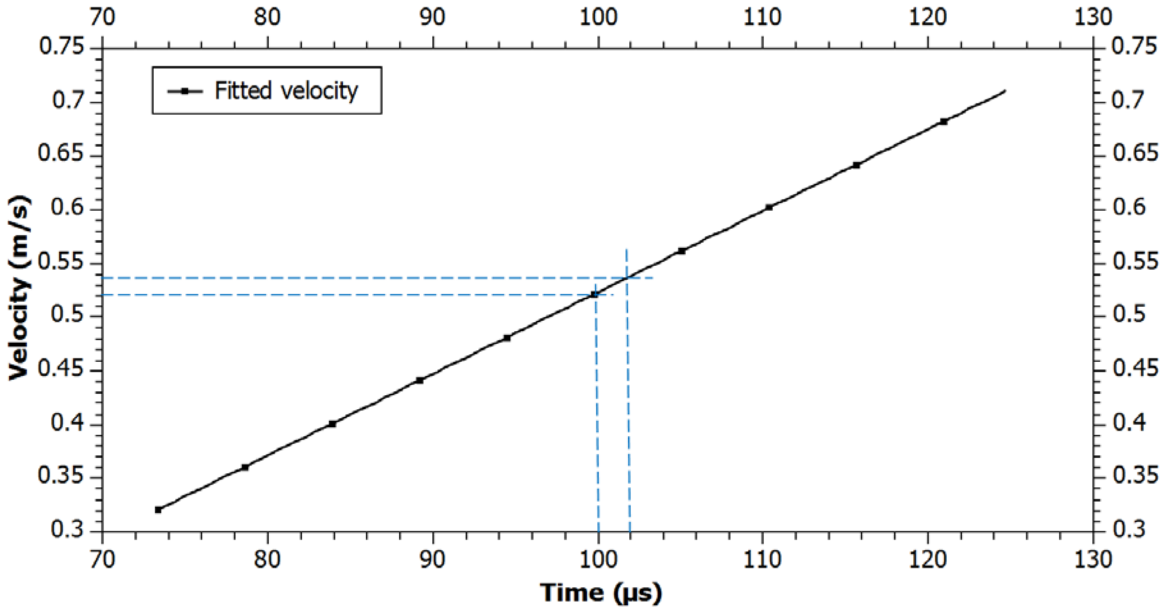

**Figure 66. Fitted velocity evolution from converted radius evolution between 72.9 µs to 125.15 µs. Blue dashed line represents the time frame (100 µs to 102 µs) determined for the initial growth of banded morphology and associated velocities**

Although the microstructure developed during the rapid solidification process in hyper-eutectic Al – Cu thin films is mostly consistent with past work [35], it is worth noting that a two-dimensional eutectic-type growth morphology was found in some regions at the edge of the in situ melt pool. In regular eutectic growth with single-wavelength periodicity and of lamellar morphology, the direction of the periodicity is perpendicular to the growth direction. On the other hand, the two-dimensional eutectic-type growth morphology exhibits periodicity not only perpendicular to the growth direction but also parallel to the growth direction. The appearance of the two-dimensional eutectic growth morphology is similar to a morphology observed in the rapidly solidified microstructure of Al – 44 wt.% Cu and termed as “optical eutectic” in past work and marked in the SMSM of Al – Cu alloys [35]. A comparison of the morphology of the two-dimensional eutectic found in present investigation and the morphology of “optical eutectic” reported previously is displayed in Figure 67, with arrows in the images representing the solidification direction.

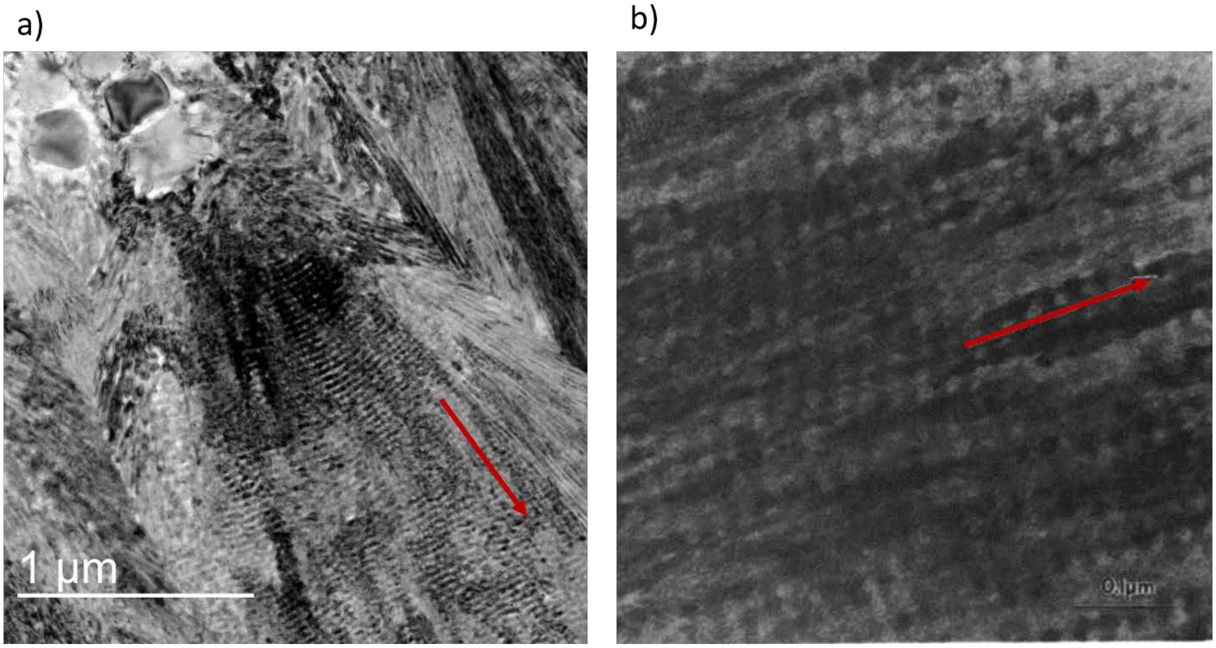

**Figure 67. a) BF TEM image of the two-dimensional eutectic-type growth observed at the edge of the melt pool in current study. b) Morphology of optical eutectic reported in reference** [35]

The morphologies of these two microstructures are at least very similar, if not exactly the same. However, currently the SMSM does not predict the appearance of optical eutectic for any solidification front velocity for the Al – 18.5Cu alloy used in the present study (see Figure 64). To the best of author’s knowledge, the origin of the formation and development of optical eutectic in Al – Cu alloys is still unclear [35,36]. However, it has been suggested that the growth of optical mode eutectic is associated with Al – Cu alloys with Cu concentration higher than 40 wt.% (22 at.% Cu) and high growth velocities, as reflected in the current SMSM. However, the current findings are partially in opposition to this assessment. TEM EDS measurements have been performed on the regular eutectic growth region and two-dimensional eutectic growth region and no noticeable difference in terms of average Cu concentration can be detected within the limits of TEM EDS measurements. Therefore, difference of Cu concentration cannot be taken as the reason to account for the different eutectic growth morphologies observed at the edge of the in situ melt pools. As mentioned before, the rapid acceleration of the solidification interface at the initial stage of rapid solidification was not captured by the low-magnification MM-DTEM sequence, while an initial velocity higher than 0.26 m/s is projected based on the converted radius evolution (Figure 59). Therefore, a rational hypothesis would be that the growth of two-dimensional eutectic morphology requires combination of high solidification velocity, hyper-eutectic Cu concentration and other factors such as crystallography, local perturbation or a certain thermal field distribution. Further investigation is needed to fully understand the origin of two-dimensional eutectic or optical eutectic growth.

STEM imaging and STEM-EDS based measurements and composition mapping have also been performed to examine the in situ melt pool in another set of in situ pulsed laser irradiated hyper-eutectic Al – Cu alloy thin film samples. Although this set of thin films were deposited using the same deposition parameters as the Al – 18.5Cu thin films, the average composition of the film is measured to be Al – 20 at.% Cu (as shown in Figure 57, section 7.1), slightly Cu-richer than the Al – 18.5Cu thin films due to inherent minor variations associated with the e-beam deposition processes. However, with a concentration difference of only 1.5 at% Cu, it is expected that the rapid solidification process in this set of sample should be very similar to the RS process in the Al – 18.5Cu samples. Therefore, when accompanied with data from Al – 18.5Cu samples, composition measurements from the Al – 20 at.% Cu (Al – 20Cu) samples should still be useful for demonstrating and analyzing in situ pulse laser irradiation induced rapid solidification proocess related microstructure evolution in hyper-eutectic Al – Cu alloys.

Example HAADF-STEM images of the edge of the in situ melt pool and the transition region from columnar grain into banded morphology, accompanied by corresponding compositional mapping are shown in Figure 68. Three grains at the melt pool edge, showing typical eutectic growth morphology as reflected by the contrast in the HAADF-STEM image in Figure 68 a), are labeled as i, ii and iii and are separated by red dashed lines for visualization purpose. Figure 68 a) and c) show the HAADF-STEM images of the examined areas and Figure 68 b) and d) present the corresponding color-coded Cu concentration level map. In Figure 68 b) and d) redder color represents higher concentration level of Cu. Quantitative STEM-EDS measurements of specific areas and also line scans for detecting compositional change along the scanned direction have been conducted for specific locations marked in Figure 68 a) using red circles (#1 - #3) for area measurements, red arrows (#4 and # 5) for line scans and red rectangle in Figure 68 c) for area measurements. The compositions from area measurements in terms of atomic percent of Cu are summarized in Table 12. Composition variations along the line scans are shown in Figure 68 e) and f).

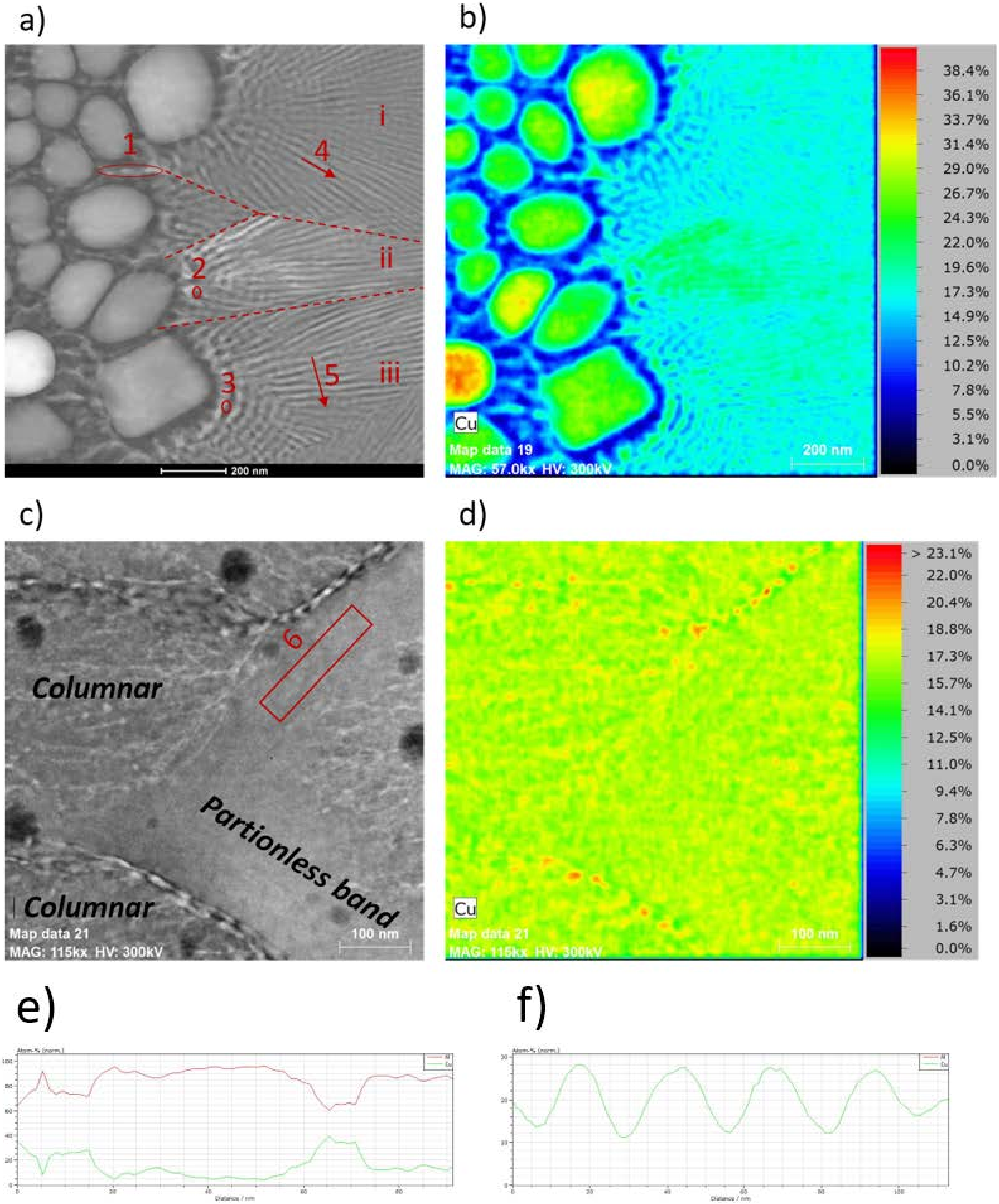

**Figure 68. a) HAADF STEM image of the edge of the in situ melt pool, b) Cu concentration heat map corresponds to STEM image in a), c) HAADF STEM image of the columnar to banded transition region, d) Cu concentration heat map corresponds to STEM image in c), e) Scanned profile of line scan #4 in a). f) Scanned profile of line scan #5 in a).**

**Table 12. EDS measurements results in Figure 68 in terms of atomic percent of Cu**

| Scan # | at.% Cu |
|---|---|
| **1** | 16.11 |
| **2** | 8.71 |
| **3** | 11.93 |
| **6** | 20.10 |

By correlating the oscillating contrast changes shown in HAADF STEM image of Figure 68 a) and the same behavior of Cu concentration changes reflected in the STEM-EDS Cu concentration mapping in Figure 68 b), the two-dimensional periodicity of the eutectic morphology is clear, and especially evident in areas that are close to the edge of the melt pool in grain i and grain iii. Results in Table 12 from area EDS measurements performed at locations 1, 2 and 3 demonstrate that the small regions with darker contrast (e.g. scan #2 and #3) are obviously more Cu-depleted than regions with brighter contrast (e.g. scan #1). Moreover, line scans #4 and #5 illustrates the presence of periodical variation of Cu concentration along not only directions perpendicular to the crystal growth direction (e.g. line scan #5 and Figure 68 f)), which is expected for regular eutectic growth morphology, but also along directions parallel to the crystal growth direction (e.g. line scan #5 and Figure 68 e)), which is not present in regular eutectic growth morphology. These observations collectively demonstrate the occurrence of a two-dimensional eutectic growth morphology in areas that are close to the in situ melt pool edge in hyper-eutectic Al-20Cu thin films. These microstructure characteristics are very similar to those observed in Al-18.5Cu thin films through conventional transmission electron microscopy. Notably, this two-dimensional eutectic growth morphology becomes less and less prominent as the eutectic growth further extends into the center of the melt pool, as shown in Figure 68 a). Recall that the tentative velocity evolution (shown in Figure 60) deduced from the converted radius evolution (displayed in Figure 59) during RS process of Al – 18.5Cu, the solidification interface migrated with an average solidification velocity of ~ 0.43 m/s initially and then decelerated to lower velocities during the initial stage (i.e. stage i as described previously in this section). Similar solidification velocity evolution is anticipated during the RS process of the Al – 20Cu thin films, despite the minor Cu concentration difference. Therefore, it is proposed here that the growth of the two-dimensional eutectics corresponds to relatively high solidification velocities and the crystal growth mode is gradually taken over by the regular eutectic growth as the solidification velocity gradually decreases during the initial stage, marked Stage i in Figure 59 and Figure 60. As a result, the two-dimensional eutectic growth morphology is most prominent in areas right next to the edge of the in situ melt pool (e.g. as shown in grain i and iii in Figure 68 a)) and progressively becomes less significant as eutectic growth continues with reducing solidification velocities.

Banded morphology has also been observed in the rapidly solidified microstructure in the in situ melt pool of Al – 20Cu thin films and an example of the transition from columnar grains into banded morphology is shown in Figure 68 c), with associated STEM EDS based Cu concentration level mapping displayed in Figure 68 d).

As expected, except along the grains boundaries that are decorated by θ-related Cu-rich phases between the columnar and banded grains, no significant Cu-enrichment can be observed in the matrix of the columnar grains and the composition measured from EDS measurements in the partionless band of the banded morphology is essentially the same as the film composition (e.g. Al – 20Cu as summarized in Table 12). Similar to what has been observed in Al – 18.5Cu, the two-dimensional eutectic growth morphology and the banded morphology are both present in the rapidly solidified microstructure in Al – 20Cu thin films, further proves the two-dimensional eutectic growth (or optical eutectic as termed in Ref. [35]) and banded morphology are not mutually exclusive in the hyper-eutectic Al – Cu alloys.

However, although the Al – 20Cu (Al – 37 wt.% Cu) correspond to the boundary of an undefined part of the current SMSM (previously shown in Figure 9, reinserted here as Figure 69 for convenience), previous assessments and proposed SMSM [35,36,113,115] do not indicate a microstructure development path for transition from to optical eutectic, or vice versa, or co-occurrence banded morphology and optical eutectic for hyper-eutectic Al – Cu alloys. This is in contrast to current findings in this study. Based on current results, the maximum velocity during the initial stage of RS process in Al-18.5Cu is ~ 0.43 m/s, while the transition of crystal growth mode from columnar growth into banded morphology occurs at a higher average solidification velocity of ~ 0.53 m/s. It is reasonable to expect similar behavior in other compositions of the hyper-eutectic Al – Cu alloys. Therefore, two-dimensional eutectic (optical eutectic) growth corresponds to intermediate to high average solidification velocity (e.g. ~ 0.4 m/s for Al –

18.5Cu) and banded morphology occurs when even higher average solidification velocity is reached (e.g. ~ 0.5 m/s for Al – 18.5Cu). However, for RS processes in a certain range of compositions on the hyper-eutectic Al – Cu alloy side (from composition just over the eutectic to ~ Al – 39 wt.% Cu based on the current SMSM), the first rapidly solidified microstructure is regular eutectic, which transitions into columnar growth of supersaturated α-cells at increased solidification interface velocity. The switch from growth of supersaturated α-cells to a regular eutectic-type growth morphology is too difficult, since it would require sufficient partition of the solute atoms (Cu in the case of Al – Cu alloys) in very short time frames and nucleation and growth of ordered phase in a periodic manner from the pre-existing supersaturated α-cells as well. On the other hand, for RS processes in a range of compositions above ~Al – 39 wt.% Cu based on the current SMSM, the first rapidly solidified microstructure is 2λ-eutectic. Instead of transitioning into columnar growth of α-cells, the eutectic growth morphology is maintained even at higher velocities, which provides "seeds" for an easier transition into optical eutectic (two-dimensional eutectic) to occur as re-nucleation of supersaturated α-cells and Cu-rich θ-related phase is no longer required. In the current study, the existing eutectic in between the θ-$Al_2Cu$ grains, which are formed during the partial melting along the grain boundaries and incubation stage, can also serve as "seeds" for eutectic growth and the high solidification velocity initially resulted in the formation of two-dimensional eutectic morphology. Considering the two-dimensional eutectic morphology is basically an inter-woven banded morphology, it is rational to speculate the growth of two-dimensional eutectic morphology is associated with the same type of interface instability [113,115] that leads to the growth of banded morphology.

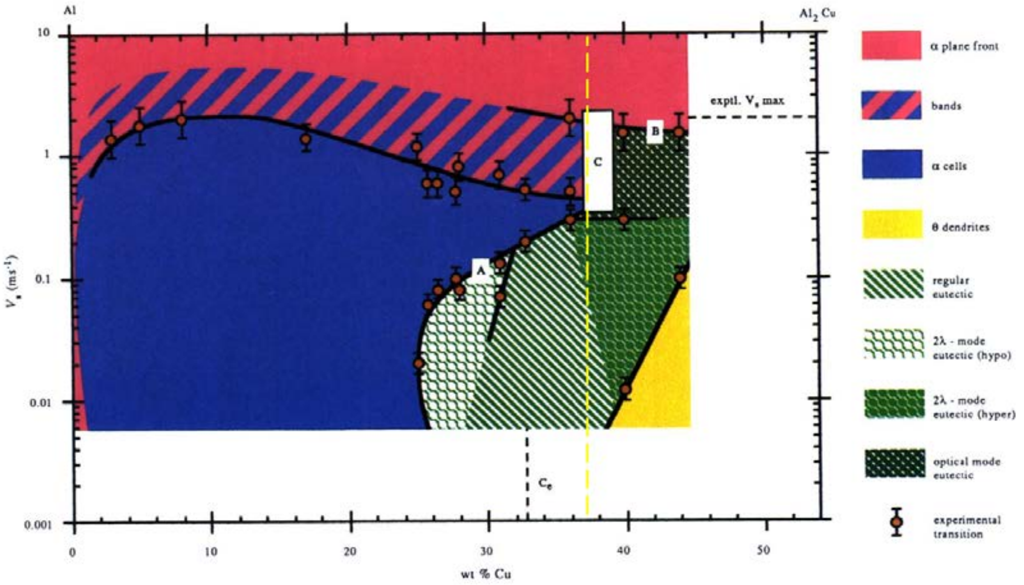

**Figure 69. Current SMSM proposed by Gill and Kurz** [35] **with yellow dashed line indicating corresponding composition of Al-20Cu (Al - 37 wt.% Cu) on the SMSM**

With data from current study, it is possible to construct a schematic SMSM in the hyper-eutectic Al – Cu alloy regime with some modifications. A tentative schematic of a SMSM for hyper-eutectic Al – Cu regime with linear velocity scale instead of log-scale is presented in Figure 70. The light blue data points with significant error bars on linear scale are data points extracted from existing Al – Cu SMSM while the yellow data points are from current study and the error bars are not noticeable on the scale used in Figure 70. Recall that the highest velocity estimated in the initial stage (stage i) is ~ 0.4 m/s and it is still lower than the critical velocity of ~ 0.5 m/s for crystal growth mode change to banded morphology, a small region of optical eutectic is set in between the α-cells and bands with white dashed line separating the aforementioned regions since more data points are needed to determine the exact shape of the transition boundaries in Figure 70. Although we have discovered morphologies including regular eutectic, α-cells, optical eutectic and banded morphology in Al – 20Cu, it is uncertain that if a sharp transition from regular eutectic to 2λ-eutectic or bands to optical eutectic would occur in hyper-eutectic Al – Cu alloys with Cu higher than 20 at.% Cu. Therefore, the transition boundary between these growth modes are depicted using white dashed line in Figure 70.

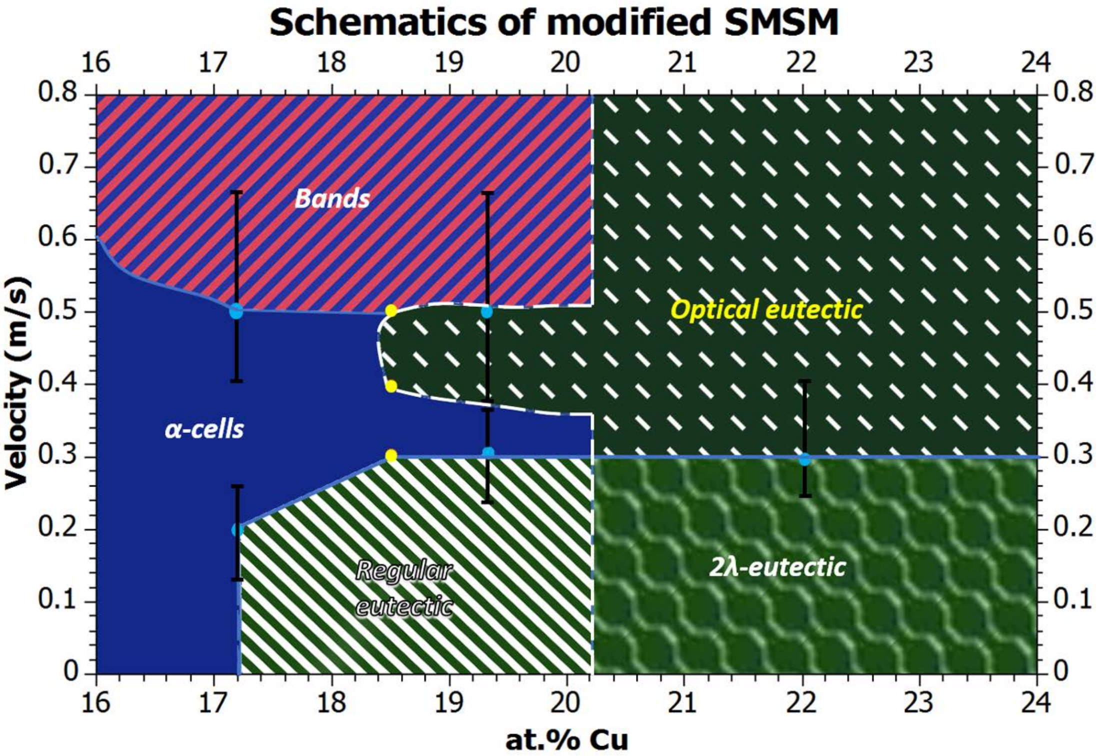

Figure 70. Modified SMSM in hyper-eutectic Al-Cu regime with linear velocity scale

## 7.3 SUMMARY

In situ pulsed laser irradiation induced rapid solidification in nanocrystalline hyper-eutectic Al – Cu alloy thin films have been investigated. Through a combination of in situ DTEM experimentation and post-mortem characterization, preliminary understanding of solidification behavior during rapid solidification process in hyper-eutectic Al – Cu alloy thin films have been achieved.

In situ low-magnification MM-DTEM observations showed that the incubation time for rapid solidification process in hyper-eutectic Al – 18.5Cu alloy thin films is ~ 22.6 µs. Unlike the cases of rapid solidification process in Al and hypo-eutectic Al – Cu thin film, it is more appropriate to use separate solidification stages instead of a continuous velocity evolution function to describe the rapid solidification process in hyper-eutectic Al – Cu thin films. However, beam effect induced artifacts hinder effective DTEM observation with high spatio-temporal resolution and great care has to be taken to consider the effects from electron beam heating for observations in MM-DTEM experiments performed at high imaging magnifications. This holds especially true for the study of dynamics of the rapid solidification processes under conditions involving a relatively flat thermal gradient in the liquid ahead of the transformation interface, e.g. towards the end of the solidification sequence and Al-Cu alloys close to the eutectic composition. Adjustment of the image formation laser will be necessary to perform meaningful high-magnification DTEM experimentation in hyper-eutectic Al – Cu alloys.

Post-mortem characterization of rapidly solidified microstructure in the in situ melt pool confirmed the correspondence between the morphological zones developed in hyper-eutectic Al – Cu alloys during surface laser melting induced rapid solidification and in situ laser irradiation induced rapid solidification. The solidified microstructure starts with regular eutectic growth, followed by directional growth of α-cells and then transition into banded morphology when the solidification velocity exceeds a critical velocity. By assuming a constant acceleration of the solidification interface during the rapid growth stage of the solidification process and combining the low-magnification DTEM observation with post-mortem characterization results, a critical velocity of 0.53 ± 0.01 m/s for transition of crystal growth mode from α-cells into banded morphology can be estimated, which is in good agreement with previously reported average value of ~ 0.5 ± 0.2 m/s, but drastically reduced the uncertainties by 95%.

Presence of a two-dimensional eutectic-type growth morphology is observed at some areas close to the edge of the in situ melt pools as the starting growth morphology, which is not predicted by the current SMSM and in contrast to prior assessment of rapid solidification behavior in hyper-eutectic Al – Cu alloys. A potential explanation accounting for the observed co-occurrence of two-dimensional eutectic-type growth morphology and banded morphology and the absence of such behavior in previous observation, based on the difficulties of transition from supersaturated α-cells to a regular eutectic-type growth morphology, is proposed in current study. Further investigation is needed to properly understand the formation and development of the two-dimensional eutectic-type growth morphology.

# 8.0 SUMMARY AND OUTLOOK

## 8.1 SUMMARY AND CONCLUSIONS

The Dynamic TEM and MM-DTEM experimentation enabled characterization of pulsed laser induced melting and rapid solidification processes in Al and Al – Cu alloys with unprecedented temporal-spatial resolution. For the first time, the rapid solidification processes in nanocrystalline Al, hypo-eutectic Al – 11Cu alloy and hyper-eutectic Al – 18.5Cu alloy thin films have been directly documented with nano-scale spatio-temporal resolution that is not attainable by conventional characterization techniques utilizing the DTEM by the current study and parallel study within the same research group [28]. Continuum modeling benchmarked by experimental metrics has been performed to determine the thermal evolution during the rapid solidification of pure Al thin film, demonstrating the unique capability of DTEM to provide direct observation with nano-scale spatio-temporal resolution and validation of computational modeling.

Accompanying the in stiu DTEM observations with post-mortem characterization techniques, the rapidly solidification processes and resultant microstructure have been characterized to determine the critical velocity for transition of crystal growth mode from columnar growth into banded morphology. A critical velocity of 0.8 ± 0.05 m/s and 0.53

± 0.01 m/s have been determined for Al – 11Cu alloy and Al – 18.5Cu alloy, respectively. Critical velocities determined by current study exhibit significantly improved uncertainties over previously reported data sets [35], facilitating quantitative understanding of the microstructural change resulted from rapid solidification processes with high accuracy and further development and validation of solidification models pertain to rapid solidification processes in metallic systems.

Effect of crystallography on the rapid solidification process in Al – 11Cu alloy thin films was evaluated by ex situ laser irradiation experimentation. At high crystal growth rate of ~ 0.5 to 0.8 m/s, combining observations obtained from in situ MM-DTEM experiments and post-mortem characterization of microstructure after ex situ laser irradiation allowed comparative study and understanding of crystallographic effects on the rapid solidification process in hypo-eutectic Al – Cu alloys, despite the RS process was not directly recorded during ex situ laser irradiation experimentation.

Although the overall microstructure development observed during rapid solidification process of hyper-eutectic Al – Cu alloys is consistent with prior reports [35,36], co-occurrence of a two-dimensional eutectic-type growth morphology and banded morphology that is contrary to previous assessments and speculations [35] has been observed in hyper-eutectic Al – Cu alloys for the first time to the best of author's knowledge. A potential explanation that can satisfactorily account for the seemingly contradicting behavior is postulated based on the experimental results from current investigation.

To conclude, the hypotheses proposed in Chapter 2.0 have been examined and evaluated through this study and the following conclusions can be drawn:

- In situ observations accompanied with continuum modeling results showed that the RS process in Al thin film is dominated by in-plane heat conduction through the metallic layer at locations that are > 100 μm away from the thick Si support frame in the TEM grids used
- Similar to Al – 4 Cu, four morphological zones formed in the in situ pulsed laser irradiated Al – 11Cu thin films. However, increased Cu content in Al – 11Cu thin films lead to longer incubation time, slower velocity evolution and change of microstructure characteristics, especially in the heat affected zone (zone 1) and the transition zone (zone 2)
- Preferred solidification directions of or close to <001> due to crystallographic effect have been identified during RS process with high crystal growth rate of ~ 0.5 to 0.7 m/s in hypo-eutectic Al-11Cu thin films
- Since the primary phase formed is faceted θ-$Al_2Cu$ phase upon solidification, fundamentally different stages of crystal growth modes and associated microstructure development and different characteristics in the crystal growth rate evolution have been observed during RS processes in hyper-eutectic Al-18.5Cu thin films
- Co-occurrence of banded morphology and two-dimensional eutectics have been discovered in Al – 18.5Cu and Al – 20Cu thin films, suggesting some modification to the hyper-eutectic part of existing Al – Cu SMSM

## 8.2 OUTLOOK

With experimental data available on the RS process of Al – 4Cu and Al – 11Cu, especially the critical velocities determined with high accuracy, collaboration with modeling experts to develop more sophisticated solidification models for properly describing rapid solidification process, including associated velocity evolution, development of morphological zones and transition between them, in hypo-eutectic Al – Cu alloy systems that can be validated by in situ MM-DTEM observations presented in current study will greatly advance current understanding of rapid solidification process and enables development of truly predictive computational models for rapid solidification process in the Al – Cu alloy systems.

Further improvements of the DTEM instruments such as a illumination source with higher brightness or higher accelerating voltage will allow more details of the evolving interface to be resolved during DTEM experimentation [117], especially at high-magnification mode. More advanced laser irradiation system that permits more arbitrary control of the laser pulse would allow quantification of the beam effect and examination of influence of laser profile on the rapid solidification process, such as extent of HAZ, curvature effect and crystallographic effect.

In opposition to previous propositions, current investigation implies the growth of optical eutectic morphology and banded morphology are not mutually exclusive in hyper-eutectic Al – Cu alloys. In order to gain better understanding of rapid solidification process in hyper-eutectic Al – Cu alloys, experimental effort using hyper-eutectic Cu compositions that range from Al – 20 at.% Cu to Al – 24 at.% Cu will allow more comprehensive evaluation of the different microstructure development path on the hyper-eutectic Cu part suggested by current SMSM as the initial rapidly solidified microstructure changes from regular eutectic to 2λ-eutectic.

# APPENDIX A

# FURTHER READINGS

Publications and conference proceedings directly resulted from the current study are listed below for potential readers to pursue interests regarding specific questions and aspects of this research:

**Publications:**

1. "Determination of Crystal Growth Rates during Rapid Solidification of Polycrystalline Aluminum by Nano-scale Spatio-temporal Resolution In Situ Transmission Electron Microscopy," *J. Appl. Phys., 120, 055106*
2. "Time-Resolved In Situ Measurements during Rapid Alloy Solidification: Experimental Insight for Additive Manufacturing," *JOM 68 (3), 985-999*
3. "In-situ Transmission Electron Microscopy of Crystal Growth-mode Transitions during Rapid Solidification of a Hypoeutectic Al-Cu alloy," *Acta Mater. 65, 56-68*

**Conferences:**

1. "Nano-Scale Spatio-Temporal Resolution in situ TEM and Numerical Modeling of Rapid Solidification Microstructure Evolution in Al Alloys After Laser Melting", *Microsc. Microanal 22 (S3), 1754-1755*

2. “Quantitative Phase Analysis of Rapid Solidification Products in Al-Cu Alloys by Automated Crystal Orientation Mapping in the TEM”, *Microsc. Microanal 21 (S3), 1465-1466*
3. “Quantitative Determination of Thermal Fields and Transformation Rates in Rapidly Solidifying Aluminum by Numerical Modeling and In-situ TEM,” *Microsc. Microanal 21 (S3), 811-812*
4. “Capturing dynamics of pulsed laser induced melting and rapid solidification in aluminum polycrystals with nanoscale temporal resolution in-situ TEM”, *Microsc. Microanal 20 (S3), 1582-1583*
5. “Rapid Solidification in Thin-Film Al-Cu Alloys: Capturing the Dynamics with Time-Resolved In Situ TEM”, *Microsc. Microanal 20 (S3), 1580-1581*
6. “Crystal Growth Mode Changes during Pulsed Laser Induced Rapid Solidification in Nanoscale Thin Films of Al-Cu Eutectic,” *Microsc. Microanal 20 (S3), 1662-1663*

# BIBLIOGRAPHY

[1] Kurz W, Fisher DJ. Fundamentals of Solidification, 4th revise. Trans Tech Publications; 1998.

[2] Lavernia EJ, Srivatsan TS. J Mater Sci 2010;45:287.

[3] Jacobson LA, McKittrick J. Mater Sci Eng R Reports 1994;11:355.

[4] Kurz W, Trivedi R. Mater Sci Eng A 1994;179–180:46.

[5] Boettinger WJ, Coriell SR, Greer a L, Karma A, Kurz W, Rappaz M, Trivedi R. Acta Mater 2000;48:43.

[6] Asta M, Beckermann C, Karma A, Kurz W, Napolitano R, Plapp M, Purdy G, Rappaz M, Trivedi R. Acta Mater 2009;57:941.

[7] McKeown JT, Kulovits AK, Liu C, Zweiacker K, Reed BW, Lagrange T, Wiezorek JMK, Campbell GH. Acta Mater 2014;65:56.

[8] Chichkov BN, Momma C, Nolte S, Alvensleben F, Tünnermann A. Appl Phys A Mater Sci Process 1996;63:109.

[9] Boneberg J, Bischof J, Leiderer P. Opt Commun 2000;174:145.

[10] Favazza C, Kalyanaraman R, Sureshkumar R. J Appl Phys 2007;102:104308.

[11] Frewin MR, Scott DA. Weld J 1999;78:15.s.

[12] Gan Y, Chen JK. Appl Phys Lett 2009;94:201116.

[13] Ivanov DS, Rethfeld B, O’Connor GM, Glynn TJ, Volkov AN, Zhigilei L V. Appl Phys A 2008;92:791.

[14] Ivanov D, Zhigilei L. Phys Rev B 2003;68:641141.

[15] Jiang L, Tsai H-L. J Heat Transfer 2005;127:1167.

[16] Jiang L, Tsai H-L. Int J Heat Mass Transf 2007;50:3461.

[17] Koch J, Korte F, Bauer T, Fallnich C, Ostendorf A, Chichkov BN. Appl Phys A 2005;81:325.

[18] Kulovits A, Zhong R, Wiezorek JMK, Leonard JP. Thin Solid Films 2009;517:3629.

[19] Lasagni A, Mücklich F. J Mater Process Technol 2009;209:202.

[20] MacDonald C a., Malvezzi a. M, Spaepen F. J Appl Phys 1989;65:129.

[21] Pronko PP, Dutta SK, Du D, Singh RK. J Appl Phys 1995;78:6233.

[22] Rethfeld B, Kaiser A, Vicanek M, Simon G. Phys Rev B 2002;65:1.

[23] Trice J, Thomas D, Favazza C, Sureshkumar R, Kalyanaraman R. Phys Rev B 2007;75:1.

[24] Zhong R, Kulovits A, Wiezorek JMK, Leonard JP. Appl Surf Sci 2009;256:105.

[25] Galenko PK, Reutzel S, Herlach DM, Fries SG, Steinbach I, Apel M. Acta Mater 2009;57:6166.

[26] Jian Z, Nagashio K, Kuribayashi K. Metall Mater Trans A 2002;33:2947.

[27] Yokota T, Murayama M, Howe J. Phys Rev Lett 2003;91:265504.

[28] Zweiacker K. In Situ TEM Investigation of Rapid Solidification of Aluminum and Aluminum Copper Alloys. University of Pittsburgh, 2015.

[29] King WE, Campbell GH, Frank A, Reed B, Schmerge JF, Siwick BJ, Stuart BC, Weber PM. J Appl Phys 2005;97:111101.

[30] Armstrong MR, Boyden K, Browning ND, Campbell GH, Colvin JD, DeHope WJ, Frank AM, Gibson DJ, Hartemann F, Kim JS, King WE, LaGrange TB, Pyke BJ, Reed BW, Shuttlesworth RM, Stuart BC, Torralva BR. Ultramicroscopy 2006;107:356.

[31] LaGrange T, Armstrong MR, Boyden K, Brown CG, Campbell GH, Colvin JD, DeHope WJ, Frank AM, Gibson DJ, Hartemann F V, Kim JS, King WE, Pyke BJ, Reed BW, Shirk MD, Shuttlesworth RM, Stuart BC, Torralva BR, Browning ND. Appl Phys Lett 2006;89:44105.

[32] LaGrange T, Campbell GH, Reed BW, Taheri M, Pesavento JB, Kim JS, Browning ND. Ultramicroscopy 2008;108:1441.

[33] Reed BW, Armstrong MR, Browning ND, Campbell GH, Evans JE, LaGrange T, Masiel DJ. Microsc Microanal 2009;15:272.

[34] Gill SC, Zimmermann M, Kurz W. Acta Metall Mater 1992;40:2895.

[35] Gill SC, Kurz W. Acta Metall Mater 1993;41:3563.

[36] Gill SC, Kurz W. Acta Metall Mater 1995;43:139.

[37] Zimmermann M, Carrard M, Kurz W. Acta Metall 1989;37:3305.

[38] Campbell J. Castings, 2nd ed. Butterworth-Heinemann; 2003.

[39] Committee ASMIH. ASM Handbook, Vol 15 - Cast n.d.

[40] Aziz MJ, T Kaplan. Acta Metall Mater 1988;36:2335.

[41] Aziz MJ. J Appl Phys 1982;53:1158.

[42] Aziz MJ, White CW. Phys Rev Lett 1986;57:2675.

[43] Kittl J a., Sanders PG, Aziz MJ, Brunco DP, Thompson MO. Acta Mater 2000;48:4797.

[44] Willnecker R, Herlach DM, Feuerbacher B. Appl Phys Lett 1990;56.

[45] Kittl J a., Reitano R, Aziz MJ, Brunco DP, Thompson MO. J Appl Phys 1993;73:3725.

[46] Aziz MJ. Metall Mater Trans A 1996;27:671.

[47] Colligan GA, Bayles BJ. Acta Metall 1962;10:895.

[48] Lum JW, Matson DM, Flemings MC. Metall Mater Trans B 1996;27:865.

[49] Wu Y, Piccone TJ, Shiohara Y, Flemings MC. Metall Trans A 1987;18:915.

[50] Willnecker R, Herlach DM, Feuerbacher B. Appl Phys Lett 1986;49.

[51] Willnecker R, Herlach D, Feuerbacher B. Phys Rev Lett 1989;62:2707.

[52] Herlach DM. Mater Sci Eng R Reports 1994;12:177.

[53] Herlach DM, Galenko PK. Mater Sci Eng A 2007;448–451:34.

[54] Lipton J, Kurz W, Trivedi R. Acta Metall 1987;35:957.

[55] Buchmann M, Rettenmayr M. Scr Mater 2007;57:169.

[56] Galvin GJ, Thompson MO, Mayer JW, Hammond RB, Paulter N, Peercy PS. Phys Rev Lett 1982;48:33.

[57] Thompson MO. Appl Phys Lett 1983;42:445.

[58] Tsao JY, Picraux ST, Peercy PS, Thompson MO. Appl Phys Lett 1986;48:278.

[59] Aziz MJ. Mater Sci Eng A 1997;226–228:255.

[60] Gilgien P, Zryd A, Kurz W. Acta Metall Mater 1995;43:3477.

[61] Kerr HW, Kurz W. Int Mater Rev 1996;41:129.

[62] Kurz W, Trivedi R. Metall Mater Trans A 1996;27:625.

[63] Kurz W. Adv Eng Mater 2001;3:443.

[64] Trivedi R, Magnin P, Kurz W. Acta Metall 1987;35:971.

[65] Ludwig A, Kurz W. Scr Mater 1996;35:1217.

[66] Kline JE, Leonard JP. Appl Phys Lett 2005;86:201902.

[67] Kulovits A, Wiezorek J, LaGrange T, Reed B, Campbell G. Microsc Microanal 2010;16:490.

[68] Kulovits A, Wiezorek JMK, LaGrange T, Reed BW, Campbell GH. Philos Mag Lett 2011;91:287.

[69] Zhong R. Microstructural Study of Laser-Induced Rapid Lateral Solidification of Metal Thin Films. University of Pittsburgh, 2010.

[70] Zhong R, Kulovits A, Wiezorek JMK, Leonard JP. Appl Surf Sci 2009;256:105.

[71] Kulovits A, Zhong R, Wiezorek JMK, Leonard JP. Thin Solid Films 2009;517:3629.

[72] LaGrange T, Campbell GH, Turchi PEA, King WE. Acta Mater 2007;55:5211.

[73] Taheri ML, McGowan S, Nikolova L, Evans JE, Teslich N, Lu JP, LaGrange T, Rosei F, Siwick BJ, Browning ND. Appl Phys Lett 2010;97:32102.

[74] LaGrange T, Campbell GH, Reed BW, Taheri M, Pesavento JB, Kim JS, Browning ND. Ultramicroscopy 2008;108:1441.

[75] Bostanjoglo O, Rosin T. Opt Acta Int J Opt 1977;24:657.

[76] King WE, Armstrong MR, Bostanjoglo O, Reed BW. High-Speed Electron Microscopy, in:. Hawkes PW, Spence JCH (Eds.). Sci. Microsc. Springer New York; 2007.

[77] LaGrange T, Reed BW, Santala MK, McKeown JT, Kulovits A, Wiezorek JMK, Nikolova L, Rosei F, Siwick BJ, Campbell GH. Micron 2012;43:1108.

[78] Liu B, Xu Q, Jing T, Shen H, Han Z. n.d.:19.

[79] Wolff F, Viskanta R. 1988;31.

[80] Rady MA, Satyamurty V V, Mohanty LAK. 1997;32.

[81] Hsu SC, Kou S, Mehrabian R, Introduction I, Hsu SC. 1980;11.

[82] Sekhar JA, Kou S, Mehrabian R. 1983;14:1169.

[83] Sowdari D, Majumdar P. Opt Laser Technol 2010;42:855.

[84] Boettinger WJ, Warren JA, Beckermann C, Karma A. Annu Rev Mater Res 2002;32:163.

[85] Wang S-L, Sekerka RF, Wheeler a. a., Murray BT, Coriell SR, Braun RJ, McFadden GB. Phys D Nonlinear Phenom 1993;69:189.

[86] Karma A, Rappel W-J. Phys Rev E 1998;57:4323.

[87] Hu H, Argyropoulos SA. 1996;4:371.

[88] Hills AWD, Malhotra SL, Moore MR. 1975;6.

[89] Shamsundar N, Sparrow EM. J Heat Transfer 1975;97:333.

[90] Peyre P, Aubry P, Fabbro R, Neveu R, Longuet a. J Phys D Appl Phys 2008;41:25403.

[91] Huang Z, Conway PP, Thomson RC, Dinsdale AT, Robinson JAJ. 2008;32:129.

[92] Levitas V, Samani K. Phys Rev B 2011;84:3.

[93] Zhang X, Grigoropoulos CP. Rev Sci Instrum 1995;66:1115.

[94] Glassbrenner CJ, Slack GA. Phys Rev 1964;134:A1058.

[95] Shanks HR, Maycock PD, Sidles PH, Danielson GC. Phys Rev 1963;130:1743.

[96] Thompson C V. Annu Rev Mater Sci 1990;20:245.

[97] Zweiacker K, McKeown JT, Liu C, LaGrange T, Reed BW, Campbell GH, Wiezorek JMK. J Appl Phys 2016;120:55106.

[98] Steen WM, Mazumder J. 2010.

[99] Bass M, Koechner W. Solid-State Lasers. New York: Springer-Verlag; 2003.

[100] AboelFotoh MO. J Appl Phys 1972;43:3789.

[101] Powell RW, Ho CY, Liley PE. Thermal Conductivity of Selected Materials-NSRDS-NBS-8. 1966.

[102] Rasband WS. 1997.

[103] Liu JM. Opt Lett 1982;7:196.

[104] Porter DA, Easterling KE, Sherif M. Phase Transformations in Metals and Alloys, (Revised Reprint). CRC Press; 2009.

[105] Steinbach I, Pezzolla F. Phys D Nonlinear Phenom 1999;134:385.

[106] Steinbach I. Model Simul Mater Sci Eng 2009;17:73001.

[107] Bhogireddy VSPK, Hüter C, Neugebauer J, Steinbach I, Karma A, Spatschek R. Phys Rev E - Stat Nonlinear, Soft Matter Phys 2014;90:1.

[108] Wang SC, Starink MJ. Int Mater Rev 2005;50:193.

[109] Williams DB, Carter CB. The Transmission Electron Microscope, in:. Transm. Electron Microsc. Springer; 1996.

[110] Liu C, Zweiacker K, McKeown JT, LaGrange T, Reed BW, Campbell GH, Wiezorek JMK. Microsc Microanal 2015;21:811.

[111] Gilgien P, Zryd A, Kurz W. ISIJ Int 1995;35:566.

[112] Trivedi R, Kurz W. Acta Metall 1986;34:1663.

[113] Carrard M, Gremaud M, Zimmermann M, Kurz W. Acta Metall Mater 1992;40:983.

[114] McKeown JT, Zweiacker K, Liu C, Coughlin DR, Clarke AJ, Baldwin JK, Gibbs JW, Roehling JD, Imhoff SD, Gibbs PJ, Tourret D, Wiezorek JMK, Campbell GH. JOM 2016;68:985.

[115] Zimmermann M, Carrard M, Gremaud M, Kurz W. Mater Sci Eng A 1991;134:1278.

[116] Zhong R, Kulovits a., Wiezorek JMK, Leonard JP. Appl Surf Sci 2009;256:105.

[117] LaGrange T, Reed BW, Masiel DJ. MRS Bull 2015;40:22.